MINORITY CARRIER TRANSPORT PARAMETERS IN HEAVILY DOPED SEMICONDUCTORS

BY

CHIH HSIN WANG

A DISSERTATION PRESENTED TO THE GRADUATE SCHOOL
OF THE UNIVERSITY OF FLORIDA IN PARTIAL FULFILLMENT
OF THE REQUIREMENTS FOR THE DEGREE OF DOCTOR OF PHILOSOPHY

UNIVERSITY OF FLORIDA

1991

TO MY PARENTS

ACKNOWLEDGEMENTS

I take this opportunity to thank my advisor, Prof. Neugroschel, for his advice and encouragement during my work. I deeply appreciate the freedom and the support he gave me to pursue my research projects. The freedom allowed me to generate numerous ideas and create new contributions to the science and technology. I enjoyed the experience of setting up the photoluminescence experiment and making it work. I also thank my co-advisor Prof. Lindholm for introducing me into the device group. I thank him for his support; I have benefited from the discussion with him. I am also grateful for his interest in my progress and work. Without their support, this work would not have been possible.

I have enjoyed and benefited from the discussions with Prof. Sah. I am also grateful for the correction he pointed out. His interest in the progress of my work is gratefully appreciated. I must also thank Profs. Bosman, Li, and Kurzweg for being on my supervisory committee. I thank Prof. Bosman for his advice in the design of the microstrip circuit.

I thank my good friend Dr. Misiakos for his help in my earlier research, and my officemate Chetan Parikh for stimulating discussions.

I also thank Prof. Srivastava for his generosity in allowing me to complete all the measurements in his optical laboratory.

I would also like to thank Dr. P. Holloway, Dr. R. Park, Mr. Lin, and Miss Y. Wang for providing the passivated GaAs wafer used in this work. The financial support of DARPA is gratefully acknowledged.

TABLE OF CONTENTS

		Page
ACKNOWLEDGEMENTS		iii
TABLE OF CONTENTS.		v
ABSTRACT		vii
CHAPTERS		
1	INTRODUCTION	1
	1.1 Motivation.	1
	1.2 Scope	3
	1.3 Overview of the Present Thesis.	5
2	MINORITY CARRIER TRANSPORT PARAMETERS IN DEGENERATE N-TYPE SILICON	8
	2.1 Introduction	9
	2.2 Theoretical Background	11
	2.3 Experimental Setup and Measurement	14
	2.4 Discussion	23
3	TEMPERATURE DEPENDENCE OF MINORITY HOLE MOBILITY IN HEAVILY DOPED SILICON.	57
	3.1 Introduction	57
	3.2 Experimental and Results	58
	3.3 Discussion and Conclusions	63
4	MINORITY-CARRIER LIFETIME AND SURFACE RECOMBINATION VELOCITY MEASUREMENT BY FREQUENCY-DOMAIN PHOTOLUMINESCENCE.	70
	4.1 Introduction	70
	4.2 Frequency-Domain Photoluminescence Decay (FDPL) for Semi-Infinite Slab	75
	4.3 Photoluminescence Measurements of S and τ.	82
	4.4 Comparison Between Time-Domain and Frequency-Domain Analyses.	89
	4.5 Conclusions.	92

5 NONDESTRUCTIVE MEASUREMENT OF MINORITY-CARRIER LIFETIME AND SURFACE/INTERFACE RECOMBINATION VELOCITY IN COMPOUND SEMICONDUCTORS. 112

5.1 Introduction. 112
5.2 Theoretical Analysis. 114
5.3 Experimental Setup and Measurements 121
5.4 Conclusions 126

6 LIFETIME AND SURFACE/INTERFACE RECOMBINATION VELOCITY MEASUREMENT IN THIN SEMICONDUCTORS LAYERS 137

6.1 Introduction. 137
6.2 Frequency-Domain Photoluminescence Decay for a Thin Layer. 141
6.3 Photoluminescence Measurements of S and τ. . .148
6.4 Conclusions 155

7 CONCLUSIONS 166

7.1 Contributions 166
7.2 Suggestions for Future Work 168

APPENDIX DESIGN AND FABRICATION OF THE TRANSMISSION LINE . . 174

REFERENCES 177

BIOGRAPHICAL SKETCH 182

Abstract of Dissertation Presented to the Graduate School
of the University of Florida in Partial Fulfillment of the
Requirements for the Degree of Doctor of Philosophy

MINORITY CARRIER TRANSPORT PARAMETERS IN HEAVILY DOPED SEMICONDUCTORS

By

Chih Hsin Wang

May 1991

Chairman: Arnost Neugroschel
Cochairman: Fredrik A. Lindholm
Major Department: Electrical Engineering

This dissertation describes the extraction of the minority-carrier transport parameters from heavily doped semiconductors.

The minority hole diffusion length L, the mobility μ and the lifetime τ have been measured in heavily phosphorous doped n-type silicon with the donor density N_{DD} ranging from 10^{18} cm^{-3} to 10^{20} cm^{-3}. For the measurements of these parameters, photodiodes with different metal overlap widths have been fabricated as the test structures. The diffusion length is extracted from the lateral photocurrent measurements for devices under steady state excitation. The lifetime and the minority carrier mobility (diffusivity) are measured from the

transient photocurrent measurements for devices under high speed laser excitation. All the parameters are simultaneously measured from the same device for the above doping range. Using the relation $L = (D\tau)^{1/2}$, which links all the measured transport parameters together, we performed the self-checking of the accuracy for the measured results.

The lifetime τ and the surface recombination velocity S in GaAs have been measured in GaAs wafers with chemically passivated surface, and from GaAs layers grown by molecular-beam-epitaxial technique. Three novel techniques that allow the nondestructive extraction of these parameters have been developed. One of the techniques, named Frequency-Domain Photoluminescence (FDPL), allows an independent determination of the τ and S from the same measurement, and presents new improvements over the conventional techniques. Due to the high tolerance for various kinds of noise, the techniques are especially useful for the sub-nanosecond lifetime measurement, which is a difficult task for the conventional techniques. Therefore, the techniques are important for the characterization of lifetime in III-V compound semiconductors, in which the lifetime can be as short as nanosecond for the doping density greater than 10^{19} cm^{-3}. Although the techniques are demonstrated on III-V materials, the methodology can be extended to other materials (e.g. Si, InP) for characterization of the surface and the bulk properties.

CHAPTER 1
INTRODUCTION

1.1 Motivation

In advanced silicon bipolar transistors, the shrinkage of the lateral dimensions is accompanied by a comparable reduction in the vertical dimensions, because of the scaling requirements. In order to avoid base punchthrough and to maintain low base resistance, the base doping density has to be increased to about 10^{18} cm^{-3} or higher for a thin-base transistor with a typical base width of less than about 1000 Å. To maintain a high common-emitter current gain for such a transistor, the emitter doping concentration is usually about 10^{20} cm^{-3}. Heavy doping effects are, therefore, significant in scaled bipolar devices. Device simulators for bipolar and field effect transistors require physical models and associated input parameters that describe how carrier transport varies with carrier concentrations, dopant densities, and temperature. To simulate the device performance, the direct measurements of the device parameters are essential. Since the confidence in using the predictions from the device simulator is achieved by comparing the predictions with the actual working device, a reliable data base for the simulator is, thus, of primary importance in order to provide the optimum information for device design. Accurate measurements of transport parameters are not only important for device

simulator, but also helpful for the understanding of the transport physics. They can provide clues to the device physicists for finding physical insights about the many scattering mechanisms existing in the carrier transport. Among these parameters, the minority carrier transport parameters are especially difficult to be accurately extracted from the measurements. Numerous measurement techniques have been developed for transport parameters extraction. Using these techniques, valuable measurement results have been reported. However, differences still existed among the data in the literature. In addition, none of the published data or techniques contain self-consistency checks that can verify their accuracy.

Recently, low temperature operation of high performance bipolar junction transistors has attracted a lot of interest in developing the next generation transistors. A great deal of effort has been devoted to integrating CMOS technologies with bipolar technologies (BiCMOS) for the low temperature operation of BiCMOS circuits. However, due to the lack of a reliable data base for the low-temperature minority carriers transport, the device simulators using the present data base may not be predictable and accurate enough to optimize the device performance. This lack of reliable data motivated the first part of this thesis.

The second part of the thesis concentrates primarily on the development of the methodology for the new techniques for characterization of the semiconductor bulk and surface/interface properties. Its motivation arises from the lack of the nondestructive measurement techniques that allow the separate determination of the surface recombination velocity and the carrier lifetime from the same measurement. In addition, for other nondestructive measurement

techniques that have been developed previously, the high frequency noise always prevents a more accurate determination of the parameters from the measured signals. This is specifically true for measuring lifetime in the range of sub-nanoseconds or a few nanoseconds. For studying the recombination mechanisms (such as Auger recombination) we need a highly accurate data to do the analysis. Without a good and accurate technique this purpose cannot be achieved. Therefore, the second part of the thesis is devoted to the development of measurement techniques with the application emphasis on the heavily doped semiconductors. Although, the measurement techniques developed here are useful in extracting parameters from heavily doped semiconductors, they are also applicable for practical purposes, such as the characterization of the surface passivations and the monitoring of the wafer processing for the process development. Due to its nondestructive properties, the techniques developed are also applicable to *in situ* monitoring of the wafer properties that correlate directly with the device performance. The *in situ* monitoring has become increasingly important as device processing evolves from the clean room to integrated *in situ* fabrication in multistage chambers. Thus, the techniques developed here are believed to be important for the future.

1.2 Scope

The work presented in this thesis is primarily concentrated on the minority carrier transport properties in heavily doped semiconductors. The parameters measured are the minority carrier lifetime τ, the

surface recombination velocity S, the carrier diffusion length L, the carrier diffusivity D, and the mobility μ. All the parameters are for minority carriers. No work is devoted to the study of the majority carrier transport. Only crystalline semiconductors are considered in this work.

All the parameters measured are obtained in low injection condition, which assures the transport parameters to be independent of the injection level and, hence, preserves a linear system in the measurements. Low injection condition, which states that the excess carrier density is much less than the background doping density, also avoids the issue of the validity of the quasi-neutrality and the effects due to the built-in field.

Both the electrical and optical techniques are used in this work. For the electrical techniques, parameters are directly extracted from the actual devices. For the optical techniques, parameters are extracted from both nonprocessed and processed wafers using different structures. All measurements used uniformly doped samples to avoid the effects due to the built-in field resulted from the gradient of doping density. The uniformly doped samples further assure the parameters be extracted from a field-free region.

Both the steady state and transient measurements were used in this work. The time scale of the transient measurements is much larger than the collision time of the carriers during transport. This validates the condition used in obtaining the Shockley current equation from the Boltzmann transport equation.

Finally, all measurements were done with the absence of hot carriers and ballistic transport. No high electric field was applied

in the measurements. The disturbed carrier-distribution is driven toward the local thermal equilibrium solely through scattering. The quasi-elastic condition is satisfied in the scattering process.

1.3 Overview of the Present Thesis

This thesis consists of two parts. The first part discusses the extraction of the transport parameters for the understanding of the minority carrier transport behavior and for generating the data base for the device simulation software. We employed a newly developed technique for this purpose. This technique allows simultaneous measurement of the minority carrier diffusion length L, lifetime τ, and diffusivity D from the same device, and provides a self-consistency check through the standard relation $L^2 = D\tau$ linking these three variables. The experimental results and the checking errors are presented. The comparison with some recent works are also discussed. There are two chapters, 2 and 3, in the first part. Chapter 2 describes the direct measurements of the minority hole transport parameters in degenerate n-type silicon by analyzing transient photocurrent response in the frequency domain. We model the minority carrier transient behavior by solving the continuity equation for a two-dimensional geometry device. Based on the results suggested by analyzing the analytical solution, a methodology to accurately extract the parameters is devised. The technique was employed to extract transport parameters for n-type silicon in the doping range of 10^{19} to 10^{20} cm^{-3}. Some interesting features of the minority hole mobility within this doping range are found for the first time. A possible

mechanism to explain the new behavior is discussed. Finally, the self-consistent checking is used to validate the accuracy of the measured results.

In Chapter 3, temperature dependence of the minority hole mobility $\mu_p(N_D,T)$ in heavily doped n^+ silicon in the doping range from 10^{18} to 2.4×10^{19} cm^{-3} was investigated. The preliminary measurements show that the mobility is strongly temperature dependent and is distinctly different from the majority hole mobility in p^+ silicon. Analytical fits to the measured data useful for low temperature simulation for bipolar devices are given.

Chapters 4, 5, and 6 compose the second part of this dissertation. The subject of this part of the thesis is the extraction of parameters governing the surface and bulk properties in semiconductors. To enable this extraction, new nondestructive measurement techniques are developed and demonstrated that extract parameters from semiconductor wafers and thin layers by measuring the photoluminescence decay. The noninvasive and high accuracy features of these techniques are addressed, and their advantages compared with other relevant techniques are discussed. Experimental results are obtained to illustrate the unique features of the new techniques.

In Chapter 4, the continuity equation for the minority carriers in an infinitely thick wafer is solved in the frequency domain. Based on the analytical solution, the expression for transient photoluminescence decay is derived. To reveal the advantages of the theory at different perspectives, the analysis is made for uniformly absorbed and strongly absorbed excitation conditions. A measurement method, based on this analysis, is developed for the extraction of transport parameters from heavily doped silicon, GaAs, and InP samples.

Chapter 5 describes a newly developed measurement technique for extracting parameters from semiconductor samples through time domain analysis of the photoluminescence signal. The continuity equation is solved by using Laplace transformation. A generalized expression that includes the self-absorption effect and is good for arbitrary surface conditions for photoluminescence decay is derived. Based on this analytical expression, we derive and analyze the expression for the effective lifetime, a physical quantity obtainable from the experiment. Finally, a methodology to nondestructively extract parameters from semiconductor wafers is presented and demonstrated on a chemically passivated GaAs wafer.

In Chapter 6, a novel technique to determine the minority carrier lifetime and the surface/interface recombination velocity from a thin hetero-structure layer is presented. The theoretical part of this technique is obtained by solving the continuity equation in the frequency domain for a thin layer. Based on the analysis of the analytical expression, new methodology is presented to extract the parameters from MBE-grown layers. The technique is demonstrated on both n- and p-type GaAs hetero-structure layers, and is believed to be important for the process developement of modern III-V devices.

Chapter 7 concludes and summarizes the main achievements of this work. The recommendations for future work for further investigations into the related areas are presented.

CHAPTER 2
MINORITY CARRIER TRANSPORT PARAMETERS IN DEGENERATE N-TYPE SILICON

This chapter describes the direct measurements of the minority hole transport parameters in degenerate n-type silicon by analyzing transient photocurrent in the frequency domain. Section 2.1 briefly reviews the relevant work done by other workers. The advantages and the limitations of these techniques are discussed. In section 2.2, the theoretical background of the measurement technique employed in this work is reviewed. Section 2.3 describes the device structure, the experimental setup, the measurement, and the results. Section 2.4 describes the main achievements obtained in this work. The comparison of the present results with that from literature is given, and the possible mechanism explaining the minority carrier transport is discussed.

In summary, the important achievements in this chapter are (1) minority hole mobility is found to increase with doping for doping larger than 4×10^{19} cm^{-3}; (2) the minority hole to majority hole mobility ratio is found to be about 2.8 at $N_{DD} = 7.2 \times 10^{19}$ cm^{-3}; (3) the measured lifetime shows a strongly Auger-dependent mechanism; (4) the extracted Auger coefficient at T = 296 K is $r_N^R = 2.22 \times 10^{-31}$ cm^6 s^{-1} and is in agreement with that reported by other workers. Finally,

self-consistent checking is used to validate the accuracy of the measured results.

2.1 Introduction

The minority carrier transport in heavily doped Si critically affects the performance of the advanced bipolar devices. To quantitatively model the static and dynamic properties of the high performance Si bipolar transistors, three doping-dependent parameters: the effective intrinsic carrier concentration n_{ie}, the minority carrier diffusivity D (or mobility μ_{min}), and the lifetime τ, are essential. Among those parameters, D and τ, which govern the minority carrier transport behavior, have to be extracted accurately in order to extract n_{ie}, which gives the information about energy gap narrowing ΔE_g, from the steady state device measurement [1,2]. The extraction of these parameters from device measurement is, however, not straightforward, especially in the degenerate doping range. Significant discrepancies exist between the values found in the literature [1]. Dziewior and Silber [3] measured D in the moderately doped p- and n-type Si (doping range 10^{17} - 10^{19} cm^{-3}) at 300 K by using chopped optical excitation. A device with bevelled geometry planar junction and a finely focused light beam were used in their technique, and valuable information about minority-carrier transport were generated. However, there are limitations to the applicability of their technique. Point generation sources in the micrometer scale are hard to realize, and besides, a

finely focused excitation source can cause locally high injection. With respect to a modulated source, a realistic modulation frequency is not high enough to determine nanosecond lifetime. Therefore, the highest doping they measured is ~ 10^{19} cm^{-3}. Swirhun et. al. [4] measured minority hole diffusion length L_p using lateral bipolar transistors of varied base widths, and lifetime on the same wafer by photoluminescence decay in the doping range of 10^{19} - 10^{20} cm^{-3}, and then calculated minority hole diffusivity using $D_p = L_p^2/\tau_p$. No direct measurements of D_p in the degenerate doping range has yet been reported. Both in Dziewior and Silber [3] and Swirhun et al. [4], a higher minority hole mobility μ_p(n-type) than that of majority hole μ_p(p-type) for the same doping was measured. The accuracy of these results is, however, difficult to establish.

Here, we report the values for D_p and τ_p obtained by direct measurement from the same device in the degenerate doping range of n-type Si (2.4×10^{19} cm^{-3} to 7.2×10^{19} cm^{-3}). The measurement technique is based on the lateral collection of a semi-infinite photodiode. Instead of a focused beam, it employs spatially uniform monochromatic light and creates a step generation profile by contact-shading the nonexcited areas. The device geometry is shown in Figure 2.1. The planar shallow junction is completely covered by its metal contact which extends laterally beyond the junction edge and overlaps with the passivating oxide. A spatially uniform laser light provides the excitation and generates carriers throughout the uncovered region. Shading the entire junction eliminates any emitter contributions to the

photocurrent so that the response is a function of the base transport parameters only. The photocurrent I_{ph} is a sensitive function of the oxide-contact overlap width W (Figure 2.1). Lifetime and mobility are extracted from fitting the frequency response of the measured diode photocurrent to the theoretical expressions for diodes with different shadowing overlap W [5,6]. The frequency dependence of the photocurrent was obtained by taking the Fourier transform of the time-domain response recorded on a fast transient digitizer. The response from devices with small overlap ($W << L$) yields directly τ independently of D, while the slope of the high-frequency response for the larger overlap device ($W >> L$) yields directly D independent of τ. This work extends the previous mobility data to higher dopings [6]. The accuracy of the results was self-consistently checked by comparing $(D_p\tau_p)^{1/2}$ with L_p obtained from a separate steady state measurement [7].

2.2 Theoretical Background

2.2.1 Transient Solution for Two-Dimensional Transport

Consider the semi-infinite geometry and mixed boundary conditions shown in Figure 2.2. The structure in the figure is converted from that in Figure 2.1 to make the two dimensional continuity equation solvable. For a well passivated silicon surface, the surface recombination velocity S is reasonably assumed to be zero. For the

analysis, we assume n-type material and let $p(x,y)$ be the excess minority-hole density in the base. The extension of the analysis to p-type material is straightforward. Because of the symmetry along the z axis and the absence of field, for the case of a line-focused monochromatic light that excites the surface at $x = x_0$, the continuity equation in the frequency domain is given as

$$\frac{\partial^2 p}{\partial x^2} + \frac{\partial^2 p}{\partial y^2} - \frac{p}{L'^2} + g(x,y) = 0. \tag{2.1}$$

where $L' = L/(1 + i\omega\tau)$ and denotes the complex diffusion length, and $g(x,y) = F\,\alpha\,(1 - R)\,\delta(x - x_0)\,\exp(\alpha y)$, of which F, R, and α are the flux density, the reflection coefficient, and the absorption coefficient, respectively.

The appropriate mixed boundary conditions are

$$p(x,0) = 0, \qquad x < 0, \tag{2.2a}$$

and

$$\frac{\partial p(x,y)}{\partial y} = 0, \qquad x > 0,\ y = 0, \tag{2.2b}$$

where (2.2a) is for the collection junction under reverse-bias and (2.2b) is for the well passivated surface with $S = 0$. Using reciprocity theorem [8] and Weiner-Hopf technique [9], (2.1) can be solved analytically together with the two boundary conditions (2.2a) and (2.2b). If $j(x_0)$ is the current collected by the semi-infinite junction per unit length, along the z axis, then we have [10]

$$j(x_0) = \frac{Q\alpha}{\alpha^2 - L^{-2}} \exp\left(\frac{-x_0}{L'}\right) \left[FX(x_0/L') - \frac{FX[x_0(-i\sigma + 1/L')}{2\sqrt{-i\sigma L' + 1}} - \frac{FX[x_0(i\sigma + 1/L')}{2\sqrt{i\sigma L' + 1}} \right], \tag{2.3}$$

where $Q = e\ F\ \alpha\ (1 - R)$, $FX(x) = \exp(x)\ \mathrm{erfc}(x^{1/2})$,
and $\sigma = (\alpha^2 - L'^{-2})^{1/2}$.

Expression (2.3) is for the finely focused line excitation; to obtain the photocurrent expression J(W,L') for the device with overlap W shown in Figure 2.1 under spatially uniform illumination, we have to integrate (2.3) from W to infinity. The integrated results are

$$I(W,L') = e\ F\ (1-R)\ \frac{\alpha^2\ L'}{\alpha^2 - L'^{-2}} \exp\left(\frac{-W}{L'}\right) \left[FX(W/L')\ (0.5 - W/L')\right.$$

$$\left. + (W/\pi L')^{1/2} + i\ \frac{FX[W(-i\sigma + 1/L')}{2\sigma L'\sqrt{-i\sigma L' + 1}} - i\ \frac{FX[W(i\sigma + 1/L')}{2\sigma L'\sqrt{i\sigma L' + 1}}\right]. \quad (2.4)$$

In both (2.3) and (2.4), when at static condition (i.e. $\omega = 0$), the two large fractions in the large square brackets are complex conjugate so that $j(x_0)$ and I(W,L') are both real [11]. Note that the expression of $e\ F\ (1-R)\ \exp(-W/L)\ L$ in (2.4) is identical to the one-dimensional photocurrent expression for a long base diode illuminated from W to infinity. Therefore, the rest of the expression can be viewed as a two-dimensional correction factor.

2.2.2 Analysis of The Solution

To make analyzing the frequency response easier, we consider the case for surface generation only (i.e. $\alpha L >> 1$). Therefore, (2.4) can be further simplified to

$$I(W,L') = e\ F\ (1 - R)\ \exp(-W/L')\ L'\ [FX(W/L')\ (0.5 - W/L') + (W/\pi L')^{1/2}], \text{ when } \alpha L >> 1. \quad (2.5)$$

The expression in (2.5) can be simplified to two special cases, namely, the small overlap case ($W \simeq 0$) and the large overlap case ($W >> L$). For the small overlap case, from (2.5), we have

$$I(0,L') = I(0,L)\ (1 + i\omega\tau)^{-1/2}, \tag{2.6a}$$

where $I(0,L)$ is the static photocurrent when $W = 0$. If we normalize $I(0,L')$ with respect to $I(0,L)$, the normalized result is

$$I_{nor}(0,L') = (1 + i\omega\tau)^{-1/2}, \tag{2.6b}$$

which shows that the frequency response is only a function of τ, independent of D. If the amplitude is plotted versus ω, the intercept is $1/\tau$ (this value is also defined as the corner frequency ω_c). Therefore, the small overlap frequency response can provide independently the information for the lifetime.

For the large overlap case, when $\omega\tau >> 1$ and $W >> L$, (2.5) can be simplified to

$$I(W,L') \simeq I(W,L)\ \exp(-W/L') \tag{2.7a}$$

$$= I(W,L)\ \exp[(-W/\sqrt{2D})\ (\sqrt{\omega} + i\sqrt{\omega}), \tag{2.7b}$$

where $I(W,L)$ is the static photocurrent for diode with overlap W. Thus, plotting the logarithm of the amplitude for sufficiently high frequency against $\sqrt{\omega}$ would result in a straight line having a slope of $-W/\sqrt{2D}$. Similar dependence of the slope in the phase plot can be also found; thus, the large overlap frequency responses provide a way of directly calculating D, independent of τ.

2.3 Experimental Setup and Measurement

2.3.1 Excitation and Optics

Figure 2.3 shows the experimental setup of the measurement. The second harmonic (wavelength λ = 0.532 μm) of the active/passive mode-locked Nd:YAG laser having a 30 ps pulse width, 30 Hz repetition rate, and about 0.3 GW peak power was employed as the optical excitation source. For a mode-locked laser, a train of pulses is produced by the oscillator. The time between the pulses is equal to the time it takes for light to make one round trip in the laser cavity. In a mode-locked laser, the cavity oscillator modes are "locked" in phase. The frequency beating of these locked modes results in a very short pulse of high intensity. Mode locking of the laser pulse is achieved by modulating the losses of the laser. An acousto-optic modulator, which produces transverse optical density grating appearing and disappearing periodically, provides the loss introduced by Bragg diffraction and is used for the active mode-locking. The mode-locking is accomplished by a saturable (bleachable at high light intensities) dye absorber. The active mode-locker supports the action of the passive (dye) mode-locker. The active and passive mode-lockers result in the stabilization of the output energy. Individual pulse selection was accomplished with a Pockel cell (an electro-optic device) which allows the selection of single pulse from the mode-locked pulse train.

The laser pulse is separated into two beams by a beam-splitter. One of the beams, used as the excitation source, strikes directly on the device for carriers injection, the other is guided to an ultra-fast detector to provide the reference signal. The theory of the measurement is based on a spatially uniform carrier excitation. A spatial filter was used in the optical setup for that purpose. The incident power was adjusted by optical attenuators to maintain low injection. The low-injection condition was justified through checking the linearity between the strength of the input light and the measured output signal. A 50% beam attenuator was used for that purpose.

2.3.2 Samples and Measurement

Photodiodes with $W >> L$ and $W \approx 0$ from an array of 10 diodes with different W were measured for each doping. The junction area of diodes was $10 \times 45\ \mu m^2$ (except for the diode with $W >> L$ for $N_{DD} = 2.4 \times 10^{19}\ cm^{-3}$, of which the area is $20 \times 100\ \mu m^2$ [6,11]). The typical structure of the photodiodes on the same chip is shown in Figure 2.4. Also shown is the carrier flow under excitation. The very shallow p^+ region, the emitter of the diode, is formed by boron diffusion. The detailed description about the fabrication procedures of the measured diodes can be referred from Wang [11]. The largest diffusion length measured in the doping range investigated is about 10 μm, which is much less than the thickness of the n^+ (base) region (≈ 300 μm). Thus, the

recombination at the bottom surface is negligible. This justifies the boundary condition used in solving the two-dimensional carrier transport (see Section 2.2). The excitation wavelength was chosen to generate carriers very near the semiconductor surface, which, in turn, enhances the diffusion tendency of the minority carriers and increases the resolution in extracting D. The laterally diffused carriers are affected by the surface properties. To satisfy the limitation of the analytical model in Section 2.2, a well passivated surface is required to minimize the effects due to the surface recombination on the carrier transport in the bulk. The thermal oxide provides the surface passivation and isolates the contact from the base. The condition of $S \approx 0$ at the passivated surface was justified experimentally from device with $N_{DD} = 2.4 \times 10^{19}$ cm^{-3} in the steady-state photocurrent measurement [11]. The metal contact covers the entire junction and extends beyond the left junction edge up to a distance much greater than W to eliminate any carrier collection from the left side. To prevent the aluminum spikes, a 1000 Å thick titanium was evaporated before evaporating the aluminum in forming the metal contact. Besides functioning as a light shield, the top metal layer also functions as a contact where the binding wire is attached.

In the measurements, the uncertainty about the values of absorption coefficient α from the literature could be larger than 20%. This uncertainty was found to have minor effects on the measured lateral photocurrent, both from the theoretical and experimental investigations [10,11]. In addition, the uncertainty due to the light

diffraction on the carrier injections was also found insignificant in the measurements [11].

For the samples in the degenerate doping range, the transient photocurrents are in the sub-nanosecond range (corresponding to the GHz frequency range). To accurately measure those parameters, special care was taken in performing the measurements in this frequency range, including the corrections for the parasitic effects and the response limit of the equipment as well as the delay between the diode signal and the reference signal. Figure 2.5 shows a typical picture of the device mounted on the microstrips with the microwave test structure. The devices were mounted on a 50-Ω microstrip fabricated on a Cr-Au metalized alumina (Al_2O_3) substrate. A detailed description of the structure and the fabrication procedure for the micro-strip is given in Appendix A. Two photodiodes on the same chip were bonded to the transmission lines opposite to each other. The impulse response for each diode is measured by connecting one terminal to the oscilloscope while leaving the other unconnected.

The transient responses of the photodiodes were measured using the two-channel Tektronix 11402 digitizer (1 GHz bandwidth, 0.35 ns rise time) or Tektronix 11802 (20 GHz bandwidth) digital oscilloscopes. An ultrafast (42 GHz) GaAs detector is connected to the second channel of the digitizer to provide simultaneously the reference time signal and the reference system response. The results were averaged over responses from a large number of laser pulses (typically 50000), until the response became independent of the number of pulses. The averaging

compensates for the laser pulse intensity variations and reduces the noise. The measured response was corrected for the effect of the parasitic pole, due to the junction and overlap capacitances of the device, and 50 Ω load resistor. The 50 Ω microstrip fixture has no effect on the photodiode transient response measured with 50 Ω input digitizer. The parasitic capacitance of the fixture (transmission line) has to be, however, taken into account (zeroed-out) in determining the junction and the overlap capacitances by measurement using capacitance meter. This can be done by zeroing the meter with the fixture without the bonding wire attached to the device. The junction and overlap capacitances of each photodiode were accurately measured through the HP 4194A impedance analyzer after zeroing-out the capacitance of the transmission line. For the highest doped device ($N_{DD} = 7.2 \times 10^{19}$ cm^{-3}), the parasitic pole was $f_p = 1/2\pi R_L C_{par} \simeq 10^9$ Hz using $C_{par} = 3.2$ pF measured by the impedance meter. Since the results are obtained from the frequency f below 10^9 Hz, the effect of f_p is not very significant. To verify that the bandwidth of the digitizer has a negligible effect on the distortion of the measured signal, the amplitude and the phase responses of the digitizer were measured by taking the Fourier transform of the laser pulse measured with the ultrafast GaAs detector. The photocurrent can be measured either under reverse bias or under short-circuit conditions. When it is measured under the short circuit condition, the peak value of the signal has to be kept well below the open circuit voltage V_{oc} to get a reliable transient response. In the frequency range of this

experiment, we find that the reflected noise from biasing-T significantly affects the transient photocurrent; therefore, we measure the photodiodes under the short-circuit condition without biasing-T, while keeping the peak signal low enough to satisfy the formerly mentioned condition. The total delay due to the electrical and optical path difference between the device and detector channels is about 0.3 ns. Since the shortest lifetime measured in Wang et al. [6] is about 6 ns, the device signal was assumed to be in phase with the light signal detected by the GaAs detector. However, in the present experiment, the 0.3 ns delay is comparable to the shortest lifetimes to be measured, and it should be measured accurately so that the detector signal may serve as an adequate reference. The electrical delay of the transient signal in the transmission line and the fixture was measured through performing TDR (Time Domain Reflectometry) measurement using Tektronix 11802 sampling oscilloscope. The total delay was measured by connecting two nearly identical ultrafast GaAs detectors at both inputs of the digitizer. By comparing the measured signal responses, the measured total delay Δt = 260 ps. The measured results are shown in Figure 2.6 for illustration. Both the optical and electrical delays of the signals between the device and detector were suitably accounted for in the extraction of D_p and τ_p for each doping device. To account for the finite laser pulse width and the system response, we normalize the device response with respect to the reference signal. Since the reference GaAs detector has a rise time much shorter than that of the digitizer, the overall system response is limited by the digitizer.

The highest analyzed frequency for the highest doped device was only about 700 MHz. Therefore, the 1 GHz bandwidth of the digitizer was not a limitation for the measured devices.

2.3.3 Results and Accuracy

The accuracy of D_p strongly depends on the accuracy of W [6]. Due to the limitation of optical microscope, the value of W for each device was measured through a scanning electron microscope and then a correction was made for the very shallow impurity lateral diffusion. The values for τ measured on devices with $W \simeq 0$ are independent of W [6] and, thus, are unaffected by the accuracy of W. The diffusivity D_p was extracted from the devices with W in the range from 1.2 μm to 6.2 μm. The uncertainty of the overlap width ΔW is $\Delta W \simeq \pm 0.1$ μm. Figure 2.7 shows the typical time-domain signal response for the highest doped devices. The noisy signal shown in the figure is the unavoidable feature in such high frequency-range measurements, and it results in the difficulties in extracting the measured parameters. However, all these high frequency noises will be filtered-out after performing the frequency-domain analysis. Therefore, FDTA (Frequency-Domain Transient Analysis) enhances the accuracy in extracted parameters. This advantage overcomes the widely existing difficulties encountered in extracting parameters from measurements with picosecond resolution. Figs. 2.8(a), (b) and 2.9(a), (b) give the frequency domain signal responses of the signals in Fig. 2.7(a) and (b), respectively. The experimental results for other dopings are given and tabulated in Table 2.1.

Table 2.1. Diffusivity D and lifetime τ for different doping densities and the corresponding figures.

Doping density N_{DD} (10^{19} cm^{-3})	Diffusivity D ($\pm$ ΔD) (cm^2/sec)	Lifetime τ (ns)	Corresponding figures
2.4	3.5 ($\pm$ 6%)	6.2	Fig. 2.10 Figs. 2.11a, b.
4.13	2.4 ($\pm$ 5%)	2.5	Fig. 2.12 Figs. 2.13a, b.
5.18	2.8 ($\pm$ 12%)	1.7	Figs. 2.14a, b. Figs. 2.14a, b.
7.18	3.8 ($\pm$ 8.4%)	0.8	Figs. 2.8a, b. Figs. 2.9a, b.

The relative error in the values for the diffusivity ΔD for each doping shown in Table 2.1 is the summation of the errors estimated from fitting the measured response to theory and the error estimated from ΔW. The procedure to obtain the error for D resulted from ΔW is as follows. First, we fit the experimental responses to theory generated by assigning the overlap width W to two different values, W_1 and $W_2 = W_1 + \Delta W$. Then, from the best fits, we graphically determine the diffusivities D_1 and D_2 for W_1 and W_2, respectively. Finally, via D_1 and D_2, $(D_1 - D_2)/D_2$ yields the error in D that resulted from ΔW. The uncertainty of about $\pm$ 0.1 μm in W causes only a small error in extracting D that depends on the value of W. In Table 2.1, for the doping density of $N_{DD} = 5 \times 10^{19}$ cm^{-3}, the larger ΔD than that for other dopings is due to the larger error estimated from fitting the measured response to theory (see Figs. 2.14a, b).

2.4 Discussion

2.4.1 Minority Carrier Lifetime

Figure 2.15 shows the hole lifetime τ_p plotted versus N_{DD}. Also plotted are the previous published data from Si:P epitaxial layers [4], and from bulk wafers [12]. It has been pointed out by Haug [13] that the predominant recombination process in heavily doped silicon is the phonon-assisted Auger recombination PAAR. For a comparison with the

experimental data, the theoretically predicted results for PAAR from Lochmann and Haug [14] are also plotted. Our results are in very good agreement with the data from Dziewior and Schmid [12], but slightly different from those of Swirhun et al. [4]. In Fig. 2.15, all the experimental values for τ_p are substantially lower than the theoretical results predicted from PAAR. We therefore fit our results with the expression [15]

$$\tau_p^{-1} = r_n^n N_{DD} + r_N^n N_{DD}^2 \text{ (sec)} \qquad (2.8)$$

to examine the possible recombination mechanism. In (2.8), $r_n^n N_{DD}$ comes from the trap assisted Auger recombination, $r_N^n N_{DD}^2$ comes from the phonon assisted Auger recombination. The complete ionization for the dopant is assumed when N_{DD} is above the metal-insulator transition, which occurs at about $N_{DD} = 3.8 \times 10^{18}$ cm^{-3} in phosphorous doped Si. In (2.8), the SRH recombination is not included because it is negligible in the degenerate material.

The best fit to our data in Fig. 2.15 yields $r_n^n = 8.1 \times 10^{-13}$ and $r_N^n = 2.2 \times 10^{-31}$. For comparison, Table 2.2 lists the values for r_n^n and r_N^n from other recent works and from theory. Our r_N^n is in good agreement with that from Dziewior and Schmid [12] and with the fit to the literature results reported by Del Alamo [16], but slightly lower than the results in low doping range reported by Landsberg [15]. Tyagi and Van Overstraeten [17] pointed out that one should also consider the possibility of trap assisted Auger transitions through shallow donor levels in explaining the deviation. The calculated r_n^n for this

mechanism for phosphorous is 1.21×10^{-31} cm^6 s^{-1}, which is very close to the experimental results. In obtaining this r_n^n, the ionization energy has to be specified. Since the ionization energy for the shallow donor does not exist in heavily doped silicon, the predicted value loses its meaning. The higher r_N^n from experiment indicates that, in addition to the predominant PAAR, some other competing mechanisms exist in the highly doped n-type Si.

For a summary of all the hole lifetimes measured in Wang et al. [6] and in this work, the lifetime data within the doping range of 10^{18} - 10^{20} cm^{-3} are plotted in Figure 2.16. Also plotted are the theoretically predicted results for PAAR from Lochmann and Haug [14]. Our measured results show that the lifetime is Auger-process limited at N_{DD} above 7×10^{18} cm^{-3}. The deviation between experiment and theory is about a factor of 2 in the Auger coefficient. It is, thus, clear that more theoretical work needs to be done in order to explain the carrier recombination in heavily doped silicon.

2.4.2 Minority Hole Mobility

Figure 2.17 shows the minority hole mobility μ_p(n-type) versus the donor density N_{DD} resulting from this work (T = 296 K). The mobilities are obtained from the diffusivities using the Einstein relation for nondegenerate minority carriers. The error bars for each measured point are from ΔD in Table 2.1. The results are plotted together with μ_p(n-type) from Swirhun et al. [4] and with the majority hole mobility μ_p(p-type) from Thurber et al. [18]. A comparison of the results from

[4] with those from this work shows that μ_p(n-type) decreases with N_{DD} at $N_{DD} \lesssim 4 \times 10^{19}$ cm^{-3}, but increases with N_{DD} at a higher doping range. The increasing μ_p(n-type) versus N_{DD} behavior was also found at the low temperature measurements for the lower doping range [19]. In [4], D_p is obtained from $D_p = L_p^2/\tau_p$ and depends on the uncertainties in the measurement of L_p and τ_p with an overall estimated uncertainty of about 25% [4]. This error is about the same as the dip in Figure 2.17, which led to the conclusion that μ_p saturates at about 130 cm^2/V·s for $N_{DD} > 10^{19}$ cm^{-3}. The new data in Figure 2.17 are obtained directly from frequency responses, which reduces the error since the values of μ_p are found independently of L_p and τ_p. The improved measurement accuracy indicates that the dependence shown by the solid line in Figure 2.17 is reliable. Figure 2.18 shows the ratio of μ_p(n-type) to μ_p(p-type). The plotted results are listed in Table 2.3. For comparison, the ratios for the mobility data from Swirhun et al. [4] are also plotted and are in good agreement with our results. The ratio for the device with $N_{DD} = 2.4 \times 10^{19}$ cm^{-3} is approximately 2.3 and is slightly lower than the theoretical value of 2.8 predicted by Bennett [20]. The calculations [20], based on the assumption of spherically constant energy surface in k-space (or, equivalently, the parabolic band structure), predict a decreasing μ_p(n-type)/μ_p(p-type) ratio with increasing N_{DD}. This contradicts our experimental results for $N_{DD} \gtrsim 4 \times 10^{19}$ cm^{-3}, which show an increasing ratio with N_{DD}. A possible reason for this difference could be attributed to the nonparabolic band structure and energy gap narrowing that actually occur in this high doping range.

TABLE 2.2. Comparison of the Auger coefficients from this work with the literature results.

r_n^n (10^{-13} cm^3 s^{-1})	r_N^n (10^{-31} cm^6 s^{-1})	Method	Reference
	0.72	Theoretical	[14]
	2.80	Experimental fit	[12]
7.8	1.80	Experimental fit	[16]
0.246	11.90	Experimental fit	[15]
8.1	2.22	Experimental fit	This work

TABLE 2.3. Comparison of minority hole mobility μ_p(n-type) and majority hole mobility μ_p(p-type) for T = 23°C. The majority hole mobility is from Thurber et al. [18].

Doping density			Ratio
N_{DD} (10^{19} cm^{-3})	μ_p(n-type) (cm^2/V·s)	μ_p(p-type) (cm^2/V·s)	μ_p(n-type)/μ_p(p-type)
2.40	137.2	60.93	2.25
4.13	94.1	55.86	1.69
5.18	109.8	54.29	2.02
7.18	149.0	52.43	2.84

Figure 2.19. shows the minority hole mobility in the doping range of 10^{18} to 10^{20} cm^{-3}. The data in the range of 10^{18} to 10^{19} cm^{-3} are from previous work [6]. Because of its higher accuracy, the new mobility value for the doping $N_{DD} = 2.4 \times 10^{19}$ cm^{-3} obtained in this work is shown in the figure. No theoretical work has yet been done for Si in this doping range to describe the new effect found in this work. Recently, using phase-shift analysis, Lowney and Bennett [21] calculated both the majority and minority carriers mobility in GaAs for donor densities between 5×10^{16} and 1×10^{19} cm^{-3}. Their results predict that, in the high doping densities, minority mobilities increase with increasing doping density for a short range of densities. The increase of minority mobility with doping density is similar to our finding in silicon. Lowney and Bennett [21] attribute this effect to the reduction of plasmon scattering and the fewer available final states, resulting from the Pauli exclusion principle, into which the majority carriers may scatter. In their calculation of the carrier-carrier scattering, due to the fact that rigorous formulisms are still not available, they account for the effect by treating the scattering particles as classical particle and then removing those states with energies below Fermi energy. No physics model was used in their calculation to account for the fewer available states for the scattering carriers. Similar as Bennett's work [20], the band distortion due to the heavy doping effect and the effect due to the randomness of the impurity atoms are also disregarded. One more plausible explanation to describe the higher minority mobility with

increasing doping density is the smooth out of the Coulomb force of impurities by the very high concentration of majority carriers. This is because the correlation of scattering impurities smooths out the randomness of the impurities, which decreases the carrier scattering. The correlation effect becomes more significant at low temperatures and for high doping densities and has been demonstrated on the surface-oxide charges scattering by Ning and Sah [22]. The correlation model [22] predicted a result with the same trend as our measurement and is more physics based than that of Lowney and Bennett [21]. To further study the transport mechanism, an inclusion of the correlation effect to the minority carrier transport mechanisms is essential.

To perform the self-checking for all the transport parameters obtained here, we calculate the diffusion length L_{AC} using $L_{AC} = (D_p\tau_p)^{1/2}$ and then compare it with the L_{DC} from an independent experiment [7]. Table 2.4 lists all the measured results. The last column shows the relative deviation (self-checking error) for each device. The relative deviations for all devices are less than 8%. Because a small uncertainty exists in the conversion from the measured ρ to N_{DD} for high doping, the values for the resistivity ρ are also listed.

With the higher accuracy for D_p afforded by our method, we can reinterpreted some literature data for the apparent energy gap narrowing defined by $p_0D_p = (n_i^2/N_{DD})D_p \exp(\Delta E_g^{app}/kT)$ [16]. We use the measured results p_0D_p by del Alamo and the D_p from this work to calculate the ΔE_g^{app}. Figure 2.20 shows the apparent energy gap narrowing ΔE_g^{app} plotted versus N_{DD}. Also shown are the ΔE_g^{app} values from del Alamo [16].

TABLE 2.4. Accuracy check for the simultaneously measured transport parameters. The L_{DC} is the diffusion length from DC measurement [7]. The L_{AC} is the diffusion length calculated from the results of this work.

N_{DD}	ρ	L_{DC}	D_p	τ_p	L_{AC}	$\frac{L_{AC} - L_{DC}}{L_{AC}}$
($10^{19}cm^{-3}$)	(ohm-cm)	(μm)	(cm^2/sec)	(ns)	(μm)	(%)
2.40	0.002862	1.56	3.5	6.2	1.47	5.90
4.13	0.001708	0.83	2.4	2.5	0.78	7.15
5.18	0.001384	0.74	2.8	1.7	0.69	7.26
7.18	0.001025	0.51	3.8	0.8	0.55	7.50

2.5 Conclusions

In this chapter, we report the values for the minority hole transport parameters directly determined by performing transient measurements in the degenerately doped n-type Si. Due to the experimental difficulties encountered in this doping range, we verify the accuracy of the results by a self-consistent check with the independently measured L_{DC} . The self-consistency check shows a good agreement (better than 8%). The dependence of the minority hole mobility on doping density shows a minimum at $N_{DD} \sim 4 \times 10^{19}$ cm^{-3} and increase for higher dopings. With the verified accuracy, the measured results reported here are believed to be important both for device modeling and for understanding of the transport physics in heavily doped silicon. The Auger coefficient determined from the experiment is however higher than the theoretical value for PAAR. To further investigate the carrier recombination and transport mechanisms, additional study of the temperature dependence of the transport parameters is necessary.

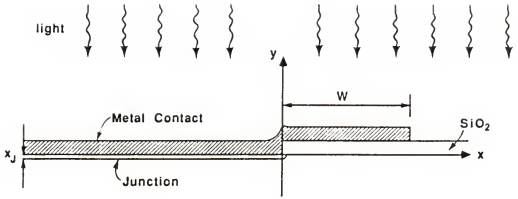

Fig. 2.1 Schematic illustration of the photodiode showing the exposed and covered regions.

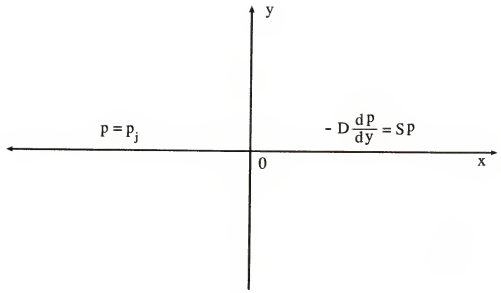

Fig. 2.2 Illustration of the semi-infinite geometry and the mixed boundary conditions.

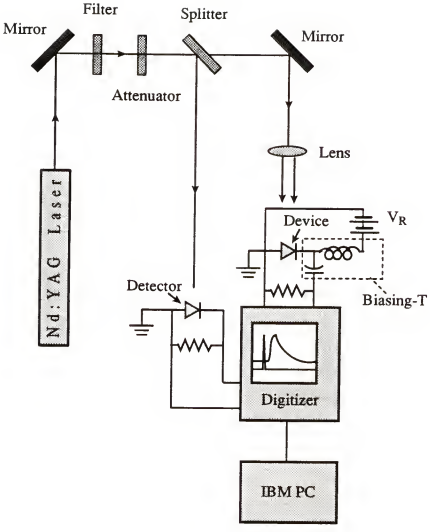

Fig. 2.3 Experimental setup for the transient measurements.

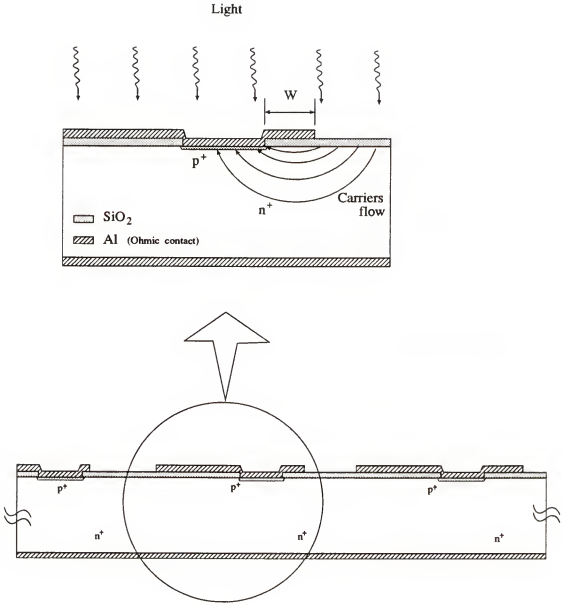

Fig. 2.4 Device cross-section illustrating the photodiodes with different overlap width W and the two dimensional carrier flow in a n^+ bulk region.

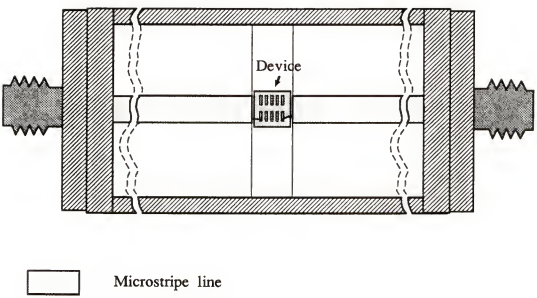

Fig. 2.5. Photodiodes mounted on the microstrip and the microwave test fixture. Two photodiodes on the same chip are bonded to the microstrips leading to SMA connectors on the opposite sides of the fixture.

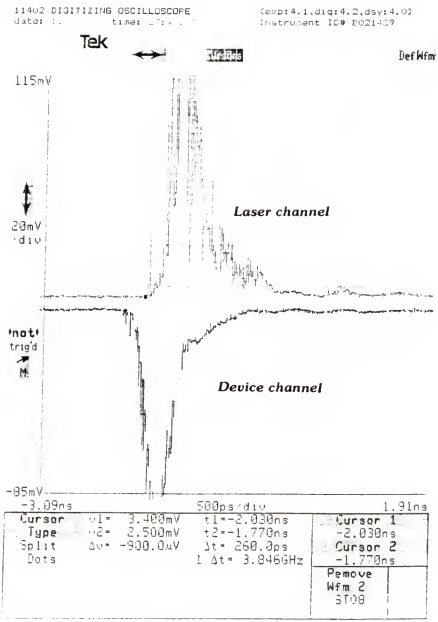

Fig. 2.6 Hard copy of the laser signals measured to illustrate the time delay between the two channels of the digitizer.

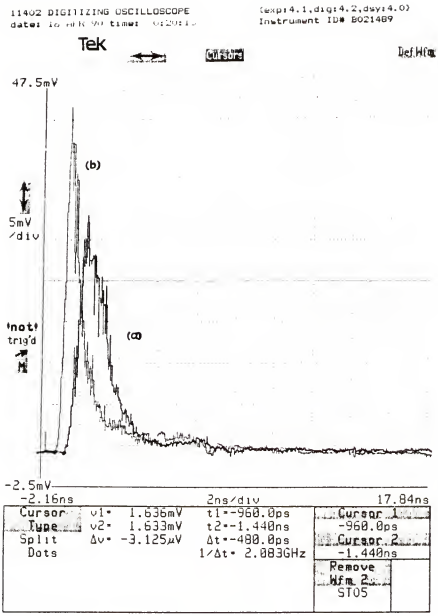

Fig. 2.7 Time domain large overlap (a) and small overlap (b) signal responses for $N_{DD} = 7.2 \times 10^{19}$ cm^{-3} device. (a) the signal was measured from device with $W \simeq 1.57$ μm and $C_j \simeq 3.22$ pF. (b) the signal was measured from device with $W \simeq 0.57$ μm and $C_j \simeq 3.21$ pF.

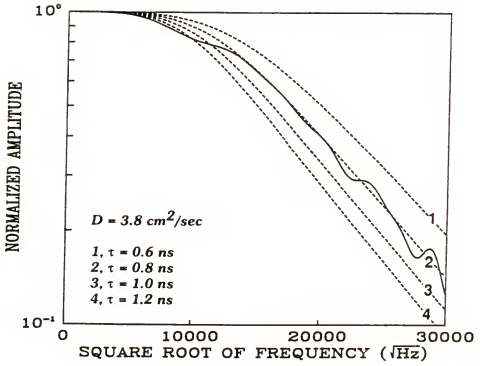

(a)

Fig. 2.8. Theoretical and experimental frequency response for small overlap device (W ≈ 0.57 μm, C_J ≈ 3.21 pF) measurement. The plots are normalized with respect to the zero frequency response. The doping is $N_{DD} = 7.2 \times 10^{19}$ cm^{-3}.
(a) Amplitude versus frequency plots for the analysis. The solid line is the Fourier transformed signal from Figure 2.7 (b). The dash lines are the theoretical plots obtained with fixing D = 3.8 cm^2/sec and changing τ from 0.6 to 1.2 ns.
(b) Phase versus frequency plots for the same analysis.

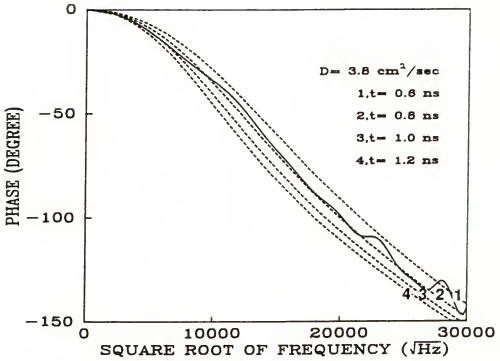

(b)

Fig. 2.8. (continued)

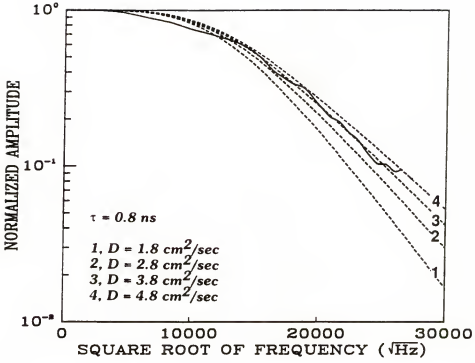

(a)

Fig. 2.9. Theoretical and experimental frequency response for large overlap device (W ≈ 1.57 μm, C_j ≈ 3.22 pF) measurement. The plots are normalized with respect to the zero frequency response. The doping is $N_{DD} = 7.2 \times 10^{19}$ cm^{-3}.

(a) Amplitude versus frequency plot for the analysis. The solid line is the Fourier transformed signal from Figure 2.7 (a). The dash lines are the theoretical plots obtained with fixing τ = 0.8 ns and changing D from 1.8 to 4.8 cm^2/s.

(b) Phase versus frequency plot for the same analysis.

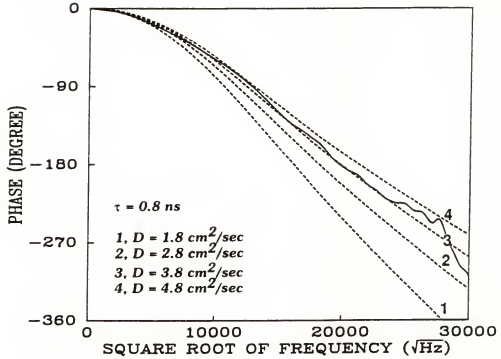

(b)

Fig. 2.9. (continued)

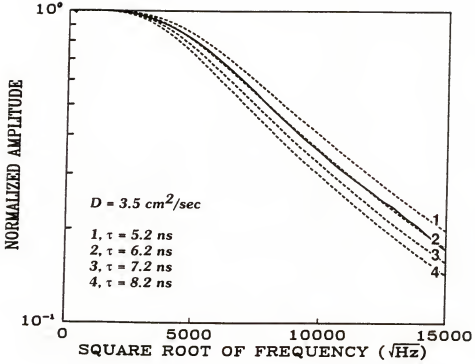

Fig. 2.10 Amplitude plot for the theoretical and experimental frequency response for small overlap device (W = 0.25 μm, C_j = 3.1 pF) measurement. The doping is $N_{DD} = 2.4 \times 10^{19}$ cm^{-3}. The solid line is the Fourier transformed signal from the time domain signal. The dash lines are the theoretical plots obtained with fixing D = 3.5 cm^2/sec and changing τ from 5.2 to 8.2 ns.

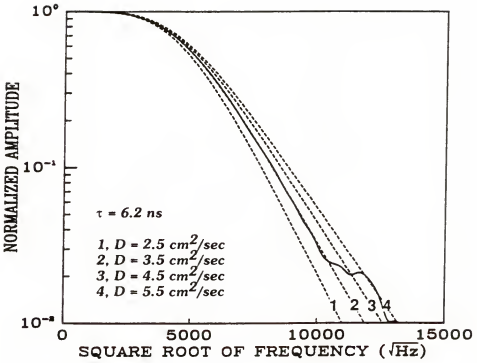

(a)

Fig. 2.11. Theoretical and experimental frequency response for large overlap device (W = 6.1 μm, C_j ≃ 5.1 pF) measurement. The plots are normalized with respect to the zero frequency response. The doping is $N_{DD} = 2.4 \times 10^{19}$ cm^{-3}.
(a) Amplitude versus frequency plot for the analysis. The solid line is the Fourier transformed response from the time domain signal. The dash lines are the theoretical plots obtained with fixing τ = 6.2 ns and changing D from 2.5 to 5.5 cm^2/s.
(b) Phase versus frequency plot for the same analysis.

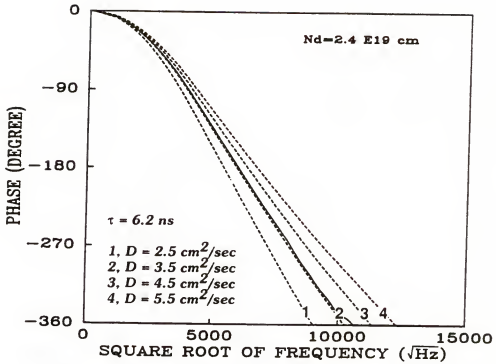

LARGE OVERLAP FREQUENCY RESPONSE

(b)

Fig. 2.11. (continued)

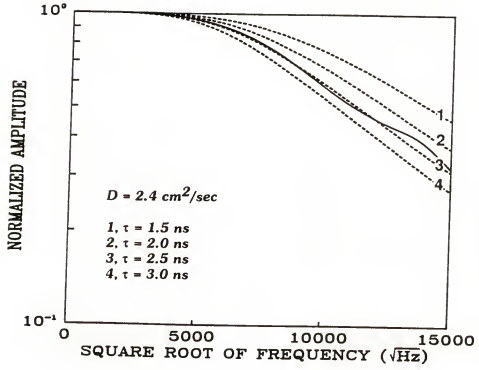

Fig. 2.12 Amplitude plot for the theoretical and experimental frequency response for small overlap device ($W \simeq 0.23$ μm, $C_i \simeq 4.51$ pF) measurement. The doping is $N_{DD} = 4.1 \times 10^{19}$ cm^{-3}. The solid line is the Fourier transformed signal from time domain signal. The dash lines are the theoretical plots obtained with fixing $D = 2.4$ cm^2/sec and changing τ from 1.5 to 3.0 ns.

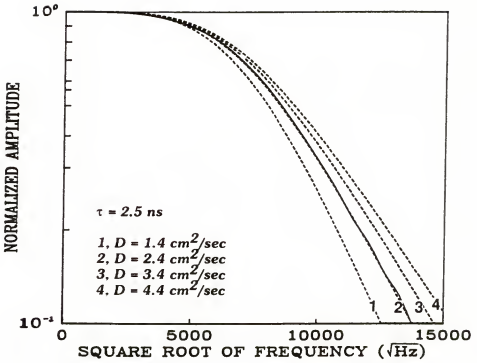

(a)

Fig. 2.13. Theoretical and experimental frequency response for large overlap device ($W \simeq 2.47$ μm, $C_j \simeq 4.58$ pF) measurement for $N_{DD} = 4.1 \times 10^{19}$ cm^{-3} device.
(a) Amplitude versus frequency plot for the analysis. The dash lines are the theoretical plots obtained with fixing $\tau = 2.5$ ns and changing D from 1.4 to 4.4 cm^2/s.
(b) Phase versus frequency plot for the same analysis.

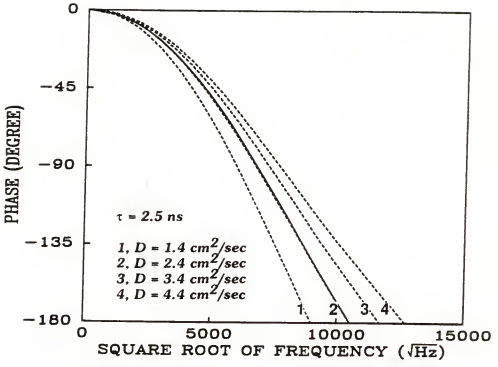

LARGE OVERLAP FREQUENCY RESPONSE

(b)

Fig. 2.13. (continued)

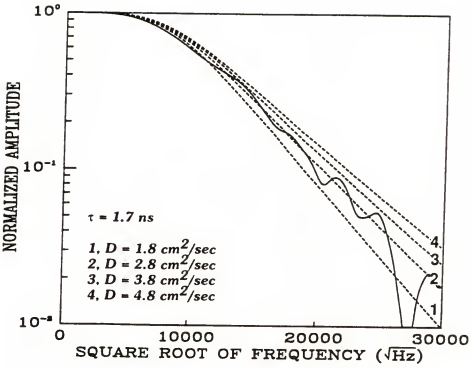

(a)

Fig. 2.14. Theoretical and experimental frequency response for large overlap device ($W \simeq 1.15$ μm, $C_j \simeq 4.04$ pF) measurement for $N_{DD} = 5.18 \times 10^{19}$ cm^{-3} device.
(a) Amplitude versus frequency plot for the analysis. The solid line is the Fourier transformed response from the time domain signal. The dash lines are the theoretical plots obtained with fixing $\tau = 1.7$ ns and changing D from 1.8 to 4.8 cm^2/s.
(b) Phase versus frequency plot for the same analysis.

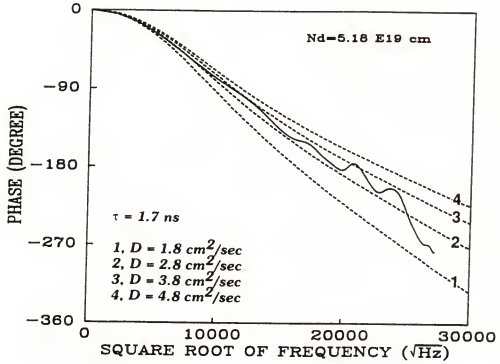

LARGE OVERLAP FREQUENCY RESPONSE

(b)

Fig. 2.14. (continued)

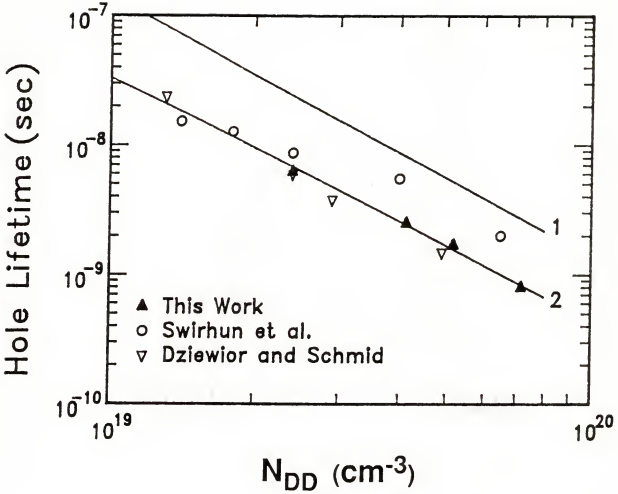

Fig. 2.15. Minority hole lifetime versus doping concentration at T = 296 K. Curve 1 corresponds to the theoretical PAAR from [14]. Curve 2, based on equation (4.1), is the best fit to the points measred in this work.

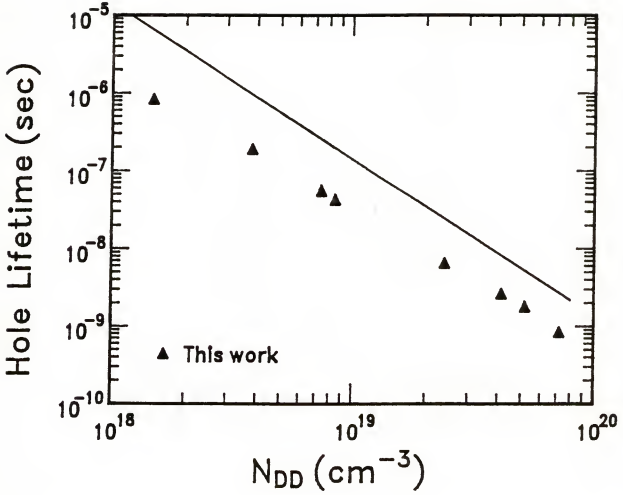

Fig. 2.16. Minority hole lifetime versus doping concentration for N_{DD} within the doping range 10^{18} - 10^{20} cm^{-3}. The solid line is from the theoretical PAAR [14].

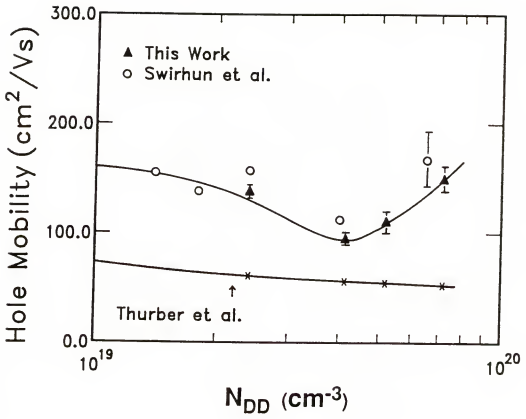

Fig. 2.17. Minority hole mobility plotted versus doping concentration at T = 296 K. The bottom solid line shows the majority hole mobility. "*" is the majority hole mobility corresponding to the dopings used in this work. The top solid line is the graphical fit for the measured data extended to lower dopings measured previously. The error margin is from Table 2.1.

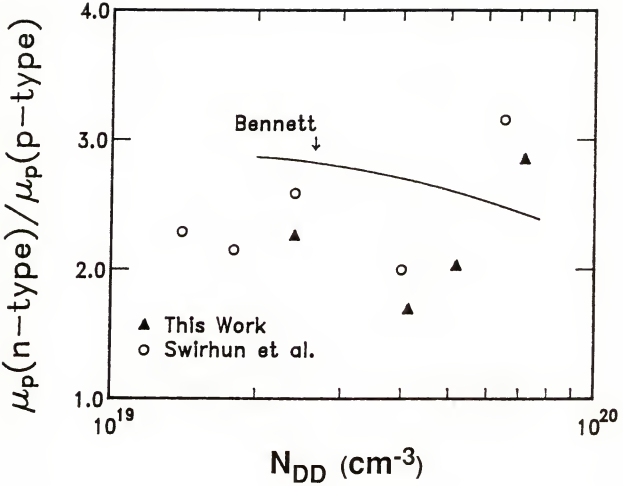

Fig. 2.18. Experimental hole mobility ratio plotted versus doping concentration. Also plotted is the theoretical mobility ratio from [20].

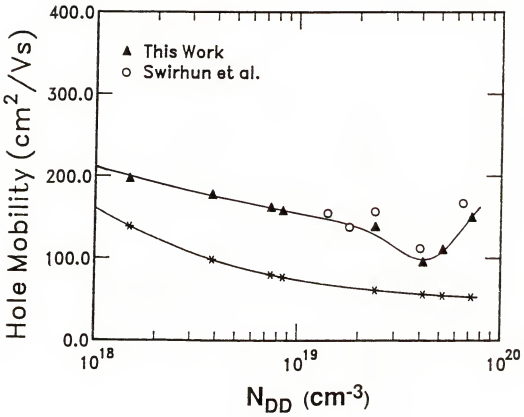

Fig. 2.19. Minority hole mobility plotted versus doping concentration at T = 296 K. The bottom solid line shows the majority hole mobility. "*" is the majority hole mobility corresponding to the dopings in this work. The top solid line is the graphical fit for the measured data.

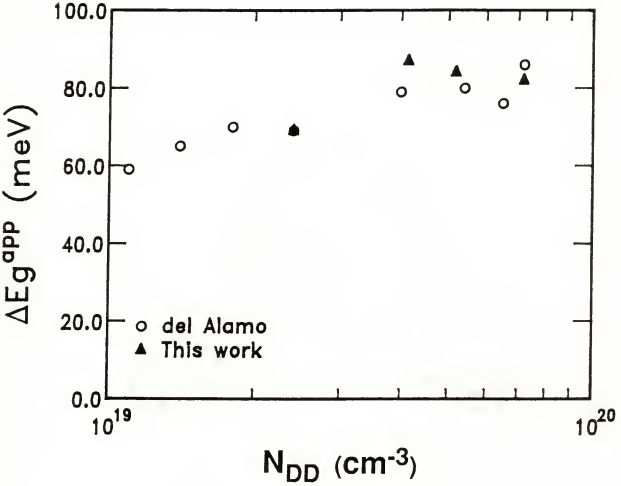

Fig. 2.20. Apparent energy gap narrowing versus doping.

CHAPTER 3
TEMPERATURE DEPENDENCE OF MINORITY HOLE MOBILITY IN HEAVILY DOPED SILICON

No previous experiment has addressed the question if there is difference in scattering mechanisms for minority as opposed to majority holes in heavily doped silicon. A direct approach to examine this is to investigate the temperature dependence of the mobility. In this chapter, the temperature dependence of the minority hole mobility $\mu_p(N_{DD},T)$ in heavily doped n^+ silicon in the doping range from 10^{18} to 2.4×10^{19} cm^{-3} is investigated. The preliminary measurement results show that the mobility is strongly temperature dependent. For temperatures below 200 K the minority carrier hole mobility increases with increasing doping, in contrast to the opposite dependence for the majority hole mobility in p^+ silicon. Analytical fits to the measured data useful for low temperature modeling for bipolar devices are given.

3.1 Introduction

Because of the recent interest in the cryogenic operation of bipolar devices [23], accurate values for the minority carrier transport parameters at low temperatures are essential. Swirhun et al. [24] measured the temperature dependence of the electron mobility μ_n

and energy gap narrowing ΔE_G in p^+ Si. The important result obtained was that the minority carrier μ_n increases with increasing doping at low temperatures, while the majority carrier μ_n in n^+ Si always decreases with increasing doping because of the impurity scattering. To explain the behavior of the minority μ_n, it was suggested [24] that the high concentration of the majority carriers may effectively screen the charged impurities from the minority carriers which diminishes the ionized impurity scattering for the minority carriers.

In this work we present similar results for the minority carrier hole mobility μ_p in n^+ Si in the doping range from 1.5×10^{18} cm^{-3} to 2.4×10^{19} cm^{-3}.

3.2 Experimental and Results

The experimental method, established earlier [5], is based on the measurement of the lateral photocurrent of photodiodes fabricated in uniformly doped substrates. The method yields simultaneously and independently L, D, and τ from the same device and was used to measure the transport parameters at 296 K in n^+ Si [6,7]. Here, we report the extension of these measurements to temperatures from 30 K to 300 K for hole diffusion length L_p and and mobility μ_p. The experimental setup is basically the same as in Wang et al. [6,7], except that, instead of employing the Ar laser, we used a tungsten light source filtered by a narrow-band filter ($\lambda \simeq 0.45$ μm) to obtain a spatially uniform light. The devices mounted on TO-5 headers were placed in a temperature

controlled He cryostat. The temperature was controlled with a precision of about ± 0.2 K. The substrate doping was determined from measured resistivity and majority carrier mobility [6]. Since the method is based on the collection of the photogenerated carriers, a possible partial impurity freezeout for the lowest doped devices at low temperatures would not affect the results.

Figure 3.1 shows the measured temperature dependence of L_p for T from 30 K to 300 K for four different dopings. The strongest temperature dependence was found for the highest doped device with $N_{DD} = 2.4 \times 10^{19}$ cm^{-3} for which $L_p(77\ K)/L_p(300\ K) \simeq 1.7$. Disregarding the magnitude of L_p and looking at the temperature dependence of the results, a remarkable behavior can be seen. As doping increases from 1×18^{18} cm^{-3} to 2×10^{19} cm^{-3}, the temperature coefficient of $L_p(T)$ changes from positive to negative. To obtain $\mu_p(N_{DD},T)$ from the measured $L_p(N_{DD},T)$, (Figure 3.1), we use

$$\mu_p(N_{DD},T) = (q/kT)[L_p^2(N_{DD},T)/\tau_p(N_{DD},T)]. \quad (3.1)$$

The values for $\tau_p(N_{DD})$ for the four samples in Figure 3.1 were measured accurately at 296 K [6] (see also the caption of Figure 3.1). The values are close to those of Dziewior and Schmid [12] at 300 K for the Auger limited lifetime. The lifetime data in [12] measured at 77 K and 300 K show only a small variation (τ is about 20% higher at 77 K in the comparison with 300 K value). Since our τ_p values at 295 K are close to the 300 K values in Wang et al. [6], we linearly extrapolate our τ_p data [6] over the 30 K - 300 K range. The results obtained from (3.1) after minor adjustment for $\tau_p(T)$ just described are shown in Figure 3.2. The number of the generated excess carriers in the measurement is

estimated to be about 10^9 cm^{-3} from the photocurrent of the device with W ≈ 0 μm. This assures the low injection conditions and the validity of the Einstein relation for the nondegenerate case, which was applied in (3.1).

From Figure 3.2, we can see that μ_p increases with decreasing T, with faster increase for larger doping. The highest mobility increase within T = 30 K - 300 K is by a factor of about 19 for the highest doped device with $N_{DD} = 2.4 \times 10^{19}$ cm^{-3}. These results rely on the literature values for the temperature dependence of τ_p from [12], causing some uncertainty in $\mu_p(T)$. Since the measured variations in τ_p are minor, they cannot explain the large increase in μ_p, particularly for the highest doped device.

The minority hole mobility from Figure 3.2 for the three lowest doped devices can be approximately fitted for 100 K < T < 295 K with

$$\mu_p(N_{DD},T) = A\ T^{-m}\ \ cm^2/Vs, \qquad (3.2)$$

where A and m are fitting parameters listed in Table 3.1. The best fits were obtained by using a least-square-root fitting computer program. For $N_{DD} = 2.4 \times 10^{19}$ cm^{-3}, m = 1.33 for a wide range of T = 30 K - 300 K, which is close to the theoretical value of m = 1.5 for acoustic phonon scattering [25]. The fitting parameter m increases monotonically with the doping. The mobility for the three lowest doped devices reaches a peak value at T ≈ 50 K. However, for the highest doped device, μ_p increases monotonically as T decreases with no peak observed in the temperature range of the measurement. The $\mu_p = AT^{-m}$ dependence for T > 100 K for all devices is similar to that for the majority carriers and suggest the dominance of the lattice scattering for T > 100 K.

Table 3.1. Best fitting parameters to (3.2) obtained from the mobility data for devices with $N_{DD} < 10^{19}$ cm^{-3} at 100 K < T < 300 K and for $N_{DD} = 2.4 \times 10^{19}$ cm^{-3} at 30 K < T < 300 K.

N_{DD} (10^{18} cm^{-3})	A	m
1.48	1848	0.39
3.05	23749	0.86
7.13	150050	1.19
24.0	338231	1.33

Comparison of the minority hole mobility data, shown in Figure 3.2, with the corresponding data available from the literature for the majority hole mobility [26,27], shows a much stronger temperature dependence for the minority hole mobility. For the majority holes, the mobility always decreases with increasing doping at any T and is insensitive to T in heavily doped region, as expected when the impurity scattering is significant. However, the experimental results in Figure 3.2 show that the minority hole mobility increases with increasing doping for $T \leq 200$ K. Similar results were reported for the minority electron mobility [24]. Since the measurement method [24] is different from that used here, similarities between the results affirm the reliability of the results from both experiments.

Figure 3.3 shows the temperature dependence of μ_p(n-type)/μ_p(p-type) = D_p(n-type)/D_n(n-type). The minority hole mobility μ_p(n-type) in this figure is from the fit given by (3.2), and the majority hole mobility μ_p(p-type) is from the empirical fit for the temperature range T = 200 K - 500 K [26]. The ratio increases strongly as T decreases for the most heavily doped device, and is only weakly dependent on T for the lowest doped device. The ratio at T = 296 K for the N_{DD} = 2.4 x 10^{19} cm^{-3} device is ≈ 2.9, which is close to the theoretical prediction for similar doping density [20]. At T = 77 K, the ratio for this device is estimated to be ≈ 19, when employing Chapman's results [27] for μ_p(p-type). Comparison of the temperature dependence of the hole mobility from this work with that for the minority electrons from [24] shows a stronger dependence for the electrons.

At a fixed T, the mobility as a function of N_{DD} can be fitted by the following analytical expression,

$$\mu = \mu_{min} + \frac{\mu_0}{1 + (N_{DD}/N_{ref})^{\beta}} . \qquad (3.3)$$

Here, μ_{min}, μ_0, N_{ref} and β are fitting parameters determined by optimization program which minimizes the fitting error. Figure 3.4 shows the analytical fits according to (3.3) for the minority hole mobility at different temperatures. The values of the four fitting parameters are shown in Table 3.2. It is interesting to point out that for T = 295 K, μ_p slightly decreases with N_{DD}, as expected for ionized impurity scattering, but μ_p increases with N_{DD} for low temperatures.

Table 3.2. Best fitting parameters to (3.3) for the hole mobility at different temperatures.

T (K)	μ_{min} (cm^2/Vs)	μ_0 (cm^2/Vs)	$N_{ref} \times 10^{18}$ (cm^{-3})	β
295	126.95	107.85	2.398	0.269
250	135.31	138.07	1.798	- 0.173
220	144.53	183.12	2.049	- 0.225
190	161.14	179.86	2.165	- 1.153
160	131.00	302.22	2.267	- 0.909
131	82.09	476.16	2.147	- 1.057
101	89.43	784.39	3.881	- 0.955
82	185.94	997.20	7.732	- 1.103
60	310.79	1481.46	11.368	- 1.608
45	366.01	2021.93	11.013	- 2.545
39	342.87	3207.88	15.189	- 2.212

3.3 Discussion and Conclusions

The temperature dependence of the minority hole diffusion length and mobility in n^+-Si was investigated for the first time. The preliminary results show that the minority hole mobility is strongly dependent on the temperature, especially for higher doped devices. At low temperatures, the mobility increases with increasing doping. This behavior is very anomalous, because adding more impurity centers leads to more scattering and, therefore, lowers the mobility. It is well known that high doping causes energy gap narrowing and significantly modifies the band structure at the band edges [28]. The modifications of the minority-carrier band affect the carrier transport and are thought to be responsible for the observed anomalous mobility behavior.

A detailed theoretical study is, however, required to explain the observed results. Also, further experiments, including simultaneous measurement [6] of all three transport parameters (L, D, and τ), are necessary to confirm the accuracy of the present results.

In the work done by Cressler et al. [23], the temperature dependence of the current gain $\beta(T)$ of bipolar transistors is assumed to be insensitive to the temperature effect on D_p. Since the $\beta(T)$ reported has the Arrhenius expression (Eq. (10) in Cressler et al. [23]), to justify the assumption in Cressler et al. [23], we plot D_p in a logarithmic scale as a function of the reciprocal temperature in Figure 3.5. For the advanced BJT with emitter doping of 10^{21} cm^{-3} and base doping of 10^{18} cm^{-3}, Figure 3.5. shows that the effects of D(T) on $\beta(T)$ could be as significant as the effect due to energy-gap narrowing.

In conclusion, the temperature dependence of the minority hole and electron mobilities must be considered in analyzing the low temperature properties of bipolar devices. Although the temperature dependence of the minority carrier mobilities is not fully understood at the present, the available data for both electrons and holes are useful for device modeling and predicting low temperature device performance.

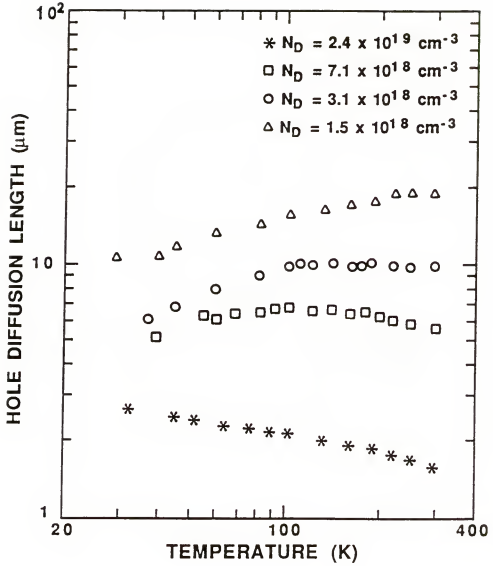

Fig. 3.1. Temperature dependence of the minority hole diffusion length for four substrate dopings. The hole lifetimes measured at 296 K are: $\tau_p \simeq 800$ ns (N_{DD} = 1.5 x 10^{18} cm^{-3}), $\tau_p \simeq 260$ ns (N_{DD} = 3.1 x 18^{18} cm^{-3}), $\tau_p \simeq 56$ ns (N_{DD} = 7.1 x 10^{18} cm^{-3}), and $\tau_p \simeq 6$ ns (N_{DD} = 2.4 x 10^{19} cm^{-3}).

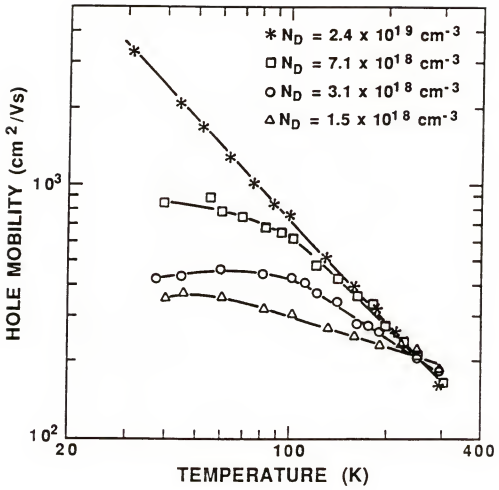

Fig. 3.2. Temperature dependence of the minority hole mobility derived from Fig. 3.1 and equation (3.1).

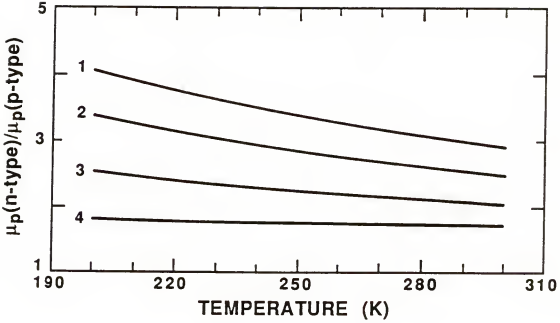

Fig. 3.3. Temperature dependence of the ratio of the minority and majority hole mobilities for $N_{DD} = 2.4 \times 10^{19}$ (1), $N_{DD} = 7.1 \times 10^{18}$ (2), $N_{DD} = 3.1 \times 10^{18}$ (3), and $N_{DD} = 1.5 \times 10^{18}$ cm^{-3} (4).

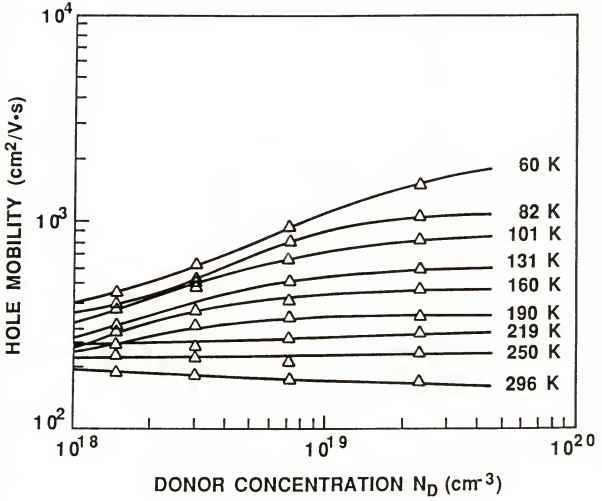

Fig. 3.4. Hole mobility in n^+ Si:P versus doping at different temperatures. The solid lines show the best fits to the experimental results (Δ).

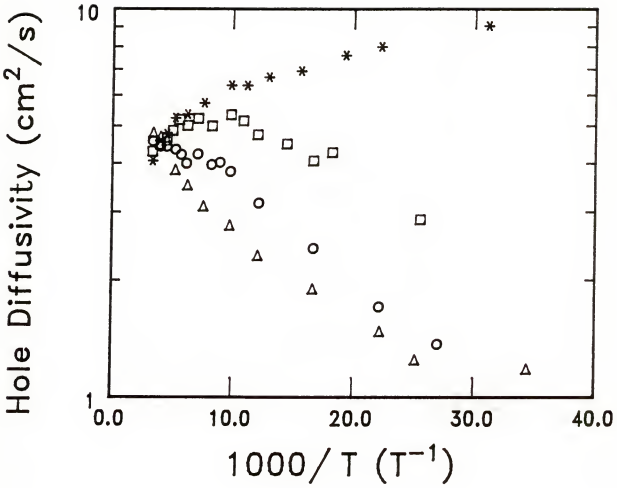

Fig. 3.5. Temperature dependence of the minority hole diffusivity. The symbols represent the same dopings as those in Fig. 3.3.

CHAPTER 4
MINORITY-CARRIER LIFETIME AND SURFACE RECOMBINATION VELOCITY MEASUREMENT BY FREQUENCY-DOMAIN PHOTOLUMINESCENCE (FDPL)

A new nondestructive and contactless experimental method for measurement of the minority-carrier lifetime τ and surface recombination velocity S is presented. The method is based on the analysis of the photoluminescence (PL) time decay after laser excitation. The PL decay is analyzed in the frequency domain, which allows an accurate extraction of both τ and S independently from the same measurement. Closed-form analytical solutions are derived for the PL signal in the frequency domain. The new technique is capable of measuring accurately sub-nanosecond lifetimes. It can also measure S on heavily doped semiconductors. The method (Frequency-Domain Photoluminescence, FDPL) is demonstrated on Si, GaAs, and InP materials.

4.1 Introduction

The minority-carrier recombination lifetime τ is important for both fundamental and technological reasons. For the semiconductor industry, the knowledge of τ enables to monitor the defect density and uniformity of wafers after different processing steps. In addition, τ can be used in screening starting material prior to the device

fabrication. Performance of many devices is affected by the minority-carrier recombination characterized by τ. It also well recognized that the surface recombination plays a decisive role in determining the properties of many semiconductor devices. This is true in particular for the devices using III-V and other compound materials, where the surface passivation is much less effective than that for Si.

Due to its nondestructive and contactless nature, the photoluminescence (PL) decay measurement has been widely used as a technique for the extraction of τ. PL decay was also used extensively in studying the recombination mechanisms in heavily doped Si [4,12,29,30] by measuring the lifetime. In the PL measurement, the decay of the emitted radiation intensity I_{PL} is monitored after the light pulse excitation is terminated. The bulk lifetime is extracted by observing the exponential decay of the measured $I_{PL}(t) \propto \exp(-t/\tau)$. When the surface recombination velocity S is large ($\geq 10^4$ cm/s), the PL signal corresponds actually to the composite luminescence of the excess carriers recombining in the bulk and on the surface. Different approaches were suggested to model the carrier dynamics, and particularly to evaluate the effect of the surface recombination on the accuracy of the PL decay method [31-34]. For the purpose of nondestructive testing, it is difficult to achieve low S without surface passivation. Thus, without an independent knowledge of S, the accuracy of the extracted τ is very limited. Since the surface recombination prevents a purely exponential PL decay [33], the extraction of τ is not so straightforward when compared with the small S case. To improve the measurement accuracy, it was suggested in Tyagi et al. [31] and Misiakos et al. [33] to analyze only the tail part of

the signal after the excess charges diffuse into the bulk and recombine there to give an approximately exponential decay. Even with this improvement, the error in τ, as estimated by Misiakos et al. [33], is about 20%. Hooft and Opdorp [34] proposed an alternative approach to deduce τ and S from the nonexponential $I_{PL}(t)$ by using a contour plot. A very important conclusion from the analysis in [33] is that the decay rate is independent of the lateral spatial distribution of the excitation. The same conclusion was also reached in a later paper [34]. This means, that a finely focused laser beam is absolutely not necessary for the PL decay measurement. In fact, a defocused laser beam is more preferable for the achievement of low injection conditions, because it prevents local high injection and possible heating. Regardless of all these improvements, as can be found in most of the time domain transient measurements, when the magnitude of $I_{PL}(t)$ decays to about 5% of its initial peak value, the magnitude of the noise becomes comparable to the decay signal. Therefore, the unavoidable noisy picture prevents a more accurate extraction of τ.

Regarding the surface characterization, Nelson et al. [35,36], evaluated S in GaAs layers with different thicknesses d by measuring the effective lifetime τ_{eff} by PL decay, using an approximation $1/\tau_{eff} = 1/\tau + 2S/d$. This approach is subject to two limitations: (i) For an accurate extraction of τ_{eff}, the relation $S << 2D/d$, where D is the diffusivity, has to be satisfied [37]. (ii) For the evaluation of S, layers with different thicknesses $d < 1$ μm, but with the same interface properties, are required [35,36]. By measuring the conductivity decay using an inductive coupling, Yablonovitch et al. [38] estimated S by

taking the difference in the reciprocal filament lifetime (τ_{eff}) between the chemically prepared samples and the reference sample. This approach is, however, subject to the same limitations as that in (i) above. Therefore, it applies only to thin films with small S. Recently, Ahrenkiel et al. [39-41] performed PL decay measurements to extract τ and S in different III-V materials. S was obtained by comparing the experimental PL signal with the theoretically predicted time-domain signal generated by assigning known values to τ and D. For sub-nanosecond lifetime measurements, the extraction procedure from the time-domain experiment is, however, not very straightforward. To account for the finite response of the measurement instrument, such as photomultiplier tube (PMT), a deconvolution of the system response must be done to recover the real PL signal. Furthermore, when laser pulse width is not much shorter than τ, another deconvolution for the laser response has to be also performed.

The above discussion clearly shows that a reliable and accurate method to determine τ and S from the same PL decay signal is still not available. Here, we present a new measurement technique to simultaneously measure τ and S in a semiconductor wafer. Instead of analyzing the transient PL response in the time domain, we analyze the response in the frequency domain through performing the Fourier transform of $I_{PL}(t)$. The FDPL signal $I_{PL}(\omega)$ is analyzed by fitting the amplitude and phase components with those from the theoretical model in the frequency range of interest. Light sources with different wavelengths λ are used in the measurements. With light, depending on

λ, the generated carriers can be either very near the surface or in depth, and the generation depth is well controllable. As shown in Section 4.2, for the nearly uniformly absorbed excitation, $I_{PL}(\omega)$ is insensitive to S and the frequency response is primarily a function of τ. For the strongly absorbed excitation, however, the response is a function of both τ and S with the corner frequency more sensitive to τ, but with the slope more sensitive to S. Thus, due to the different dependencies of the responses on the excitation conditions, by analyzing the frequency responses for the two separate experiments, τ and S can be extracted accurately and simultaneously. The effects due to the finite response of the measurement system and the finite laser pulse width can be taken care of by normalizing the output response to the input response. Hence, this technique is not subject to the complicated procedure required in the time domain analysis and has more potential for sub-nanosecond lifetime measurements.

It is important to note, that the frequency-domain analysis exploits the entire measured signal, instead of focusing only on a particular part of the signal. This overcomes one of the main shortcomings of the time-domain analysis that uses only the tail portion of the signal. In addition, by performing the Fourier transform, the high frequency noise that disturbs the accuracy in the time-domain analysis does not appear in the frequency range required for the analysis. Therefore, the accuracy and the reliability of the extracted parameters is much improved. The comparison of the two approaches and the advantages of the FDPL over the time-domain analysis

are further discussed in Section 4.3.2. A quantitative comparison describing the confidence levels of the extracted parameters from these two approaches is given in Section 4.4.

Although, the model presented here is demonstrated by measuring the luminescence to monitor the excess charge decay rate, it is generally applicable to other methods that monitor the excess carrier density. These include microwave reflection [42], infrared absorption [43], and conductivity decay by inductive coupling [38,44]. Throughout this work, the low injection conditions are assumed to ensure a meaningful lifetime and to preserve a linear system, such that the Fourier transform is applicable.

The FDPL technique is especially powerful for the characterization of surface properties of the III-V and II-VI compound materials, for which the surface passivation techniques and characterization are not yet well developed.

4.2 Frequency-Domain Photoluminescence Decay (FDPL) for Semi-Infinite Slab

4.2.1 Analytical Expression in the Frequency Domain

Figure 4.1 illustrates the semi-infinite semiconductor wafer used for the analysis. The laser light is chosen as the excitation source for illustration, but the analysis is also valid for other kinds of sources, such as E-beam. The wafer is uniformly doped-n type material (extension to p-type is straightforward).

Assuming that the transport parameters are excitation independent, the three-dimensional continuity equation can then be simplified to the one-dimensional expression [33]

$$\frac{\partial P}{\partial t} = D \frac{\partial^2 P}{\partial z^2} - \frac{P}{\tau} + G(t)\ (1 - R)\ \alpha\ e^{-\alpha z}, \qquad (4.1)$$

where P is the number of excess holes in the z plane and is a function of z and t, α is the absorption coefficient of the light excitation source, G(t) is the external excitation flux, and R is reflection coefficient. The Fourier transformed expression for $\partial P/\partial t$ is $j\omega P'(\omega)$, where $P'(\omega)$ is related to P through the relation $P'(\omega) = \int_0^\infty P(t)\ e^{-\omega t}\ dt$. After performing the Fourier transformation on both sides of (4.1), we then have

$$D\partial^2 P'/\partial z^2 - (j\omega + 1/\tau)P' + G'(\omega)\ \alpha\ (1 - R)\ e^{-\alpha z} = 0, \qquad (4.2)$$

where P'and G' are the frequency domain counterparts of P and G, respectively, and $j = \sqrt{-1}$. For a simplicity the argument ω of P' is not explicitly shown in (4.2).

The boundary conditions in the frequency domain are

$$P'(\omega,\infty) = 0, \quad S\ P'(\omega,0) = D \frac{\partial P'(\omega,0)}{\partial z}, \qquad (4.3)$$

and the solution of (4.2) is

$$P'(\omega,z) = \frac{\alpha\ G'\ (1-R)}{D\ (\alpha^2 - L'^{-2})} \left[\frac{\Gamma + \alpha}{\Gamma + L'^{-1}}\ e^{-z/L'} - e^{-\alpha z} \right], \qquad (4.4)$$

where $L' = L/(1 + j\omega\tau)^{1/2}$, $L = \sqrt{D\tau}$, and $\Gamma = S/D$.

The luminescence signal I_{PL} observed outside the sample is calculated by using the distribution of the excess carrier density P′,

$$I_{PL}(\omega,\lambda) = \gamma(\lambda) \int_0^{\infty} \frac{P'(\omega,z)}{\tau_r} e^{-\beta(\lambda)z}\, dz, \qquad (4.5)$$

where τ_r is the radiative lifetime component of τ, $\beta(\lambda)$ is the absorption coefficient of the emitted light at wavelength λ, and $\gamma(\lambda)$ is the normalized PL spectrum defined as $\gamma(\lambda) = \gamma_{spon}(\lambda)/\int_0^{\infty} \gamma_{spon}(\lambda)\, d\lambda$. The $\gamma_{spon}(\lambda)$ is the spontaneous emission rate from the well-known van Roosbroeck-Shockley relation given as $\gamma_{spon}(\lambda) = (8\pi v^2 N^2 \alpha/c^2)/[\exp(h\nu/kT) - 1]$ [45]. The exponential term in (4.5) accounts for the self-absorption effect on the emitted PL signal and is important for the direct energy-gap materials, as will be shown in Section 4.3. Using (4.4), the integrated result is

$$I_{PL}(\omega) = K\, G'(\omega)\, F(\omega), \qquad (4.6)$$

where $K = \alpha\,(1 - R)\,\gamma(\lambda)/[\tau_r\, D\,(\alpha + \beta)]$,

and $$F(\omega) = \frac{(\alpha + \Gamma + \beta + L'^{-1})}{(\alpha + L'^{-1})(\beta + L'^{-1})(\Gamma + L'^{-1})}. \qquad (4.7)$$

With setting $\beta = 0$, $G'(\omega) = 1$, and $\gamma = 1$, after performing the inverse Fourier transform on (4.6), it is found that (4.6) converges to the time-domain expression (11) in Misiakos et al. [33], as was expected mathematically.

4.2.2 The Analysis

In (4.7), $F(\omega)$ is a function of S, τ, and D. Thus, $F(\omega)$ obtained from the PL measurements provides information that can be used for the

determination of these parameters. When the excitation pulse is of the delta shape, i.e. $G(t) = \delta(t)$, we have $G'(\omega) =$ constant, which implies $I_{PL}(\omega) \propto F(\omega)$. Therefore, due to the same dependence of $I_{PL}(\omega)$ and $F(\omega)$ on ω, $F(\omega)$ can be directly deduced from $I_{PL}(\omega)$. When the excitation is of finite pulse width, $F(\omega) = K^{-1} I_{PL}(\omega)/G'(\omega)$. To explore $F(\omega)$ further for the purpose of extracting the material parameters, we normalize $F(\omega)$ with respect to its zero frequency component $F(0)$, and obtain

$$F_{nor}(\omega) = F(\omega)/F(0) = I_{PL}(\omega)\, G'(0)/[I_{PL}(0)\, G'(\omega)], \qquad (4.8)$$

where $G'(0)$and $I_{PL}(0)$ are the zero frequency components of $G'(\omega)$ and $I_{PL}(\omega)$, respectively. Since $I_{PL}(\omega)$, $G'(0)$, $I_{PL}(0)$, and $G'(\omega)$ in (4.8) can be determined experimentally, using (4.7) and (4.8), by fitting the experimental $F_{nor}(\omega)$ to the theoretical $F_{nor}(\omega)$ for both the amplitude and phase components, the transport parameters can be extracted without a knowledge of K, which is experimentally hard to determine.

Expression (4.7) can be simplified for two different kinds of excitations. To simplify the analysis, we restrict the excitations to the case when the measured luminescence corresponds to the spectrum range where self-absorption is not significant ($\beta \approx 0$).

(i) Nearly uniform excitation ($\alpha \approx 0$)

For this case, we have $\beta \ll \Gamma$ and $\beta \ll L'^{-1}$, which leads (4.7) to

$$F(\omega) \approx L'^{2} = D\tau/(1 + j\omega\tau) = Amp_u(\omega)\, e^{j\phi(\omega)}, \qquad (4.9)$$

where $Amp_u(\omega)$ and $\phi(\omega)$ correspond to the amplitude and phase components of $F(\omega)$, respectively, and are given by

$$Amp_u(\omega) = D\tau/(1 + \omega^2\tau^2)^{1/2}, \qquad (4.10a)$$

$$\phi(\omega) = -\tan^{-1}(\omega\tau). \qquad (4.10b)$$

In (4.10a), the subscript u stands for the uniform excitation. The negative sign in (4.10b) physically represents the phase delay between the output and input signals at the excitation frequency ω. Taking log on both sides of (4.10a), we have

$$\log[\mathrm{Amp}_u(\omega)] = \log D + \log\tau - 1/2\,\log(1 + \omega^2\,\tau^2). \qquad (4.11)$$

When $\omega\tau << 1$, (4.11) can be simplified to $\log[\mathrm{Amp}_u(\omega)] = \log D + \log\tau$, which is independent of ω. When $\omega\tau >> 1$, (4.11) can be simplified to

$$\log[\mathrm{Amp}_u(\omega)] = \log D - \log\omega. \qquad (4.12)$$

Therefore, the $\mathrm{Amp}_u(\omega)$ versus ω plot in the log-log scale is frequency independent for $\omega\tau << 1$ and is a straight line with slope of -1 when $\omega\tau >> 1$. The intercept of this line with the ordinate at $\omega = 1$ equals logD. The corner frequency ω_c is, however, dependent only on τ. A typical plot for this analysis is shown in Figure 4.2. The curves are generated numerically using (4.7). We can see that changing D affects only the intercept with the ordinate and has negligible effect on ω_c and on the slope of the high-frequency range spectrum.

Regarding $F_{nor}(\omega)$, we have

$$F_{nor}(\omega) = 1/(1 + j\omega\tau) = \mathrm{Amp}'_u(\omega)\; e^{j\phi(\omega)}, \qquad (4.13)$$

where $\mathrm{Amp}'_u(\omega)$ corresponds to the amplitude component of $F_{nor}(\omega)$ given by

$$\mathrm{Amp}'_u(\omega) = 1/(1 + \omega^2\,\tau^2)^{1/2}. \qquad (4.14)$$

It is noted, that the phase component for both $F(\omega)$ and $F_{nor}(\omega)$ have the same expression as that given by (4.10b). From (4.14), when $\omega\tau >> 1$, the $\mathrm{Amp}'_u(\omega)$ against ω in the log-log scale plot is a straight line with the same slope as for the case of $F(\omega)$, but its intercept with the low frequency limit corresponds to the corner frequency ω_c (= $1/\tau$) that depends only on τ. Expression (4.10b) shows that the $\tan[-\phi(\omega)]$ versus

ω plot in the linear scale should yield a straight line with slope of τ. Figures 4.3(a) and 4.3(b) show typical plots generated by changing τ while fixing other parameters in (4.7). Since both $Amp'_u(\omega)$ and $\phi(\omega)$ are functions of τ only (independent of S), τ can be extracted without the knowledge on S from the normalized frequency spectrum. The extraction accuracy is not affected by the surface properties of the material, therefore, it provides a first determination of τ.

(ii) Strongly absorbed excitation ($\alpha \approx \infty$)

For this case, we have $\alpha >> \Gamma$, $\alpha >> \beta$, and $\beta << L^{-1}$, and (4.7) becomes

$$F(\omega) = Amp_s(\omega)\, e^{j\Theta(\omega)}, \tag{4.15}$$

where $$Amp_s(\omega) = B^{-1}\,(\Gamma^2 + 2\Gamma B\cos\phi + B^2)^{-1/2}, \tag{4.16a}$$

$$\Theta = \phi + \Omega,$$

$$\Omega = \tan^{-1}[B\sin\phi/(\Gamma + B\cos\phi)], \tag{4.16b}$$

and $$B = (1 + \omega^2\tau^2)^{1/4}/L. \tag{4.16c}$$

In (4.15), the subscript s stands for the strongly absorbed excitation. When $\omega\tau >> 1$, (4.16a) can be further simplified to

$$Amp_s(\omega) = \sqrt{D/\omega}\;\Gamma^{-1}\,[1 + \sqrt{2\omega/D}/\Gamma + \omega/(D\Gamma^2)]^{-1/2}, \tag{4.17}$$

which shows that in the high-frequency range, $Amp_s(\omega)$ is independent of τ. A typical plot of the dependence of $Amp_s(\omega)$ on ω at different τ generated from (4.7) for strongly absorbed excitation is shown in Figure 4.4. It is noted that Amp_s is weakly dependent on τ at $\omega_c \approx 1/\tau$ and is independent of τ at higher ω as was verified in (4.17). For a comparison, using (4.7), we also graphically analyze the sensitivity of

the dependence of $Amp_S(\omega)$ on S and D in the same scale plots shown in Figures. 4.5(a) and 4.5(b). A much stronger dependence of $Amp_S(\omega)$ on S and D is found in the high-frequency range in comparison with that on τ in Figure 4.4. It is interesting to point out the strong dependence on D in the high-frequency range analysis for this non-contact measurement. Note also, that the sensitivity to D is larger for the strongly absorbed case Figure 4.5(b) compared to the uniformly absorbed case (see 4.10(a)). Physically, this is because τ becomes relatively unimportant for $\omega > 1/\tau$, similarly to the short-circuit current case [6,46]. For the strongly absorbed excitation, the excess carriers are generated very near the surface, and the huge concentration gradient enhances the diffusion tendency of these carriers and, thus, enhances the dependence of $Amp_S(\omega)$ on D.

If we normalize $Amp_S(\omega)$ in (4.16a) with respect to its zero frequency component, when $\omega\tau >> 1$, we have

$$Amp'_S(\omega) = \frac{(\Gamma + 1/\sqrt{D\tau})}{\sqrt{\omega\tau}\,\Gamma\,(1 + \Gamma^{-1}\sqrt{2\omega/D} + \Gamma^{-2}\,\omega/D)^{1/2}}, \qquad (4.18)$$

where $Amp'_S(\omega)$ is the amplitude of the $F_{nor}(\omega)$ for the strongly absorbed excitation. Expression (4.18) is a function of both S and τ. To investigate the sensitivity of $Amp'_S(\omega)$ on τ and S, we plot $Amp'_S(\omega)$ from (4.18) against ω in log-log scale by changing different parameters. Figure 4.6 illustrates the effects of τ on $Amp'_S(\omega)$ for the strongly absorbed excitation. Changing τ affects only the corner frequency and has no effect on the slope of the high-frequency spectrum. Figure 4.7 illustrates the effects of S on $Amp'_S(\omega)$. Changing S only weakly affects the corner frequency, but strongly affects the slope of the high-frequency spectrum. This suggests that τ and S can be determined

independently from different parts of the curve in the frequency spectrum. Therefore, the two parameters can be separated. Moreover, the nearly uniform absorption experiment provides an even more accurate determination of τ and serves to double check the results.

4.3 Photoluminescence Measurements of S and τ

4.3.1 Experimental Setup and Measurements

Figure 4.8 shows the experimental setup used for the measurement. A nitrogen-pumped dye laser with 800-ps half pulse width was used as the excitation source. The laser beam was focused into a 0.4 mm x 5 mm^2 spot to strike the front surface of the wafer via a cylindrical lens. The luminescence light emitted from the front side was collected using an objective lens. The collected PL signal was focused into a 3 x 3 mm^2 spot and then directed into a double grating monochromator (bandwith = 0.5 nm) for spectral separation. A high-pass filter was put in front of the entrance slit of the monochromator to reject the scattered laser light and pass the PL light. The PL signal of the selected wavelength was detected with a Si avalanche photodiode (APD) having a rise time of 0.2 ns. The applied reverse bias V_R on the APD is 150 V, which yields an amplification of about 100. The APD was mounted on a XYZ micropositioner to get the maximum output signal. The PL signal is measured through Tektronix 7D20 or 11402 digitizer and is transferred to a VAX minicomputer through IBM PC for the frequency-domain analysis.

The luminescence signal measured by the digitizer is the total response from the PL signal and from the system. In order to obtain the frequency response of the PL signal accurately, the effects due to the finite laser pulse width and the finite bandwidth of the detector and digitizer have to be accounted for. In the frequency domain, $I_{PL}(\omega)$ can be recovered from the measured total response $I_{tot}(\omega)$ through the following relation

$$I_{PL}(\omega) = I_{tot}(\omega)/I_{sys}(\omega), \qquad (4.19)$$

where $I_{sys}(\omega)$ is the Fourier transform of the measurement system. To measure $I_{sys}(\omega)$, we directly strike the APD with the laser light pulse and then do the Fourier transform of the measured response. Since both $I_{tot}(\omega)$ and $I_{sys}(\omega)$ are measured with the APD under the same reverse bias, the influence of the parasitic RC time constant, due to the p/n junction capacitance C_j of the detector and the series combination of the load resistance R_L (50 Ω) and the detector series resistance R_s, is cancelled after the normalization in (4.19). The phase delay plot is very sensitive to the signal delay, both to the light travelling delay and electrical delay. The delays of $I_{tot}(t)$ and $I_{sys}(t)$ were suitably accounted for in the analysis. This correction is not very important for the lifetime measured here, but is important for sub-nanosecond lifetime measurements (see Section 2.3.2). The resulting frequency-domain spectrum of the PL signal is then fitted to the theoretically predicted spectrum for different excitations for parameter extraction.

From the above discussion, it becomes obvious that working in the frequency domain makes the inclusion of the effects due to the finite system response straightforward. This is to be contrasted with the

elaborated deconvolution required for the time domain analysis, as pointed out in Section 4.1.

4.3.2 Experimental Results

Measurements were done on Si-doped n-type GaAs wafer with doping density of $N_{DD} = 2 \times 10^{17}$ cm^{-3} chemically passivated by sulfide-based layer. The passivation was done about two months before the measurements were performed. The measured PL signals for the nearly uniform and strongly absorbed excitation experiments are shown in Figure 4.9. All the curves have been suitably normalized so that they can be shown together in the same semi-logarithmic plot. All decays become essentially straight lines after the first 20 ns, illustrating the nearly exponential decay behavior of the PL signal. Curve (a) is used for the uniformly absorbed excitation analysis. Curves (b) and (c) are used for the strongly absorbed excitation analysis. The different slope of the curves (b) and (c) is due to the self-absorption of the emitted light at different wavelengths. The relatively noisy signal of all curves is unavoidable whenever the signal is very weak, which causes difficulties in the parameter extraction from the time-domain analysis. The noise is due partly to the high 1 GHz bandwith of the measurement system and can be reduced by filtering out the high-frequency portion of the noise, beyond the range required for the analysis for the material parameters. As shown later, this is automatically done by the frequency-domain analysis.

For the uniform excitation, the dye laser was tuned to $\lambda = 880$ nm, which corresponds to the absorption coefficient $\alpha = 1000$ cm^{-1} [47].

The PL signal with wavelength of λ = 860 nm, which corresponds to the self-absorption coefficient β = 4200 cm^{-1} [47], was chosen for the analysis by tuning the monochromator. Figures 4.10(a)-(c) correspond to the Fourier transformed signal responses for the nearly uniform excitation. The dotted lines are numerically generated using the theoretical expression (4.7), and the solid lines are the Fourier transformed responses from the curve (a) in Figure 4.9. The theoretical fits are generated by fixing S = 7000 cm/s, a value obtained from the strongly absorbed excitation (Figure 4.11), and changing τ with increment of 10 ns. Here, the minority hole diffusivity is assumed equal to that of the majority holes. In Figures 4.10(a)-(c), we intentionally plot the abscissa axis in the linear scale to increase the resolution in the parameter extraction procedure. It is interesting to point out that the $\tan(-\theta)$ versus $f^{1/2}$ plot in Figure 4.10(c) has higher sensitivity to τ than the other two dependencies in Figures 4.10(a) & (b). From the analysis for this experiment in Sec. 4.2, the response is insensitive to the value of S. Therefore, based on the plots in Figures 4.10(a)-(c), after comparing the experimental results with the theoretical fits, the extracted lifetime, which is sensitive only to the corner frequency, is τ = 56 ns.

Curves (b) and (c) in Figure 4.9 show the typical PL signal responses for the strongly absorbed excitation. The dye laser was tuned to 505 nm wavelength, which corresponds to $\alpha = 8 \times 10^4$ cm^{-1} [47]. The measured emitted signals with wavelengths λ = 900 nm and λ = 876 nm are shown in Figure 4.9 as curves (b) and (c), respectively. The signal corresponding to λ = 876 nm was measured after changing the

laser striking point at the wafer for checking the spatial uniformity of both τ and S. Due to the stronger self-absorption effect, curve (c) shows a steeper decay. Thus, the slope of the time-domain decay signal yields a shorter effective lifetime than that from the curve (b). Figures 4.11(a)-(c) correspond to the Fourier transformed responses for the strongly absorbed excitation. The solid line is the Fourier transformed response from the curve (c) in Figure 4.9, and the dotted lines are the theoretically predicted results. In all these plots, the theoretical fits are obtained with fixing τ = 56 ns and changing S with increment of 2000 cm/s. The extracted surface recombination velocity is S = 7000 $\pm$ 1000 cm/s with a deviation of about 14% for the fitted results. As pointed out in Sec. II.B, for the strongly absorbed excitation, τ is sensitive only to the corner frequency, while S is more sensitive to the slope of the response. Hence, τ extracted from this measurement provides a cross check of the accuracy for τ obtained from the nearly uniform excitation measurement. In addition, the extracted parameters from the amplitude and from the phase plots provide a double check for the accuracy.

We have investigated the spatial uniformity of τ and S by doing the similar analysis for the signal shown by the curve (b) in Figure 4.9, which was measured at the nonabsorbing wavelength (λ = 900 nm) after changing the laser striking point. Figures 4.12(a) & (b) show the Fourier analysis for this signal. The extracted value for S from the best fit is S = 12000 $\pm$ 1000 cm/s for τ = 56 ns. Although, the decay slopes of the curves (b) and (c) in Figure 4.9 are different, yielding different effective lifetimes from the two time-domain curves, the frequency-domain analysis gives the real bulk lifetime with the

same value of τ = 56 ns. This clearly illustrates that the real τ can be obtained from the FDPL at any emission wavelength. The difference in the extracted S indicates nonuniform surface passivation. This could be due to the nonuniform thickness of the chemical film, which could result in different degree of degradation for the passivated surface [48]. Detail study of the surface passivation for GaAs and other materials by FDPL is left for future study.

4.3.3 Application to Heavily Doped Si and InP

We have also extended the FDPL technique to extract S and τ from InP and heavily doped Si. For a comparison with the results from FDPL analysis, the time-domain PL signals are referred from the literature data for Si [12,49] and for InP [50], respectively.

Figure 4.13 shows the PL signal referred from Swirhun [49] (curve (a)) and from Dziewior and Schmid [12] (curve (b)). Curve (a) corresponds to the doping density N_{DD} = 4.2 x 10^{18} cm^{-3} and was measured on a Si wafer well passivated by SiO_2 [49]. The excitation wavelength used is λ = 647 nm, for which α = 4000 cm^{-1} [51]. Curve (b) corresponds to the doping density N_{DD} = 9.7 x 10^{18} cm^{-3} and was measured on etched bare silicon wafer [12]. The excitation wavelength is λ = 514.5 nm, with corresponding α = 1.3 x 10^{4} cm^{-1} [51]. Due to the different surface preparations, it is expected that S extracted from (a) will be much smaller than that from (b). Figures 4.14(a) and (b) and 4.15(a) and (b) illustrate the results after performing the frequency-domain analysis on the signals from curves (a) and (b) in Figure 4.13, respectively. Due to the negligible self-absorption

effect on the emitted light for Si, the self-absorption coefficient β is set to zero. In the analysis of Figure 4.14, the minority hole diffusivity D_p is set to 4.4 cm^2/s, a value interpolated from the results in Wang et al. [6], and the extracted S from the best fit is S = 1100 cm/s, which is comparable to the effective surface recombination velocity measured using the vertical gated transistor [49]. The extracted lifetime is τ = 165 ns, which is 5 ns greater than that reported in [49]. For the analysis in Figure 4.15, the minority hole diffusivity D_p = 4 cm^2/s is from Wang et al. [6]. The best fit from Figures 4.15(a) and (b) shows that S = 30000 cm/s for the unpassivated Si surface, a value much larger than that from Figure 4.14, as was expected earlier. The lifetime extracted is τ = 57 ns, which is 8 ns greater than that extracted from the time-domain analysis [12]. It is noted that if we do the correction for the lifetimes for both dopings, the τ vs N_{DD} plot [12] would show a stronger Auger recombination dependence, and the data point for $N_{DD} = 4.2 \times 10^{18}$ cm^{-3} almost sits on the $1/N_{DD}^2$ line. This illustrates the physical implication of the correction for τ using the FDPL.

Figure 4.16 shows the PL signals for InP referred from Ahrenkiel et al. [50]. This figure is shown as an illustration convenience, more detailed information about the curves can be referred from Ahrenkiel et al. [50]. The different slopes of the decay curves, which indicate different effective lifetimes, are due to a different degree of the self-absorption on the emitted light. This is a result of a large absorption coefficient for direct energy-gap materials, as was similarly shown in Figure 4.9 for GaAs. Figures 4.17 and 4.18 correspond to the frequency-domain analysis for the signals (a) and (b)

in Figure 4.16, respectively. We can see, that with choosing a suitable value for β, which accounts for the self-absorption effect for both signals, the resulting real bulk lifetime τ from these two signals is the same. The lifetime thus obtained is τ = 280 ns and is close to the value (τ = 300 ns) reported in Ahrenkiel et al. [50].

4.4 Comparison Between the Time-Domain and Frequency-Domain Analyses

The analytical expression accounting for the self-absorption on the PL decay in the time domain $I_{PL}(t)$ is essential for the time-domain analysis. The closed-form expression for $I_{PL}(t)$ has been derived previously by us, and is shown here for a convenience only. The detailed description about the derivation and application for $I_{PL}(t)$ is given in Chapter 5. The time-domain PL decay signal is given by

$$I_{PL}(t) = Q\,(\Gamma + \alpha)/(\Gamma - \beta)\,\{[\alpha/(\alpha^2 - \beta^2) - \alpha/(\alpha^2 - \Gamma^2)]\,FX(\alpha^2 Dt) + [\Gamma/(\alpha^2 - \Gamma^2)]\,FX(S^2 t/D) - [\beta/(\alpha^2 - \beta^2)]\,FX(\beta^2 Dt)\}\,\exp(-t/\tau), \qquad (4.20)$$

where $FX(X) = \exp(X)\,\mathrm{erfc}(\sqrt{X})$, $Q = G\,(1 - R)\,\alpha$, and $\Gamma = S/D$. Here, all the symbols have the usual meaning.

Figure 4.19(a) shows the normalized time domain PL decay $I_{PL}(t)$ measured using the same setup as in Figure 4.8. Because of the non-exponential decay, the experimental points cannot be fitted with a single exponential decay curve, which is a straight line for I_{PL} in semi-log scale plots. We therefore fit the experimental results with the theoretical curves generated via the analytical expression (4.20)

for $I_{PL}(t)$. In the measurement of $I_{PL}(t)$, the excitation light source was tuned to the wavelength of λ = 735 nm ($\alpha \approx 10^4$ cm^{-1}). The luminescence very near the peak in the PL spectrum was measured to provide stronger response, and hence to minimize the disturbance due to the high-frequency noise. This is because the noise seriously affects the accuracy of the parameters extracted from the time-domain analysis. The wavelength of the measured signal is λ = 867 nm, and the self-absorption coefficient for this wavelength is $\beta \approx 3000$ cm^{-1}. These values for α and β were used in generating the theoretical curves for the fitting. The fits were obtained by fixing τ = 56 ns while changing S from 3000 cm/s to 15000 cm/s with increment of 3000 cm/s. In the fitting procedure, both the theoretical and experimental decay signals were normalized with respect to their peak values. In the normalization of the experimental data, the laser signal was treated as a delta-like pulse. Therefore, the effect due to finite laser pulse width is neglected. The best-fitted curve shows the extracted surface recombination velocity to be S = 9000 $\pm$ 3000 cm/s. Note the large uncertainty (~ 33 %) for S extracted from this analysis. The uncertainty is due to the high-frequency noise, which is hard to remove even when the signals are measured at the peak wavelength in the luminescence spectrum. Here, we try not to use the electrical filtering, although the frequency filter can reduce the high-frequency noise to a certain degree. This is because the filtering distorts the PL response and introduces additional uncertainty to our analysis. In addition, filtering reduces the time response of the system which limits the value of the smallest lifetime that can be accurately measured.

In the time-domain analysis, the normalized experimental data are fitted with the normalized theoretical dependencies. The normalization is done with respect to the peak intensity [39]. An accurate determination of the peak intensity from PL signals is, thus, critical for the time-domain analysis. However, we have noted that the determination of the peak intensity is subjective and difficult because of the fluctuation of the laser output and the electrical noise. Therefore, the uncertainty in the peak intensity could also introduce additional uncertainty for the extracted parameters, and yields the overall uncertainty for the measured S greater than 33 %.

The FDPL analyzes the luminescence signal in the frequency domain. The normalization is done by normalizing the frequency response to its zero-frequency component. By Fourier transform, the zero-frequency component $I_{PL}(\omega=0)$ is equal to the integrated area under the measured time-domain signal $I_{PL}(t)$ shown in Figure 4.19(b), $I_{PL}(\omega=0) = \int_0^\infty I_{PL}(t)$ dt. Because of the integration, the area under $I_{PL}(t)$ and, thus, the normalization in the frequency domain is much less affected by the uncertainty in the peak intensity and noise. For the analysis, we Fourier-transformed the entire PL decay curve into the frequency space. Therefore, the zero-frequency component does not disregard any data points in the PL signals, and makes the normalization less subjective than that in the time-domain analysis. Note, that the signal analyzed in Figure 4.11 is measured at the wavelength (λ = 876 nm) corresponding to a much weaker luminescence intensity than that (λ = 867 nm) in Figure 4.19. Nevertheless, the accuracy of the parameters extracted from FDPL (deviation ~ 14%) is still better than that from the time domain analysis (deviation $\geq$ 33%, see Figure 4.19(a)). This quantitative comparison clearly illustrates the advantages of the FDPL.

4.5 Conclusions

We have successfully demonstrated a new FDPL (Frequency-Domain Photoluminescence) technique for lifetime measurement and for surface characterization in both direct and indirect energy-gap materials. To our knowledge, this is the first nondestructive technique that allows the separate determination of the minority-carrier lifetime and surface recombination velocity from the same measurement. A separate measurement with uniformly absorbed excitation allows the determination of lifetime independently and provides an accuracy check of the lifetime. Due to its noncontact and nondestructive properties, the technique is applicable especially for the characterization of surface passivation on III-V compound materials and for wafer screening. The extension of this technique for the determination of minority carrier diffusivity in MOCVD and MBE grown layers is planned.

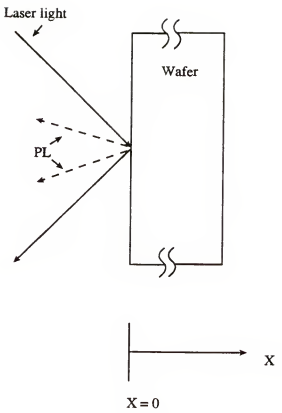

Fig. 4.1. Schematic illustration of an infinite semiconductor sample excited by a laser beam.

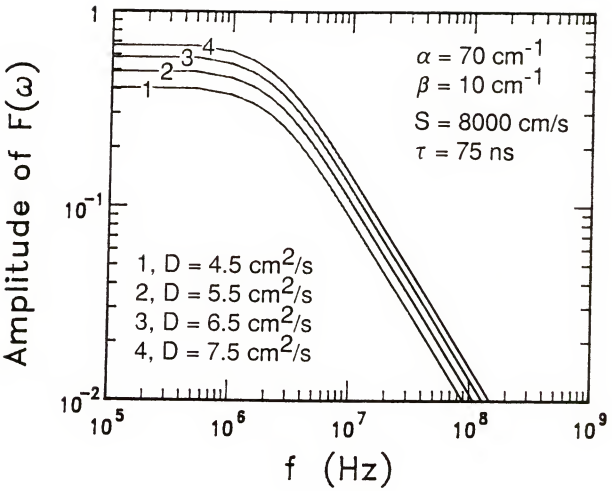

Fig. 4.2. Theoretical analysis of the frequency response for the nearly uniform excitation. Here α is set to 70 cm^{-1}. The frequency f is plotted against the amplitude of Eq. (4.7). The plots are obtained by fixing α, β, S, and τ, while changing D.

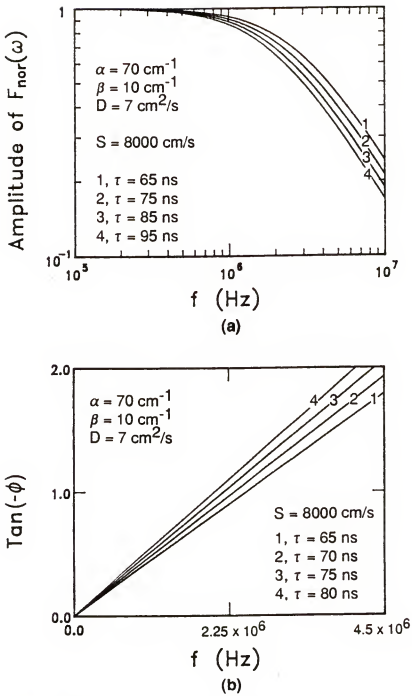

Fig. 4.3. Theoretical analysis of the frequency response for the nearly uniform excitation. The frequency f is plotted against the normalized amplitude F_{nor} (a) and tan(- phase) (b). The F_{nor} is obtained by normalizing Eq. (4.7) with respect to its zero frequency response. The plots are obtained by fixing α, β, S, and D, but changing τ.

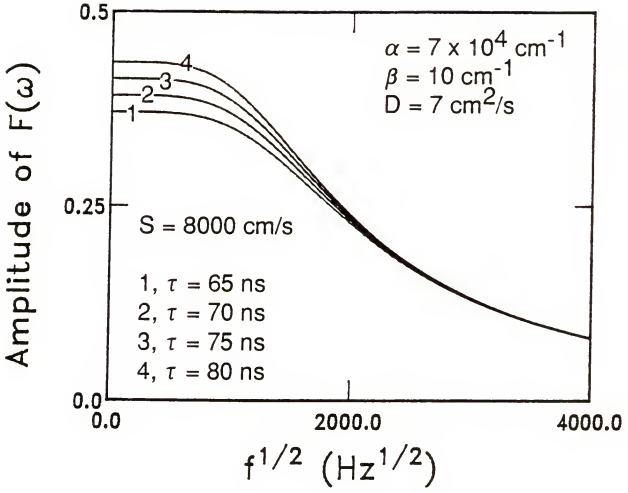

Fig. 4.4. Theoretical analysis of the frequency response for the strongly absorbed excitation. Here α is 7×10^4 cm^{-1}. The square root of frequency $f^{1/2}$ is plotted against the amplitude of $F(\omega)$. The plots are obtained by fixing α, β, S, and D, but changing τ.

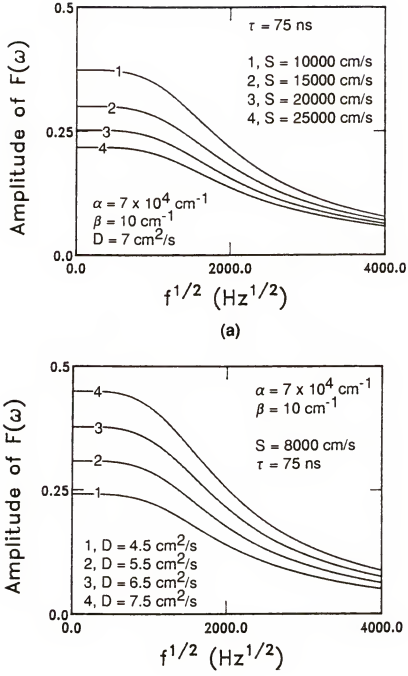

Fig. 4.5. Theoretical analysis of the frequency response for the strongly absorbed excitation. The plots are obtained by changing S (a) or by changing D (b), while fixing the rest of the parameters.

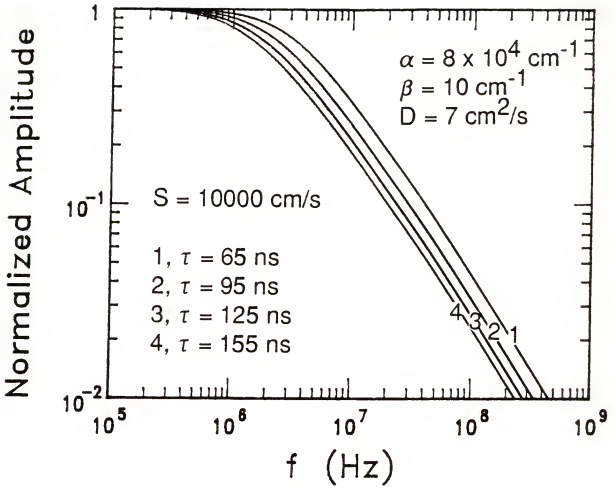

Fig. 4.6. Theoretical analysis of the normalized frequency response for the strongly absorbed excitation. Here α is 8 x 10^4 cm^{-1}. The plots are obtained by changing τ and fixing other parameters.

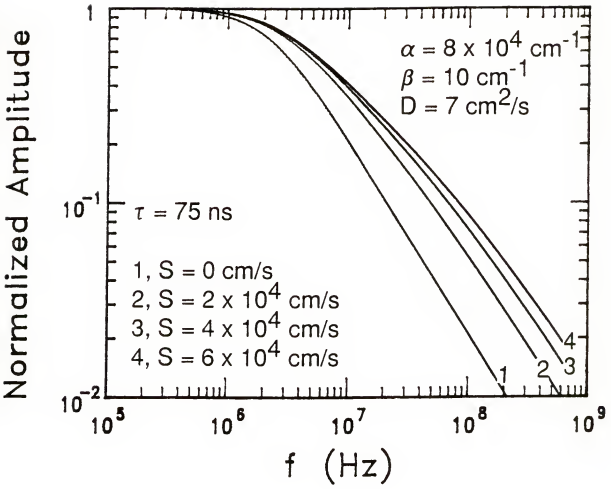

Fig. 4.7. Theoretical analysis of the normalized frequency response for the strongly absorbed excitation. Here α is 8×10^4 cm^{-1}. The plots are obtained by changing S and fixing other parameters.

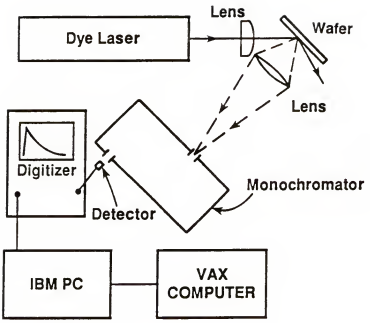

Fig. 4.8. Experimental setup for the photoluminescence measurement and the analysis.

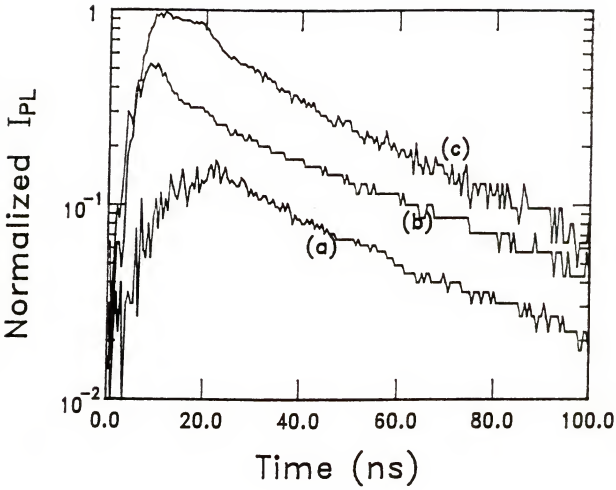

Fig. 4.9. Time-domain PL decay signals measured under different excitations. The laser wavelengths used are λ = 880 nm (curve a) and λ = 505 nm (curves b and c). The emission wavelengths are λ = 860 nm (curve a), 900 nm (curve b), and 876 nm (curve c).

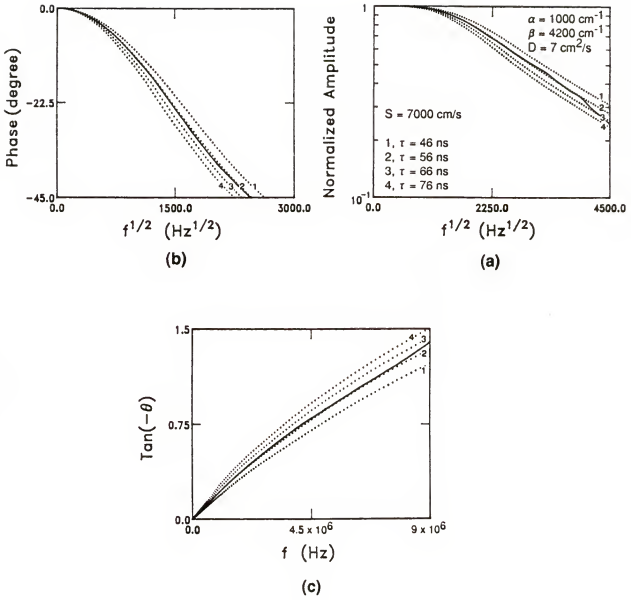

Fig. 4.10. Theoretical (dotted lines) and experimental (solid line) frequency responses for the nearly uniform excitation. Both amplitude (a) and phase (b) and (c) plots are normalized with respect to the zero frequency response. The theoretical plots are obtained by changing τ and fixing other parameters.

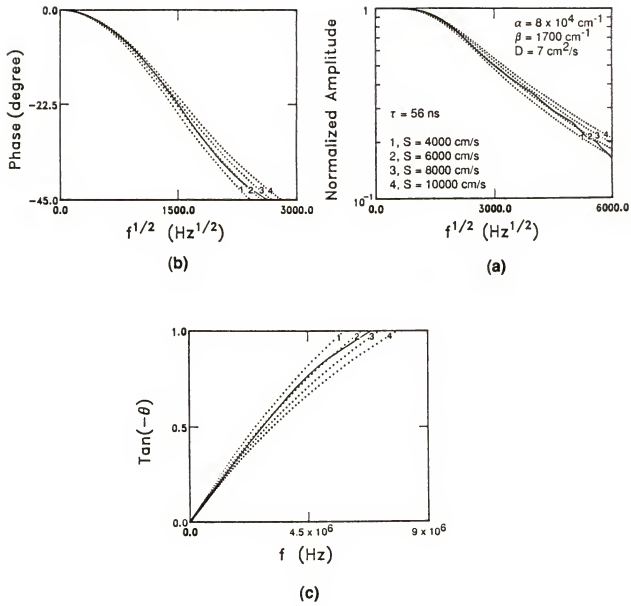

Fig. 4.11. Theoretical (dotted lines) and experimental (solid line) frequency response for the strongly absorbed excitation. The emission wavelength is λ = 876 nm. Both amplitude (a) and phase (b) and (c) plots are normalized with respect to the zero frequency response. The theoretical plots are obtained by changing S and fixing other parameters.

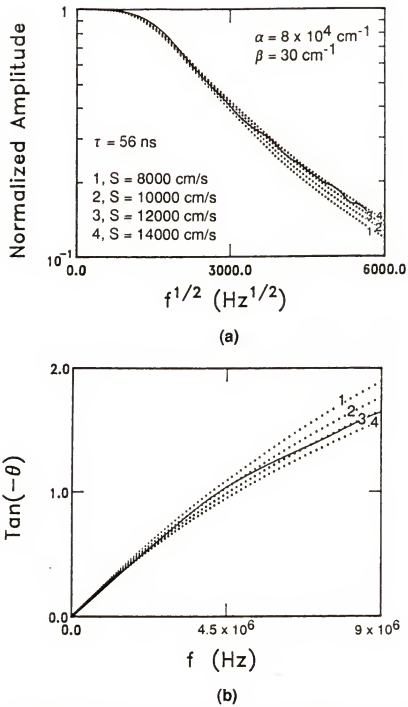

Fig. 4.12. Theoretical (dotted lines) and experimental (solid line) frequency response for the strongly absorbed excitation. The emission wavelength is λ = 900 nm. Both amplitude (a) and phase (b) plots are normalized with respect to the zero frequency response. The theoretical plots are obtained by changing S and fixing other parameters.

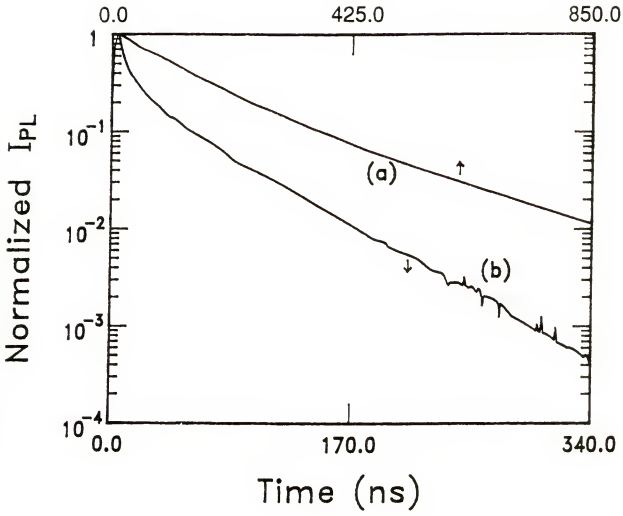

Fig. 4.13. Time domain PL decay signals for silicon wafers with different surface passivations (from Refs. 12 and 49).

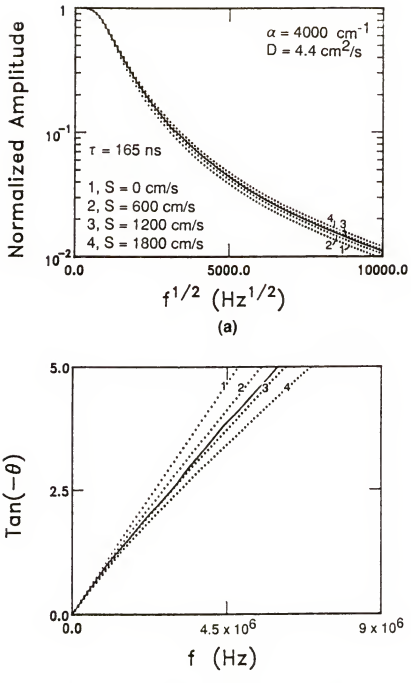

Fig. 4.14. Theoretical (dotted lines) and experimental (solid line) frequency response for the strongly absorbed excitation. The laser wavelength is λ = 647 nm. Both amplitude (a) and phase (b) plots are normalized with respect to the zero frequency response. The theoretical plots are obtained by changing S with increment of 600 cm/s while fixing τ = 165 ns and other parameters.

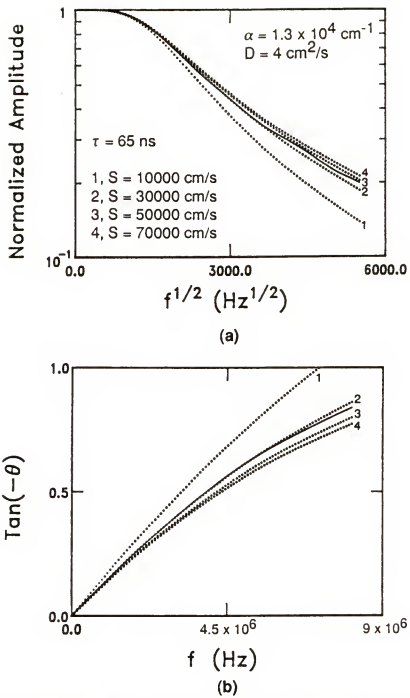

Fig. 4.15. Theoretical (dotted lines) and experimental (solid line) frequency response for the strongly absorbed excitation. The laser wavelength is λ = 514.5 nm. Both amplitude (a) and phase (b) plots are normalized with respect to the zero frequency response. The theoretical plots are obtained by changing S with increment of 20000 cm/s while fixing τ = 65 ns and other parameters.

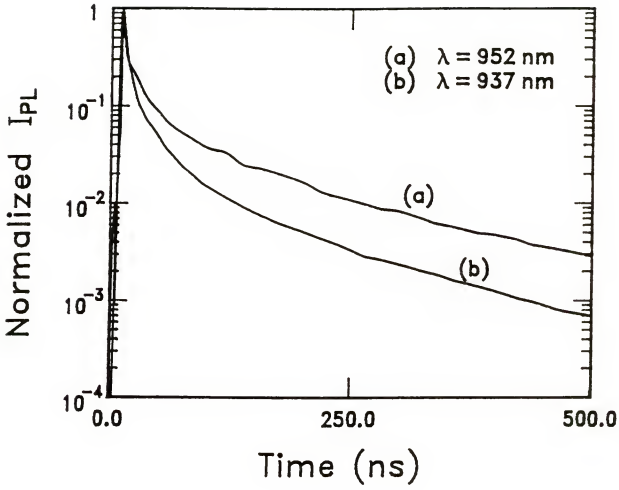

Fig. 4.16. Time-domain PL decay signals for InP wafer (from Ref. 50). The signals come from two different emission wavelengths as indicated.

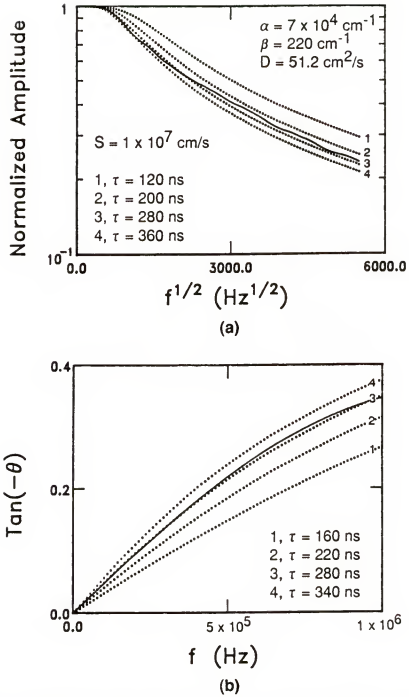

Fig. 4.17. Theoretical (dotted lines) and experimental (solid line) frequency response for the strongly absorbed excitation. The emission wavelength is λ = 952 nm. Both amplitude (a) and phase (b) plots are normalized with respect to the zero frequency response. The theoretical plots are obtained by changing τ with increment of 80 ns (a) and 60 ns (b) while fixing S = 1 x 10^7 cm/s ($\simeq$ thermal velocity) and other parameters.

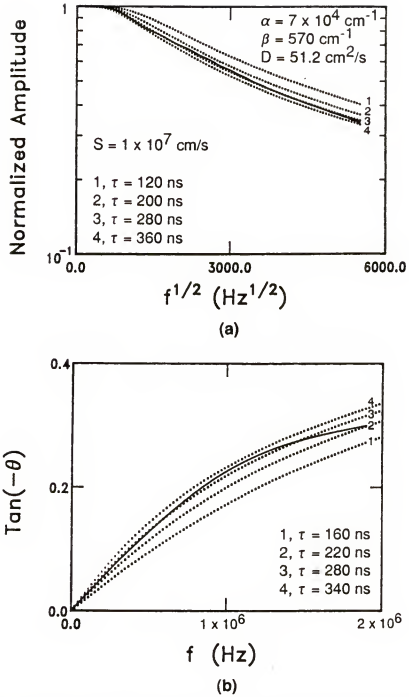

Fig. 4.18. Theoretical (dotted lines) and experimental (solid line) frequency response for the strongly absorbed excitation. The emission wavelength is λ = 937 nm. Both amplitude (a) and phase (b) plots are normalized with respect to the zero frequency response. The theoretical plots are obtained by changing τ with increment of 80 ns (a) and 60 ns (b) while fixing S = 1 x 10^7 cm/s (≃ thermal velocity) and other parameters.

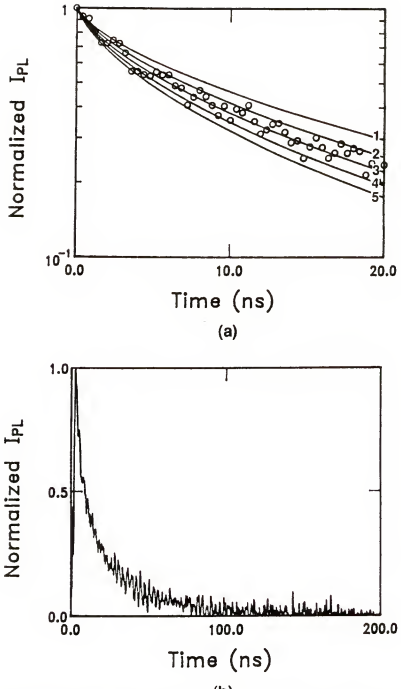

Fig. 4.19.(a) Time-domain analysis showing curve fitting for the photoluminescence decay signal. The solid lines are theoretical curves calculated using (4.20). The open circles are from the experiment. The solid curves corresponds to S = 3000 cm/s (curve 1), S = 6000 cm/s (curve 2), S = 9000 cm/s (curve 3), S = 12000 cm/s (curve 4), and S = 15000 cm/s (curve 5).
(b) Measured time-domain signal in linear scales.

CHAPTER 5
NONDESTRUCTIVE MEASUREMENT OF MINORITY-CARRIER LIFETIME AND SURFACE/INTERFACE RECOMBINATION VELOCITY IN COMPOUND SEMICONDUCTORS

5.1 Introduction

The minority carrier lifetime τ and the surface/interface recombination velocity S in compound semiconductors are of primary interest for the design and fabrication of solar cells and other optoelectronic devices. The knowledge of S is also very important for studying surface passivation, and for developing new passivation processes. Typically, the surface properties due to the passivation are studied by a qualitative comparison of measurements from the device with a passivated surface with those from a reference device. Measurement of the barrier height of a Schottky diode [52] and the surface potential of a MESFET [53] have been used to characterize the surface passivation, and have provided valuable results. These techniques are, however, destructive and are not suitable for monitoring the fabrication process. Nondestructive techniques, in particular the DC and transient photoluminescence (PL) measurements have also been widely used. In the DC PL experiment, the PL intensity is measured from the passivated sample excited by a CW laser and is compared with the PL intensity from a reference sample. The reference sample can be either an unpassivated surface with a large S, or a heterointerface with a very small S. Thus, the DC PL measurement

yields only qualitative results. The transient PL monitors the excess carrier recombination by observing the transient luminescence signal from radiative recombination after the laser excitation is terminated. This measurement yields quantitative results. However, in order to separate the surface recombination from the bulk recombination, a well passivated reference sample is required [38].

The PL measurements are complicated by the self-absorption effects on the emitted photons, which are important for semiconductors with very large absorption coefficient α. From the well known van Roosbroeck-Shockley relation [45], a material with a short radiative lifetime τ_r has a large α. Thus, the self-absorption is closely related to the materials with a short τ_r and, hence, to the direct energy band materials.

In this chapter, a new optical method is presented for measurement of the bulk lifetime τ and surface recombination velocity S in semiconductors. The method is based on measurement of the photoluminescence decay as a function of the self-absorption under different excitation conditions. The method allows a quantitative surface characterization without a reference sample. In Section 5.2, the closed-form analytical expressions, accounting for the self-absorption, are derived for the photoluminescence decay for a semi-infinite sample with an arbitrary value of S. In Section 5.2.2, a comprehensive method based on this expression is presented for the nondestructive extraction of the parameters from the bulk wafer. The experimental results with GaAs wafer as an illustration are shown in Section 5.3. The technique presented here is particularly suitable for

characterization of the surface passivation of compound semiconductors with direct energy-gap, and is demonstrated on a GaAs sample. In addition, a methodology for extracting τ and S from materials with a negligible self-absorption is presented. This can be useful for characterization of indirect energy-gap materials, such as Si.

5.2 Theoretical analysis

Misiakos et al. [33], have derived analytical expressions for the PL decay for the case of a finite interface recombination velocity and a semi-infinite slab thickness. They also showed that the beam size, shape, and uniformity does not affect the PL decay rate. Other workers, using different approaches, have derived similar expressions for the purpose of investigation of the influence of the surface recombination on measurement of τ in Si [31,32,34]. The expressions given are, however, limited to the materials without self-absorption [31,32,34]. Recently, Ahrenkiel et al. [50], derived an analytical expression to model the PL decay for a window/absorber heterojunctions, for the case of an infinite S and a semi-infinite slab thickness with accounting for the self-absorption. Therefore, a PL decay model that accounts for the self-absorption and for a finite S is not yet available. Below, an analytical treatment for the PL decay for an arbitrary S and a semi-infinite slab is presented. The analytical model accounts for the self-absorption. Based on the analytical expressions, the methodology to extract S and τ is devised.

5.2.1 Modeling the Photoluminescence Decay

Consider a semi-infinitely thick semiconductor sample with the z axis perpendicular and with the x and y axes parallel to the sample surface. We assume that that the sample is a uniformly doped n-type material, the extension to p-type is straightforward. Throughout the analysis, low-level injection condition is assumed, therefore, the minority carriers flow by diffusion and the minority carrier bulk lifetime is characterized by a constant value τ. We also assume that the surface at $z = 0$ is irradiated by a defocused laser beam that is terminated at time $t = 0$. It has been shown by Misiakos et al. [33], that the three-dimensional continuity equation for the excess hole concentration Δp can be simplified mathematically to a one-dimensional equation, provided that the transport parameters are independent of the injection level and are functions of z only. Employing this conclusion, at $t > 0$, the time dependent continuity equation is [33]

$$\frac{\partial P}{\partial t} = D \frac{\partial^2 P}{\partial z^2} - \frac{P}{\tau}, \tag{5.1}$$

where D is the hole diffusivity, and P is the total number of the excess holes per unit of depth in the x-y plane given by $P = \int_{-\infty}^{\infty}\int_{-\infty}^{\infty} \Delta p \, dx \, dy$. By letting

$$P(z,t) = P'(z,t)\, e^{-t/\tau}, \tag{5.2}$$

we can rewrite Eq. (5.1) as

$$\frac{\partial P'}{\partial t} = D \frac{\partial^2 P'}{\partial z^2}. \tag{5.3}$$

This equation can be solved by the method of the Laplace transform.

Taking the Laplace transform on both sides of Eq. (5.3) yields

$$s\,\underline{P}'(z,s) - P'(z,0) = D\,\frac{\partial^2 \underline{P}'(z,s)}{\partial z^2}, \tag{5.4}$$

where s is the Laplace transform operator and $\underline{P}'$ is the Laplace transformation of P'. The initial condition for Eq. (5.4) is

$$P'(z,0) = Q\,e^{-\alpha z}, \tag{5.5a}$$

where $Q = \alpha\,G\,(1 - R)$, $G = \int_{-\infty}^{\infty}\int_{-\infty}^{\infty} g(x,y)\,dx\,dy$ is the total photon flux projected on the sample surface, g(x,y) is the photon flux for a delta impulse laser excitation projected at a point (x,y), and R is the reflection coefficient. The boundary conditions are

$$S\,\underline{P}'(0,s) = D\,\left.\frac{\partial \underline{P}'(z,s)}{\partial z}\right|_{z\,=\,0}, \text{ and} \tag{5.5b}$$

$$\underline{P}'(\infty,s) = 0. \tag{5.5c}$$

Using Eqs. (5.5a), (5.5b), and (5.5c), Eq.(5.4) has the solution

$$\underline{P}'(z,s) = -\frac{Q}{\sqrt{D}}\,(S + \alpha D)\,\frac{\exp(-s\sqrt{s/D}\,z)}{(s - \alpha^2 D)(\sqrt{s} + S/\sqrt{D})}$$

$$+ Q\,\exp(-\alpha z)\,/\,(s - \alpha^2 D). \tag{5.6}$$

The out-flux of the emitted photons comes from the photons reaching the surface and escaping from the active region, and can be approximated using a one-dimensional model for a widely defocused laser beam. Using this approximation, we calculate the attenuation along the z axis for the luminescence from the carriers that recombine at $z = z'$ plane. The attenuation is characterized by the self-absorption coefficient β, and the PL decay signal $I_{PL}(t)$, which is propotional to the integrated excess hole density, is thus equal to

$$I_{PL}(t) = C\,e^{-t/\tau}\,L^{-1}\,[\int_0^{\infty} \underline{P}'(z',s)\,e^{-\beta z'}\,dz'], \tag{5.7}$$

where C is a proportional constant, and L^{-1} is the inverse Laplace transform. After some algebra to evaluate the integral in (5.7), we obtain

$$\int_0^\infty \underline{P}'(z',s)\, e^{-\beta z'}\, dz'$$

$$= -\frac{QD\,(S/D + \alpha)}{(S/\sqrt{D} + \sqrt{s})(s - \alpha^2 D)(\sqrt{s} + \beta/\sqrt{D})} + \frac{Q}{(s - \alpha^2 D)(\alpha + \beta)}. \quad (5.8)$$

Taking the inverse Laplace transform on (5.8), we transform the solution to the time domain, and the final expression for (5.7) is

$$I_{PL}(t) = Q\,(\Gamma + \alpha)/(\Gamma - \beta)\,\{[\alpha/(\alpha^2 - \beta^2) - \alpha/(\alpha^2 - \Gamma^2)]$$
$$FX(\alpha^2 Dt) + [\Gamma/(\alpha^2 - \Gamma^2)]\, FX(S^2 t/D) - [\beta/(\alpha^2 - \beta^2)]$$
$$FX(\beta^2 Dt)\}\, \exp(-t/\tau), \quad (5.9)$$

where $FX(X) = \exp(X)\, \mathrm{erfc}(\sqrt{X})$, $Q = G\,(1 - R)\,\alpha$, and $\Gamma = S/D$.

When setting $\beta = 0$, Eq. (5.9) converges to Eq. (11) in [33], which corresponds to the case without self-absorption. Similarly, by setting $S = \infty$, Eq. (5.9) converges to Eq. (24) in Ahrenkiel et al. [50], which applies for the window/absorber layer or for a sample with poorly passivated surface.

To illustrate the effect of the self-absorption on the PL decay signal, we present the normalized $I_{PL}(t)$ versus t plot in Figure 5.1. The plot is in a semi-log scale, and $I_{PL}(t)$ is normalized to its peak value $I_{PL}(t=0)$. The figure is plotted with changing β while fixing other parameters, and it clearly shows that the self-absorption strongly affects the PL response. Equation (5.9) is for a delta impulse laser excitation. A real finite width laser pulse can be approximated by a Gaussian or a square pulses. A practical approach to account for the finite pulse width in the analysis of the PL signal, is

to evaluate numerically the convolution integral. If $F'(t)$ is the flux of the actual laser pulse, then the PL response $I_{PL}'(t)$ is

$$I_{PL}'(t) = \int_0^t F'(\tau')\ I_{PL}(t-\tau')\ d\tau'. \tag{5.10}$$

5.2.2 Methodology for the Extraction of τ and S

In the time-domain PL response, the directly measurable parameter is the effective lifetime τ_{eff}, which can be extracted from the slope of the tail part of the decay signal. The effective lifetime is also the only measurable quantity for the time-domain PL analysis. To investigate the effect of S and τ on τ_{eff}, and to extract S and τ from τ_{eff}, we derive analytical expression for the instantaneous effective lifetime τ'_{eff} in terms of S and τ. Since τ_{eff} is extracted from the tail part of the decay signal, the effect of the finite laser pulse width on τ_{eff} is negligible. We, therefore, restrict our discussion on τ'_{eff} only for the delta impulse laser excitation.

τ'_{eff} is defined as the reciprocal slope of the $\ln[I_{PL}(t)]$ vs. t plot. This can be expressed mathematically as

$$\frac{1}{\tau'_{eff}} = -\frac{d}{dt} \ln[I_{PL}(t)]. \tag{5.11}$$

Substituting (5.9) into (5.11), we obtain analytical expression

$$\tau'^{-1}_{eff} = \tau^{-1} - \Omega, \tag{5.12}$$

where $\Omega = \Omega_1/\Omega_2$, and

$$\begin{aligned}\Omega_1 = {} & [\alpha/(\alpha^2 - \beta^2) - \alpha/(\alpha^2 - \Gamma^2)]\ [\alpha^2 D\ FX(\alpha^2 Dt) - \alpha\sqrt{D}/\sqrt{\pi t}] \\ & + [\Gamma/(\alpha^2 - \Gamma^2)]\ [S^2/D\ FX(S^2 t/D) - S/\sqrt{\pi D t}] \\ & - [\beta/(\alpha^2 - \beta^2)]\ [\beta^2 D\ FX(\beta^2 Dt) - \beta\sqrt{D}/\sqrt{\pi t}],\end{aligned} \tag{5.13a}$$

$$\Omega_2 = [\alpha/(\alpha^2 - \beta^2) - \alpha/(\alpha^2 - \Gamma^2)]\ FX(\alpha^2 Dt)$$
$$+ [\Gamma/(\alpha^2 - \Gamma^2)]\ FX(S^2 t/D) - [\beta/(\alpha^2 - \beta^2)]\ FX(\beta^2 Dt). \quad (5.13b)$$

The expression (5.12) clearly shows the reduction of τ'_{eff} with decreasing values of Ω, and illustrates a direct way to extract τ from τ'_{eff}. Note that the expressions (5.13a) and (5.13b) imply that Ω is independent of τ and depends only on the material parameters α, β, S, D and time t. A typical picture to illustrate this behavior is shown in Figure 5.2, where τ'_{eff} is normalized with respect to τ and is plotted against t for five values of β, ranging from 100 to 4100 cm^{-1}. In (5.12), τ'_{eff} is a function of time, but becomes negligibly dependent on time when t is much larger than τ. Mathematically, this is because FX(X) approaches a constant value when X approaches infinity. This negligible dependence of τ'_{eff} on t for large t implies, that with a separately measured τ we can extract S from τ'_{eff}, provided that the information on α, β, and D can be obtained independently. Further examination of the plots in Figure 5.2 shows that τ'_{eff} is only weakly dependent on β when β and t are large. Thus, due to the negligible dependence of τ'_{eff} on t, in what follows, τ_{eff} is defined to be the asymptotic value for τ'_{eff} when $t > \tau$. The dependence of Eqs. (5.13a) and (5.13b) on α implies, that for a very small value of α, when β is also small, Ω is negligible in comparison with τ^{-1}. Therefore, based on (5.12), if we plot τ_{eff}^{-1} versus β for a very small value of α, the intercept with the ordinate is equal to the reciprocal of the lifetime, τ^{-1}. Figure 5.3 shows the results for this analysis. The values for τ_{eff}^{-1} are generated using Eqs. (5.12), (5.13a), and (5.13b) for the decay time t_D = 17 ns. An examination of Figure 5.3 shows that, as β

approaches to 0, the curves with different values of S converge to the same intercept ($= \tau^{-1}$), from which τ can be extracted. Further examination of the plots for large β shows, that the curves become independent of β and are a function of S only. Thus, by graphically fitting the measured values of τ_{eff} for different values of β with the theoretical plots, we can determine S and τ from the best fitting curve.

With the already known value for τ, the resolution in the determination of S can be further improved by performing a strong absorption measurement (large α). This is because for the strongly absorbed excitation light source, the excess carriers are generated very near the sample surface and are highly affected by the surface properties. Figure 5.4 shows τ_{eff}^{-1} versus β plots generated using expression (5.13a), (5.13b), and (5.12) for various values of S for the strongly absorbed excitation. The absorption coefficient α of the external excitation is set to 10^4 cm^{-1} to enhance the dependence of τ_{eff}^{-1} on S. Due to the significant contribution of α to $\mathcal{Q}$ and, thus, on τ_{eff}^{-1}, in contrast to that shown in Figure 5.3, the intercepts of the curves with the ordinate in Figure 5.4 do not converge to the same point. However, similar to the case in Figure 5.3, for large β, the curves become less dependent on β and depend only on S.

A similar analysis can be done by plotting τ_{eff}^{-1} versus α, but fixing β, with S as the parameter. Typical dependencies illustrating this analysis are shown in Figure 5.5. The curves are generated by setting $\beta = 10^4$ cm^{-1}, in correspondence to the value for α in Figure 5.4, for the same values of S as in Figure 5.4. We intentionally set β to the same value as that for α in Figure 5.4, to check the

significance of the dependence of τ_{eff}^{-1} on S for the two approaches. It is interesting to point out, that for this correspondent switch between the value of α and β, the dependence of τ_{eff}^{-1} on α (Figure 5.5) is nearly the same as that for τ_{eff}^{-1} on β (Figure 5.4), regardless of the different dependencies of Q_1 and Q_2 on α and β. Therefore, plotting τ_{eff}^{-1} versus α provides an alternative approach to determine τ and S from the PL decay signals.

To extract τ and S from materials in which the self-absorption effect is negligible, we have devised a similar analysis based on the above methodology. This is done by plotting τ_{eff}^{-1} versus α for different values of S. Figure 5.6 illustrates typical dependencies for this analysis. The curves are generated using Eqs. (5.13a), (5.13b), and (5.12) for $\beta = 0$. Thus, if we measure τ_{eff} from the tail part of the PL decay signal under different excitations, by fitting the measured values for τ_{eff} and the corresponding values of α to the theoretical plots, τ and S can be determined.

5.3 Experimental Setup and Measurements

Photoluminescence measurements were performed to extract τ and S from a GaAs wafer. The wafer is Si-doped n-type GaAs with a doping density $N_{DD} = 2 \times 10^{17}$ cm^{-3} that was chemically passivated about four months before the measurements. The experimental setup is very similar to that used in our previous work [54]. A nitrogen pumped dye laser with 800 ps half pulse width was used as the excitation source. A double-grating monochromator with 0.2 nm resolution was used to separate the luminescence signals detected by an avalanche Si

photodiode with 0.2 ns rise time. The signals were acquired by Tektronix 11402 digitizer having 1 GHz bandwidth. The effective lifetime τ_{eff} was extracted from the semi-log plot in the digitizer display. For the weakly-absorbed excitation measurements, the dye laser was tuned to the wavelength λ = 870 nm, which corresponds to α = 2650 cm^{-1} [47]. The PL signals corresponding to three different wavelengths were picked up by adjusting the monochromator settings. Low injection condition was justified by checking if the peak intensity of the PL signals drops to 1/2 of its original value after inserting 50% attenuator into the laser beam. Figure 5.7 shows the PL decay signals measured at λ = 880 nm, 884 nm, and 886 nm. All the curves have been suitably normalized so that they can be shown together in the semi-logarithmic plot. By examination of this figure, it can be found that the decay slopes for the three signals are different. The noise in the PL response is due to the high-frequency reflection noise in the coaxial cable (see the discussion below). The effective lifetimes are measured from the portion that corresponds to the decay time $t_D \approx 17$ ns from the time when the laser pulse is terminated. Figure 5.8 shows the theoretical dependencies of τ_{eff} vs. β calculated from (5.12), together with the experimental results. The values for β were translated from the corresponding wavelengths using the absorption data from Casey et al. [47]. The solid lines are from theory with setting τ = 52 ns and α = 2650 cm^{-1} [47], while changing S from 10 cm/s to 20010 cm/s with increment of 5000 cm/s. Based on the fits, the extracted value for the lifetime is 52 ns, and the value for S is roughly estimated to be about 10^4 cm/s. Table 5.1 lists the measurement data and the values for β

plotted in Figure 5.8. In generating the theoretical plots in Figure 5.8, the value for the minority-carrier diffusivity D is assumed to be the same as that of the majority carriers in the p-type sample with the same doping density as that in our n-type sample.

Table 5.1. Summary of the experimental data for the weakly absorbed excitation measurements.

wavelength λ (nm)	β (cm^{-1})	τ_{eff} (ns)
880	900	27.8
884	320	33.5
886	210	33.9

To enhance the surface effect on the PL decay so that S can be determined more precisely, the excess carriers have to be injected very near the sample surface. We tuned the dye laser to λ = 735 nm (α = 1.3 x 10^4 cm^{-1} [47]) to achieve this purpose. The excitation wavelength cannot be too short, because the reduction in the excitation wavelength will also result in the reduction of the PL intensity and, hence, make the extraction of τ_{eff} more affected by the measured noise. Figure 5.9 shows the PL signals measured at different wavelengths for the strongly-absorbed analysis. The signals were measured by setting the monochromator to five different output wavelengths. The values of τ_{eff} for each signal were extracted from the portion that corresponds to the

decay time $t_D \approx 17$ ns. Figure 5.10 shows the theoretical curves for τ_{eff} vs. β and the measured data for the strongly-absorbed case. Table 5.2 lists the measured data and the corresponding values for β plotted in Figure 5.10. The values of β are obtained again from Casey et al. [47]. The solid lines are from theory and are used to fit the experimental results to extract S. The theoretical fits are generated by setting τ = 52 ns, obtained from the previous analysis, and changing S from 10 to 20010 cm/s with increment of 5000 cm/s. The best fit shows that S = 8000 $\pm$ 1000 cm/s, which agrees with the value determined from different technique [54].

The measured PL responses in Figures 5.7 and 5.9 are relatively noisy, which affects somewhat the accuracy of the results. The measured high-frequency noise is due partially to the high (1 GHz) bandwidth of the digitizer. The avalanche Si detector is mounted in a TO-18 package attached to a coaxial cable connected to a 50-Ω input of a digitizing oscilloscope. The DC bias for the detector is provided through a microwave biasing-T circuit with a 50-Ω input impedance. The impedance mismatch between the TO-18 package, and the 50-Ω cable and biasing circuit, causes a high-frequency reflection noise in the cable. This noise source can be removed using available fast photodetectors mounted in microwave packages together with the biasing circuit. The relatively noisy signal in Figures 5.7 and 5.9 affects only the accuracy of the results. It is very clear, however, that the slope of the curves in the figures is a strong function of λ, which fully justifies the analysis done above.

Table 5.2. Summary of the experimental data for the strongly absorbed excitation measurements.

wavelength λ (nm)	β (cm^{-1})	τ_{eff} (ns)
880	900	25.3
872	2350	20.6
867	3000	19.0
860	4000	18.0
850	5000	17.9

5.4 Conclusions

A new technique is developed to determine the minority carrier lifetime and the surface recombination velocity in semiconductors. Analytical expression accounting for the self-absorption effect is derived for transient photoluminescence decay in a bulk wafer with arbitrary surface recombination velocity. The technique analyzes the photoluminescence signals measured under different excitations and different self-absorption conditions. Measurement results used to demonstrate the technique are obtained from a GaAs wafer. Due to its contactless and non-destructive nature, the technique is especially useful for the characterization of the surface properties of III-V and other compound materials. The technique is also applicable to monitor the material properties during the wafer processing and specifically to evaluate the surface passivation after different surface treatments. Due to the lov quantum yield in the wafer used in this work [54], we assume that the photo-recycling effect is negligible, and the excess carriers are generated mainly by the external excitation from the laser. For high quantum yield wafers, the internal generation of the excess carriers could be significant when compared with the laser generation, and the effect due to photo-recycling needs to be suitably accounted for. Further study of the photo-recycling effect on the photoluminescence decay from bulk wafers is planned for the future.

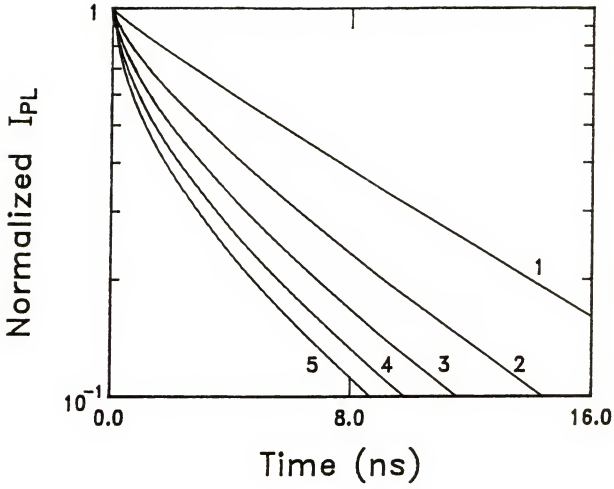

Fig. 5.1. Influence of the self-absorption on the photoluminescence decay after delta impulse excitation. The plots are generated with fixing τ = 10 ns, S = 8000 cm/s, D = 50 cm^2/s, and α = 10^4 cm^{-1}, while changing the self-absorption coefficient β to five different values. The values for β are 100 cm^{-1} (curve 1), 1100 cm^{-1} (curve 2), 2100 cm^{-1} (curve 3), 3100 cm^{-1} (curve 4), and 4100 cm^{-1} (curve 5).

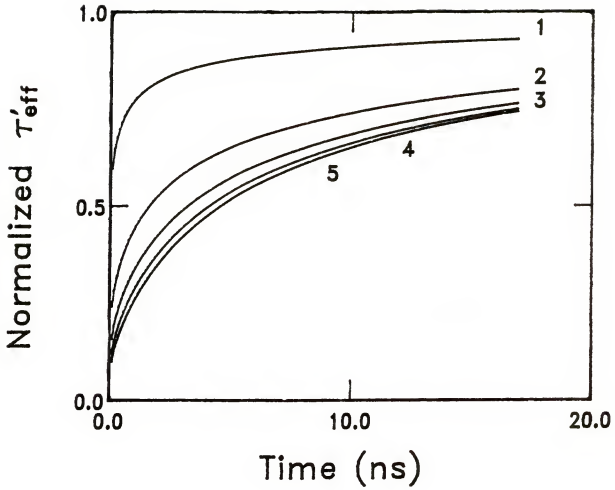

Fig. 5.2. Normalized instantaneous effective lifetime τ_{eff} as a function of the decay time for different values of β. The curves 1 to 5 are generated using the same values for all the parameters as those for the corresponding curves in Fig. 5.1.

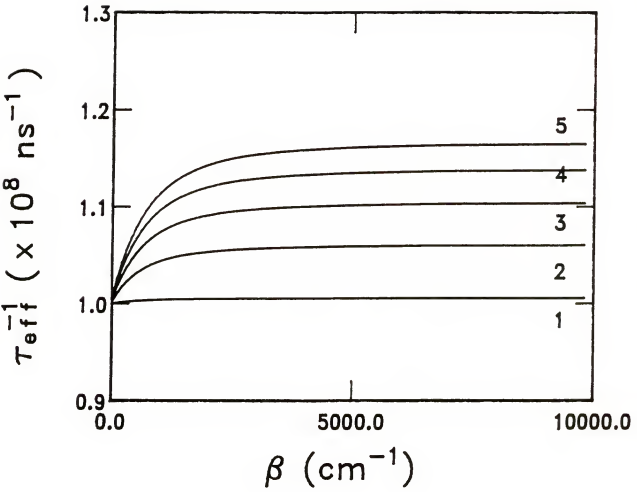

Fig. 5.3. Analysis for a weakly absorbed excitation showing the reciprocal of the effective lifetime as a function of the self-absorption coefficient β for different values of S. The plots are generated with fixing τ = 10 ns, D = 50 cm^2/s, t_D = 17 ns, and α = 20 cm^{-1}, while changing S to five different values: 10 cm/s (curve 1), 10010 cm/s (curve 2), 20010 cm/s (curve 3), 30010 cm/s (curve 4), and 40010 cm (curve 5).

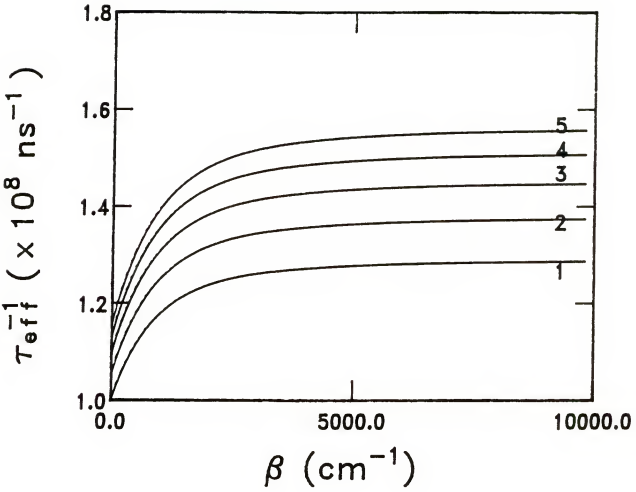

Fig. 5.4. Reciprocal of the effective lifetime as a function of the self-absorption coefficient β for different values of S. The plots are generated by setting $\alpha = 10^4$ cm^{-1}. The rest of the parameters for the curves 1 to 5 are the same as in the corresponding curves in Fig. 5.3.

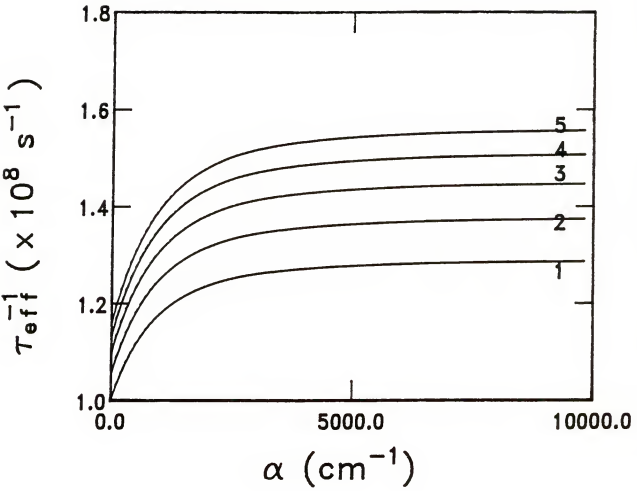

Fig. 5.5. Reciprocal of the effective lifetime as a function of the absorption coefficient α for different values of S. The plots are generated by setting $\beta = 10^4$ cm^{-1}, $\tau = 10$ ns, $D = 50$ cm^2/s, and $t_D = 17$ ns. The curves 1 to 5 correspond to the same values of S as in Fig. 5.3.

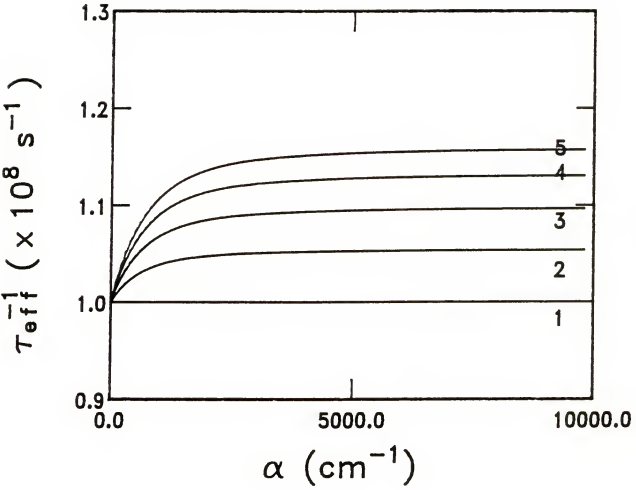

Fig. 5.6. Reciprocal of the effective lifetime as a function of the absorption coefficient α for different values of S. The plots are generated by setting $\beta = 0$ cm^{-1}. The rest of the parameters correspond to the same values as in Fig. 5.5.

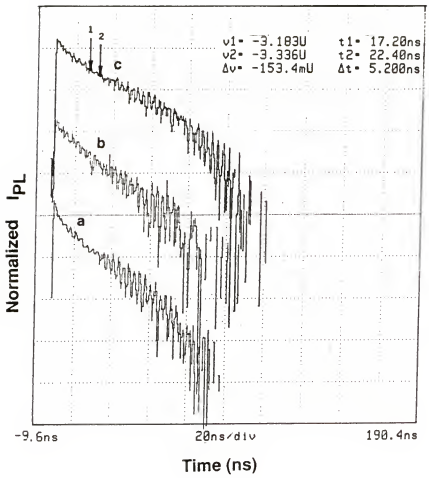

Fig. 5.7. PL decay signals from weakly absorbed excitation measurements. The figure is the hardcopy of the screen of the Tektronix 11402 digitizer. The emission wavelengths λ are: λ = 880 nm (curve a), λ = 884 nm (curve b), and λ = 886 nm (curve c). The information in the legend shows the $\tau_{eff} = -\Delta t/\Delta v$ = 33.9 ns for the curve c. The points from which τ_{eff} was calculated for the curve c are shown by the arrows.

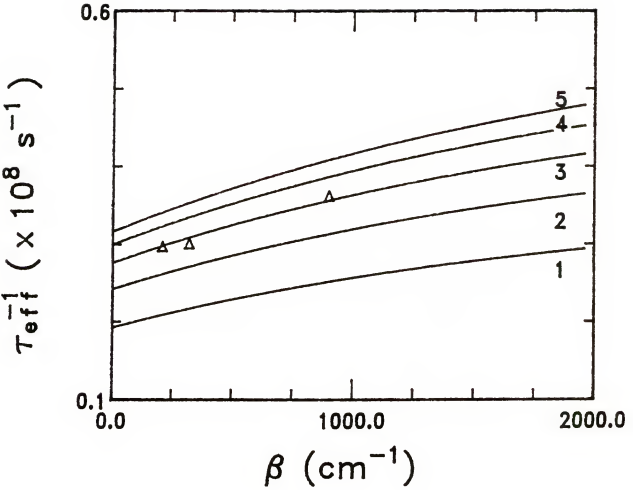

Fig. 5.8. Experimental data (Δ) and the theoretical dependencies (solid lines) for the weakly absorbed excitation. The curves were generated by setting τ = 52 ns, t_D = 17 ns, D = 7 cm^2/s, and α = 2650 cm^{-1}, while changing S to five different values: 10 cm/s (curve 1), 5010 cm/s (curve 2), 10010 cm/s (curve 3), 15010 cm/s (curve 4), and 20010 cm (curve 5).

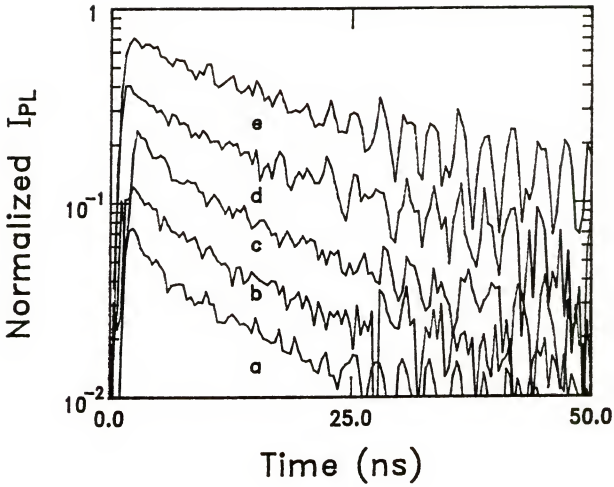

Fig. 5.9. PL decay signals for the strongly absorbed excitation measurements. The emission wavelengths λ are: λ = 850 nm (a), λ = 860 nm (b), λ = 867 nm (c), λ = 872 nm (d), and λ = 880 nm (e).

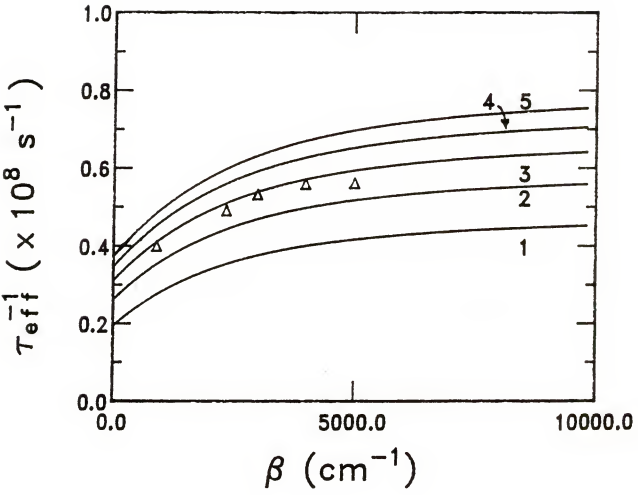

Fig. 5.10. Experimental data (Δ) and theoretical dependencies (solid lines) for the strongly absorbed excitation. The theoretical curves were generated by setting τ = 52 ns, t_D = 17 ns, D = 7 cm^2/s, and α = 1.3 x 10^4 cm^{-1}, while changing S to five different values: 10 cm/s (curve 1), 5010 cm/s (curve 2), 10010 cm/s (curve 3), 15010 cm/s (curve 4), and 20010 cm/s (curve 5).

CHAPTER 6
LIFETIME AND SURFACE/INTERFACE RECOMBINATION VELOCITY MEASUREMENT IN THIN SEMICONDUCTORS LAYERS

This chapter presents a new nondestructive photoluminescence (PL) method for measurement of the bulk lifetime τ and surface/interface recombination velocity S in thin layers. The method is based on an exact analytical solution for the PL decay in a thin semiconductor layer. S and τ are obtained by analyzing the PL-decay response to a pulsed laser excitation for layers with different thicknesses. The decay analysis is done in the frequency domain which improves accuracy and suppresses noise. The method is demonstrated on isotype double AlGaAs/GaAs/AlGaAs heterostructure, but is also applicable for thin layers bounded by interfaces with different recombination velocities, such as SOI, GaAs/Si, and $Si_{1-x}Ge_x$/Si systems.

6.1 Introduction

Nondestructive measurement techniques are the preferred ones among various characterization methods. They can serve as a process monitor in the development and optimization of processing techniques for different semiconductors. They can also be applied to study the fundamental physics and to measure basic material properties. Due to its nondestructive properties, the photoluminescence (PL) decay measurement has been widely employed for the characterization of semiconductor thin films [35,37,55].

GaAs thin layers grown by molecular beam epitaxy (MBE) or by metal-organic chemical vapor deposition (MOCVD) are of special interest for the fabrication of high efficiency solar cells, high performance heterojunction bipolar transistors (HBTs), and optical electronic devices. For solar cells, the ultimate quantum efficiency depends mainly on two material parameters: the recombination lifetime of excess carriers in the active layer τ and the recombination velocity at the interface S. In designing the cells to achieve their optimum performance, the knowledge of these parameters is essential. The typical procedure used to obtain the values for these parameters is to fit the quantum yield spectra measured on the finished cells to the theoretical model. Recently, Borrego and Ghandhi [56] reported an alternate way to extract τ and S by measuring excess carrier decay from the isotype double heterostructure (DH) layers. The results reported in [56] are basically based on the PL decay measurements widely used for the study of surface passivation on GaAs thin layers [35]. In principle, the technique monitors the PL decayed signal by using a single photon counting system [35]. In studying the electrical properties of the passivated GaAs layer, isotype DH $Al_{0.5}Ga_{0.5}As/GaAs/Al_{0.5}Ga_{0.5}As$ [35] and $Ga_{0.5}In_{0.5}P/GaAs/Ga_{0.5}In_{0.5}P$ [57] layers with different active layer thicknesses d are employed. The injected excess carriers are confined in the active layer (GaAs) due to the presence of the two adjacent wider-energy gap confinement layers. Under low injection condition, the carrier decay is exponential and depends solely on the material properties, which can be characterized by a single parameter, the effective lifetime τ_{eff}. In the time-domain analysis, τ_{eff} is extracted by analyzing the decay rate of the excess carriers. From the photoconductive decay theory, τ_{eff}

can be approximately expressed as $\tau_{eff}^{-1} = \tau^{-1} + \tau_s^{-1}$, where τ_s accounts for the recombination at the interface and has the expression $\tau_s = d^2/\pi^2 D + d/2S$ [55] (D is the minority carrier diffusivity). For DH samples, the diffusion part ($d^2/\pi^2 D$) in τ_s is usually negligible, and the expression can be simplified to $\tau_{eff}^{-1} = \tau^{-1} + 2S/d$ [55]. Therefore, plotting τ_{eff}^{-1} versus d^{-1}, with the values for τ_{eff} that are obtained for different values of d, gives the interface recombination velocity S and bulk lifetime τ from the slope and the intercept of the plots. The drawback in this technique is that in order to extract S and τ, samples with different active-layer thickness need to be prepared under the same growth conditions to preserve the same material properties of the interfaces and active layers of different samples. In addition, as pointed out in our earlier work [54], the noisy decay signal from the measurement itself prevents a further effort to improve the accuracy from the time-domain analysis.

In this chapter, we present a new technique to determine S and τ from semiconductor thin films. The parameters are determined from the transient PL decay induced when a laser pulse creates electron-hole pairs in the active layer of the isotype DH sample. Taking advantage of the frequency-domain analysis [54], instead of analyzing the signal in the time domain, we analyze the PL decay in the frequency domain for the parameter extraction. This is done by taking the Fourier transform of the PL decay which is then compared with the analytical expressions relating the input to the output in the frequency domain. The analytical expression is obtained by solving the continuity equation in

the frequency domain. Based on this expression, a procedure to determine S and τ from thin layers is devised. For a layer with an intermediate thickness about equal to the diffusion length, $d \approx L$, the approximate model employed in Nelson and Sobers [35] results in an error of at least 5 % [34]. The new analytical expression derived below and used in the new technique is exact and is good for layers of any thickness. In addition, it is also good for layers with different S for the top and bottom interfaces. Therefore, this technique is also applicable to samples with non-isotype DH layers, e.g. samples with P/n/N or N/p/P structures (the capital N and P is by convention associated with the material of large energy gap). Although the technique is developed for thin films, it is not subject to the restricted conditions that the layer thickness d has to satisfy $d \ll L$ and $S \ll D/d$ [35].

The model presented here is demonstrated by measuring the luminescence to monitor the excess charge decay rate, and it is generally applicable to other types of methods that can monitor the excess carrier density. These methods include measuring recombination lifetime by microwave reflection, infrared absorption, and induction current. The technique presented here is demonstrated on GaAs thin film, its extension to other materials with finite thickness is straightforward. The technique could be also useful for characterizing SOI (silicon on insulator) Si layers for wafer screening and process monitoring.

6.2 Frequency-Domain Photoluminescence Decay for a Thin Layer

Throughout the analysis, the widely employed low injection condition is assumed. This assumption assures that the minority carrier lifetime is characterized by a constant τ, and hence preserves the linearity of the system required for Fourier analysis. This assumption also assures that the minority carrier transport parameters are injection-independent, which validates the transformation of the three-dimensional continuity equation into the one-dimensional equation [33]. With this transformation, the PL decay was shown to be independent of the beam size, shape, and uniformity [33]. This implies that a focused beam, which can result in locally high injection, is completely unnecessary. Thus, it greatly simplifies the problem we deal with.

In the following analysis, laser light is chosen as the excitation source. Although various kinds of excitation sources (e.g. E-beam and light) have been used to study the PL decay, for DH samples, only light source can be employed to inject carriers into the active layer. This is because E-beam will be blocked by the window layer of the sample, but light will not if a suitable wavelength is chosen.

6.2.1 Analytical Expression in the Frequency Domain

Let us consider a semiconductor sample of thickness d with the z axis perpendicular and with the x and y axes parallel to the sample surface. We assume the sample is a uniformly doped n-type material

(extension to p-type is straightforward). The surfaces at z = 0 and z = d can be the interfaces of a DH sample. We also assume that the surface at z = 0 is irradiated by a defocused laser beam that generates excess holes with density Δp. Based on the assumptions and the discussion made above, the three-dimensional continuity equation can then be simplified to the one-dimensional expression [33]

$$\frac{\partial P}{\partial t} = D \frac{\partial^2 P}{\partial z^2} - \frac{P}{\tau} + G(t)\,(1 - R)\,\alpha\, e^{-\alpha z}, \qquad (6.1)$$

where P is the number of excess holes per unit of depth in the x-y plane given by $P = \int_{-\infty}^{\infty}\int_{-\infty}^{\infty} \Delta p \, dx \, dy$ and is a function of z and t, α is the absorption coefficient of the excitation source, and R is the reflection coefficient. It is noted that, in (6.1), G(t) is the total excitation flux in the x-y plane given by $G(t) = \int_{-\infty}^{\infty}\int_{-\infty}^{\infty} g(t) \, dx \, dy$, where g(t) is the flux per cubic volume. Performing Fourier transformation on both sides of Eq. (6.1), we then have

$$D\partial^2 P'/\partial z^2 - (j\omega + 1/\tau)P' + G'(\omega)\,(1 - R)\, e^{-\alpha z} = 0, \qquad (6.2)$$

where P' and G' is the frequency domain counterparts of P and G, respectively, $j = \sqrt{-1}$, and $\omega = 2\pi f$, where f is the frequency.

In the frequency domain, the boundary conditions for the diffusing carriers that recombine at the two surfaces/interfaces are

$$S_2\, P'(\omega,d) = -\, D \frac{\partial P'(\omega,d)}{\partial z}, \quad S_1\, P'(\omega,0) = D \frac{\partial P'(\omega,0)}{\partial z}, \qquad (6.3)$$

where S_1 and S_2 correspond to the surface/interface recombination velocities at z = 0 (top surface) and at z = d (bottom surface), respectively. Solving Eqs. (6.2) and (6.3), we obtain, after lengthy algebra, the solution

$$P' = \alpha\,(1 - R)\, G'\,(A\, e^{z/L'} + B\, e^{-z/L'} - C\, e^{-\alpha z}), \qquad (6.4)$$

where

$$A = \frac{\alpha}{(\alpha^2 - L'^{-2})} \times \left(\frac{(S_1/\alpha D + 1)(S_2 - \Lambda)\, e^{-d/L'} - (S_2/\alpha D - 1)(S_1 + \Lambda)\, e^{-\alpha d}}{(S_1 - \Lambda)(S_2 - \Lambda)\, e^{-d/L'} - (S_2 + \Lambda)(S_1 + \Lambda)\, e^{d/L'}} \right),$$

$$B = \frac{\alpha}{(\alpha^2 - L'^{-2})} \times \left(\frac{(S_1/\alpha D + 1)(S_2 + \Lambda)\, e^{d/L'} - (S_2/\alpha D - 1)(S_1 - \Lambda)\, e^{-\alpha d}}{(S_1 + \Lambda)(S_2 + \Lambda)\, e^{d/L'} - (S_2 - \Lambda)(S_1 - \Lambda)\, e^{-d/L'} } \right),$$

$C = 1/[D\,(\alpha^2 - L'^{-2})]$, $L' = L/(1 + j\omega\tau)^{1/2}$, $L = \sqrt{D\tau}$, and $\Lambda = D/L'$.

The photoluminescence intensity I_{PL} resulting from the electron-hole recombination is proportional to the $P(\omega,z)$, and can be evaluated using

$$I_{PL}(\omega,\lambda) = \frac{\Theta\, \gamma(\lambda)}{\tau_r} \int_0^d P'(\omega,z)\, e^{-\beta(\lambda)z}\, dz, \qquad (6.5)$$

where Θ is a constant accounting for the solid emission angle and the reflection of the emitted luminescence from the front surface, $\gamma(\lambda)$ is the normalized PL spectrum [54], τ_r is the radiative lifetime, and $\beta(\lambda)$ is the self-absorption coefficient. In (6.5), the exponential term accounts for the self-absorption effect on the emitted luminescence signal. The factor outside the integral is usually hard to determine, but will be cancelled out after we normalize $I_{PL}(\omega,\lambda)$ with respect to its zero-frequency response $I_{PL}(0,\lambda)$. We will show this in more detail in later section.

Using (6.4), we complete the integration and have

$$I_{PL}(\omega) = K\, G'(\omega)\, F(\omega), \tag{6.6}$$

where $K = \alpha\,(1 - R)\,\Theta\,\gamma/\tau_r$,

and $$F(\omega) = \frac{A\,\{\exp[(L'^{-1} - \beta)d] - 1\}}{(L'^{-1} - \beta)} - \frac{B\,\{\exp[-(L'^{-1} + \beta)d] - 1\}}{(L'^{-1} + \beta)}$$

$$+ \frac{C\,\{\exp[-(\alpha + \beta)d] - 1\}}{(\alpha + \beta)}. \tag{6.7}$$

The symbols have been defined in (6.4). We will focus the following analysis on the luminescence signal corresponding to a wavelength λ. Therefore, for brevity, we have dropped out λ in (6.6) and (6.7).

6.2.2 Analysis for Determining S and τ

We restrict the analysis for DH layers with the same top and bottom interface/surface recombination velocity, $S_1 = S_2 = S$. A quantity useful for determining S and τ from experiment is the normalized frequency response $F_{nor}(\omega)$ given by the relation [54]

$$F_{nor}(\omega) \triangleq F(\omega)/F(0) \tag{6.8a}$$

$$= I_{PL}(\omega)\, G'(0)/[I_{PL}(0)\, G'(\omega)], \tag{6.8b}$$

where $F(0)$, $G'(0)$, and $I_{PL}(0)$ are the zero frequency component of $F(\omega)$, $G'(\omega)$, and $I_{PL}(\omega)$, respectively. It is noted that in (6.8b), the normalization feature enables the analysis without the knowledge of the constant K in (6.6), which is difficult to accurately determine from experiment. Therefore, this simplifies the experimental procedure, and hence minimizes the uncertainty in the measurement. In addition, the normalization also takes care of the finite system response, which could be due to the laser pulse or the detector. Therefore, it also

increases the accuracy of the measured response. In (6.8b), $I_{PL}(\omega)$ and $G'(\omega)$ can be determined by performing Fourier transform on their time domain counterparts $I_{PL}(t)$ and $G(t)$, which are experimentally measurable. The theoretical $F_{nor}(\omega)$, obtained by using expressions (6.7) and (6.8a), depends on a given set of the material parameters (S, τ, d, α, β). Therefore, by fitting the theoretical $F_{nor}(\omega)$ to the experimental $F_{nor}(\omega)$, S and τ can be extracted provided other parameters can be independently determined.

To determine S and τ experimentally, we need to investigate the influence of various experimental conditions on the PL decay. We try to avoid those conditions with uncertainty, which in turn yield inaccuracy in the results, but employ those conditions that are well controllable. We use Eqs. (6.7) and (6.8a) to analyze their dependence for different conditions. First, we investigate the effect due to light wavelength. With light, by using different wavelengths, the carriers can be injected either near the sample surface or in depth. By checking the dependence of $F_{nor}(\omega)$ on α and β numerically, for a thin layer, we found a very weak dependence of the response on α and β. This implies that the response is insensitive to the excitation depth, and the procedure to extract S and τ by using different light wavelengths is not feasible. Nevertheless, at the same time, this also implies that the result is not affected by the uncertainties in the values of α and β. For III-V compound semiconductors, this is especially helpful, because the value for α (or β) is strongly doping-dependent with uncertainty of the order of 20% or higher [47]. Thus, for an accurate extraction of S and τ, a thin layer is essential, because it results in the negligible dependence of $F_{nor}(\omega)$ on α and β, and hence avoids the uncertainty introduced by those parameters.

Second, we have also investigated the dependence of $F_{nor}(\omega)$ on the carrier diffusivity D. A very weak dependence of $F_{nor}(\omega)$ on D was found for thin layers. Physically, this is because for thin layers ($d < L$), the carrier diffusion is very negligible. This weak dependence on D also implies that the frequency response is insensitive to the uncertainty due to D, an advantage similar to the case for α and β. In some materials, the minority-carrier diffusivity has not been well characterized. However, this technique has the advantage that allows us to take the diffusivity data for the minority carriers from the data for the majority carriers without sacrificing the accuracy of the analysis.

Third, we investigate the effect due to the layer thickness. Figures 6.1(a) and 6.1(b) show the dependence of the amplitude of $F_{nor}(\omega)$ on S for layers with $d < L$ and $d << L$. The plots are obtained numerically from the theory (Eqs. (6.7) and (6.8a)) by fixing τ but changing S as a parameter. For layers with $d < L$, the carrier recombination is composed of both the bulk and the surface recombination. For the thinner layer ($d << L$), the luminescence becomes more sensitive to S than τ. Physically, this is because the excess carriers are more likely to recombine at the surface/interface than in the bulk. Therefore, for layers with $d << L$, a stronger dependence of $F_{nor}(\omega)$ on S than that for $d < L$ layer is observed.

A separate analysis for the frequency response was performed to check the dependence of the corner frequency ω_c on S and τ. The results shows that the overall frequency response for a given ω_c can be fitted equally well by various sets of τ and S. This implies that the values for the best fitted S and τ are not unique, and hence makes the

determination of τ and S from a single layer impossible. To enable the extraction, we developed a computer program that generates all sets of (τ, S) that fit equally well to a given response. The program is based on Eqs. (6.7) and (6.8a), and the values for various sets of (τ, S) are obtained through iteration. Using this program, we examine the values of (τ, S) for layers with the same electrical properties (e.g. same S and τ, same doping density, etc.), but with different thicknesses. The analysis is done by plotting S versus τ for all the sets of (τ, S) for the three layers with different thicknesses. The actual values for (τ, S) are extracted from the intercept of the curves. Figure 6.2 illustrates typical results for this analysis. The different slopes come from different degree of participation of the bulk recombination in the total recombination. The decrease of the slope for the thinner layers implies that the extracted S from a thinner layer is much less affected by the uncertainty in τ. An extreme condition is for the case when the slope approaches nearly zero, or equivalently, the accuracy of the values for S from the curve fitting is nearly independent of that for τ. This is the condition for very thin layers ($d \ll L$), and implies that S can be extracted from a single layer without the knowledge of an accurate τ. To obtain the value for τ, an additional layer with different thickness is still essential. We will demonstrate the extraction procedure based on the measurement results in next Section. Since the layer thickness can be well defined by modern thin film growth techniques, using layers with different thicknesses provides a more practical approach for determining τ and S.

6.3 Photoluminescence Measurements of S and τ

6.3.1 Experimental Setup

The photoluminescence experiments were done at room temperature (296 K). The samples used in this work are N-$Al_{0.4}Ga_{0.6}As$/n-GaAs/N-$Al_{0.4}Ga_{0.6}As$ double heterostructures shown in Figure 6.3. The layers were grown by MBE on (100) GaAs substrate at a temperature of 650°C. Two samples with the same structure, but with different thicknesses (d = 0.3 μm and 0.5 μm) of the GaAs layer were grown. The n-GaAs layers are silicon-doped with donor concentration $N_{DD} = 1 \times 10^{17}$ cm^{-3}. The N-AlGaAs layers are 1500 Å thick and are silicon-doped with $N_{DD} = 1 \times 10^{18}$ cm^{-3}. The two AlGaAs layers serve as both surface passivation and carrier confinement for the active layer (n-GaAs). The GaAs layers were grown very thin (less than 1 μm) to avoid the photo-recycling effects [35] and to minimize the uncertainty introduced by α and β (see Sec. 6.2.2.). The samples were grown under the same conditions to assure the same interface/surface and bulk properties in the GaAs layers.

The experimental setup for the time-resolved photoluminescence measurements is similar to that used in our previous work shown in Figure 4.8. Dye laser with pulse width of 800 ps pumped by a nitrogen laser was used as the photoexcitation source. The wavelength of the dye laser $\lambda = 740$ nm was suitably tuned such that the incident laser light penetrates through the wide-energy-gap AlGaAs cap layer and is completely absorbed in the GaAs active layer. The laser light was focused into a 2 x 9 mm^2 spot by using a cylindrical lens to help the

efficient collection of the luminescence light from the sample. While focusing the light, we noticed that the peak intensity of the signal dropped to about one-half of the original value after inserting a 50% attenuator to the laser beam. This validates the low injection condition required for the measurements. The low-injection requirement was also justified through checking the decay curve of the measured signal. At higher excitation levels, a non-exponential decay is, in fact, observed as a result of ambipolar recombination. The PL decay signals were collected by using an objective lens mounted on a XYZ micropositioner and were focused on the entrance slit of a double grating monochromator for light separation. Two high-pass filters with cut-on wavelength of 800 nm were put in front of the entrance slit to block the stray light from the laser. The PL signal selected by the monochromator was detected using a silicon avalanche photodiode (APD) with a rise time of 0.2 ns (under a reverse bias V_R = 150 V). The bias was applied through a biasing-T that passes only the transient signal to the digitizer. The measured PL signal was acquired using the Tektronix 11402 digitizer (1 GHz bandwidth) and was subsequently transferred to a Mini-VAX computer through IBM PC for data analysis.

6.3.2 Measurements and Results

Figure 6.4 shows the photoluminescence decay signals from samples with GaAs layer thickness d = 0.5 μm (curve a) and d = 0.3 μm (curve b). The curves are plotted after taking the natural logarithm on the luminescence intensity. Both signals were suitably normalized so that they can be shown in the same figure. The different slopes in the signals are because of the different thicknesses of the layers.

To justify the negligible dependence of $F_{nor}(\omega)$ on β experimentally, we have measured the PL signals at different emission wavelengths for the layer with d = 0.5 μm. No significant difference was found in this analysis, as was expected from the simulation in Sec. 6.2.2. Therefore, throughout the whole measurements, the PL decay signals were taken at the wavelength corresponding to the peak of the spontaneous emission in GaAs ($\lambda \simeq 870$ nm) to obtain the optimum intensity. The system response was measured by directly striking the detector with the laser beam, and was subsequently used to normalize the PL decay signals to account for the effects due to the finite laser pulse width and finite rise time of the detector. While measuring the system response, the signal intensity was kept on the same level as that for the PL decay signal to avoid changing the measurement condition.

Figures 6.5(a) and 6.5(b) show the frequency domain analysis of the signal shown in Figure 6.4(a) for d = 0.5 μm. The solid line is the experimental result obtained after performing the Fourier transform on curve (a) in Figure 6.4. The dotted lines come from the theory, and are used to fit the experimental results for extracting τ and S. Both the experimental and theoretical curves are obtained by normalizing the frequency response with respect to its zero-frequency component. The best fit of the measured curves to the theory can be obtained either by changing the values for S while choosing a value for τ or by changing the values for τ while choosing a value for S. For thin layers, the stronger dependence of the response on S suggest us to generate the fits by changing S as the fitting parameter while fixing τ as a known parameter. Figure 6.5(a) illustrates the parameter extraction for τ

and S from the amplitude analysis. A first estimate for the value of τ is obtained through roughly estimating a value larger than ω_c^{-1} from the experimental response. The value of S is then obtained from the best fit through checking the fitting curves graphically. Similar procedure was used in figure 6(b) for the phase analysis. Physically, the phase delay angle θ is a measure of the phase delay between the PL signals and the excitation source at a sinusoidal frequency ω. The optical delay due to the measurement setup was suitably accounted for in doing the phase delay calculation. Instead of plotting θ in Figure 6.5(b), we plot $\tan(-\theta)$ for the phase delay analysis. This is because $\tan(-\theta)$ provides a higher resolution than θ in the parameter-extraction procedure. The straight line dependence for the phase plots indicates that the luminescence signal is an exponential decay curve in the time domain [54]. Though oscillating in some frequency ranges, the solid line in Figure 6.5(b) still shows a straight-line dependence. The deviation for the values of S resulting from the oscillation in this figure is less than $\pm$ 9%. A comparison of this deviation with that from the time domain analysis will be shown in next Section to address more explicitly the advantages of the new technique.

From the best fits of both the amplitude and phase plots, the extracted values for d = 0.5 μm are τ = 60 ns and S = 500 cm/s. It should be noted that this set of values is not the only one that fits the experiment. As pointed out earlier, the experimental response can actually be fitted equally well by other sets of values for τ and S. The use of the values for (τ, S) obtained here is to find the other sets for (τ, S), from which the actual values for (τ, S) can be extracted by combining results from a similar analysis for a layer with another thickness.

Figures 6.6(a) and 6.6(b) show the frequency-domain analysis for the layer with thickness d = 0.3 μm. The solid line is the frequency response after performing the Fourier transform on the signal from Figure 6.4(b). The theoretical plots in both figures are obtained by fixing τ = 50 ns, a value estimated from ω_c^{-1}, and changing S from 350 to 650 cm/s with increment of 100 cm/s. The different response compared with that in Figure 6.5 is a result of the different layer thicknesses. The higher resolution for S in Figure 6.6 indicates that a thinner layer response is more sensitive to the changes in S. This is because for very thin layers, the recombination of the excess carriers in the bulk becomes negligible in comparison with that through the surface. It is noted that both Figures 6.5 and 6.6 show a slight increase for the best fitted values of S when going from the low-frequency to high-frequency regions. This change in S can be attributed to a possible dependence of S on the levels of excess carrier concentration. From both the amplitude and phase analysis for layer with d = 0.3 μm, the extracted values are τ = 50 ns and S = 400 cm/s.

We have used the values for τ and S determined from the above analyses for d = 0.3 μm and d = 0.5 μm, to generate all the other sets of values for (τ, S). Figure 6.7 illustrates the results. Also shown in Figure 6.7 are the two data points for (τ, S) obtained from the analyses in Figures 6.5 and 6.6. Curves (a) and (b) in Figure 6.7 correspond to the values of (τ, S) that can generate the best fit to the experimental responses in Figures 6.5 and 6.6. Due to the difference in the layer thicknesses, the slopes of the two curves are different. The values for the actual τ and S are determined from the

intercept of the two curves. This is because the fits generated by the (τ, S) for the two different thicknesses can be both well fitted into the experimental responses (solid lines) in Figures 6.5 and 6.6. The values extracted from the intercept are τ = 41 ns and S = 356 cm/s. The value for S determined from this work is comparable to the results (S = 450 ± 100 cm/s) for p-GaAs layer reported in the literature [35].

6.3.3 Discussion

For a comparison of this technique with the time-domain analysis, we performed the analysis for the measured signals in the time domain, from which we obtain τ_{eff} from the best fit to the PL decay signals. Figure 6.8 shows the typical results giving a direct visual indication of whether the decay kinetics are of a simple exponential form with a constant τ_{eff}. The straight lines correspond to the best fitted curves generated by using a computer program. The fitted curves were chosen to fit the decay signals only within a specified range of time. Since the slopes of the tail parts are strongly affected by the noise, the tail part is not included in generating the best fit. The effective lifetimes obtained from the slopes are τ_{eff} = 26 ns and τ_{eff} = 17 ns for the samples with d = 0.5 μm and d = 0.3 μm, respectively. To check the deviation for the values of τ_{eff} measured at different parts of the signal with τ_{eff} obtained from the overall best fit, we plotted in Figure 6.9 τ_{eff} versus time with incremental time of 0.4 ns for the sample with d = 0.5 μm as an illustration. The deviation is about 19 % of the τ_{eff} from the best fits when the decay time t < 40 ns, and increases to ~ 35 % or more when the decay time is within the range of

50 ns < t < 70 ns. This deviation is a result of the fluctuations in the decay signal, and is unavoidable because of the fluctuations of the laser output intensity and the high frequency noise from the electrical setup. However, as we have shown in Section 6.3.2, the deviation for the parameters extracted from frequency domain can be as low as ~ 9 %, which greatly improves the reliability of the measured results. In Figure 6.9, the increase of the deviation with time introduces additional difficulties in extracting the value for τ_{eff} from the region where the decay signal is below 20 % of its peak value. Therefore, only part of the decay curve can be used in doing the best fit. However, in the frequency-domain analysis, the entire decay curve can be employed in the analysis regardless of the noisy tail signal. This is especially helpful for extracting very short (nanosecond or sub-nanosecond) lifetime from heavily doped semiconductors. This is because for very short lifetime measurement, the high-frequency noise becomes more apparent in the luminescence decay.

Perhaps the best illustration of the improved accuracy and noise suppression of the present method compared to the time-domain analysis, can be made by comparing Figures 6.5(b) and 6.6(b) with Figure 6.8. In all three figures the fit of theory with experiment is a straight line. It is very clear, however, that the noise was filtered out in the frequency-domain curves, which makes the fit more accurate. This is clearly evidenced, in particular, by comparing Figure 6.6(b) with curve (b) in Figure 6.8. The Fourier transform into the frequency domain used the entire time-domain spectrum and the entire bandwidth of the system. The noise in the time-domain signal can be suppressed by frequency filtering. This will, however, reduce the system bandwidth

which is very undesirable for measurement of short lifetimes. As demonstrated in Figures 6.5 and 6.6, in the frequency-domain the noise suppression can be achieved without limiting the system bandwidth. Other advantages of the frequency-domain measurements are discussed in Wang and Neugroschel [54].

6.4 Conclusions

A new nondestructive measurement technique is developed and demonstrated on the MBE grown-double heterostructure layers. The technique allows a more accurate determination of the minority carrier lifetime and the surface recombination velocity from layers of finite thickness compared to other techniques. A new and exact analytical solution was obtained by solving the continuity equation in the frequency domain for layers of any thickness, and was applied for the extraction of parameters from layers with thicknesses less than the diffusion length. The technique is also applicable when the sample thickness is greater than the diffusion length. It is especially suitable for the characterization of heavily doped semiconductor samples with submicron diffusion length and sub-nanosecond lifetime. A comparison of the accuracy of the technique with that from the time-domain analysis is made, based on the signals measured from the luminescence decay. From the comparison, the advantages for the new technique are emphasized.

Due to its nondestructive features, the technique presented here can provide parameters for evaluation of materials, monitoring of material growth, and design and modeling of devices. The technique

also has potential in the development of the passivation process for III-V and II-VI compound materials. The application of this technique to the characterization of the bulk GaAs on Si and GaAs/Si interface properties is planned.

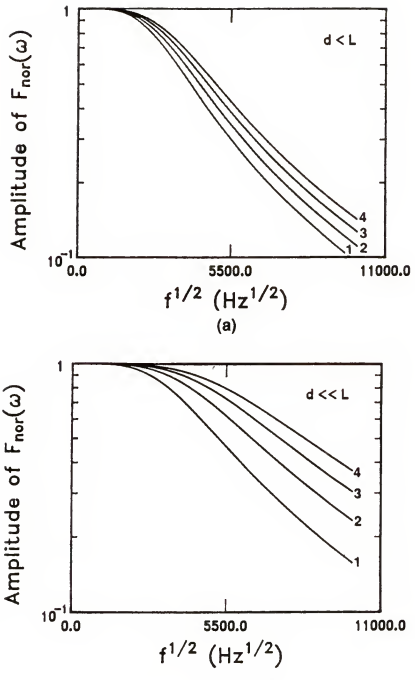

Fig. 6.1. Amplitude of the normalized frequency responses for layers with d < L (d ≈ 0.3 L) (a) and with d << L (d ≈ 0.06 L) (b). Curves 1, 2, 3, and 4 corresponds to S = 500, 1000, 1500, and 2000 cm/s, respectively. The response is normalized with respect to its zero frequency component.

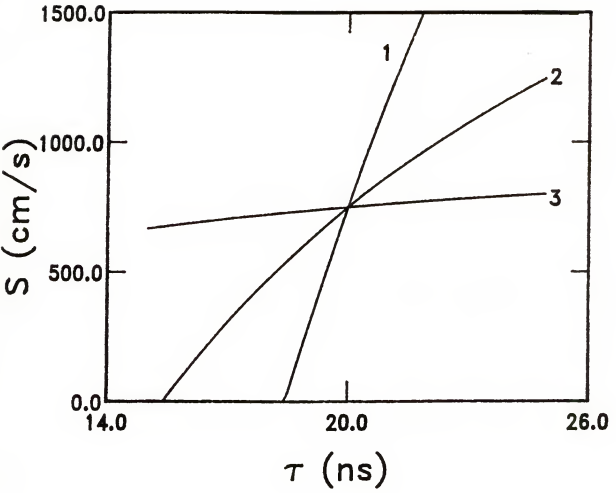

Fig. 6.2. Figure showing various sets of S and τ for layers of different thicknesses. Each curve gives the values for (τ, S) that corresponds to the same frequency response. Curves 1, 2, and 3 are for layers with $d \approx L$, $d < L$ ($d \approx 0.3\ L$), and $d \ll L$ ($d \approx 0.03\ L$), respectively.

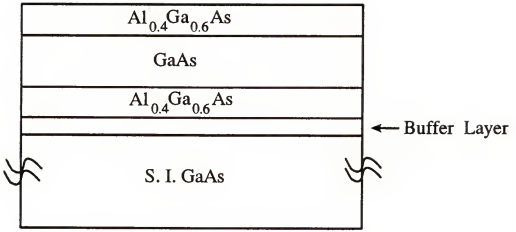

Fig. 6.3. Schematic diagram of the sample structure.

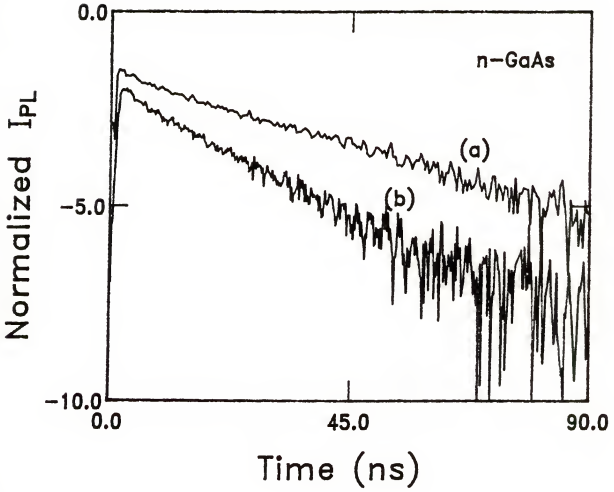

Fig. 6.4. Photoluminescence time decay signals of n-GaAs DH samples at 296 K for two different thicknesses d = 0.5 μm (a), and d = 0.3 μm (b).

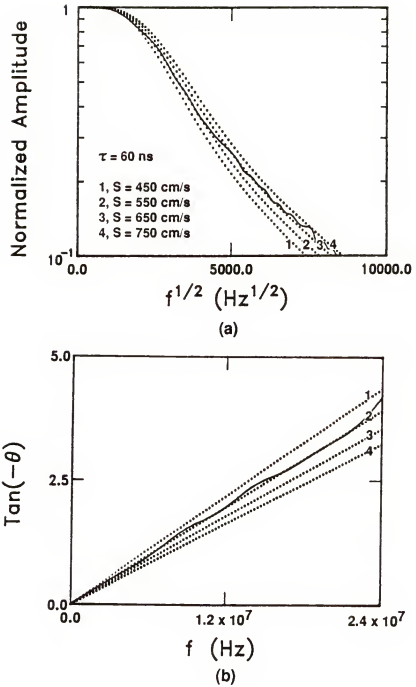

Fig. 6.5. Amplitude (a) and phase (b) of the frequency response for the n-GaAs layer with d = 0.5 μm. The solid line comes from the experiment. The dotted lines are the theoretical plots obtained with fixing τ = 60 ns, and changing S from 450 to 750 cm/s with increment of 200 cm/s. Both figures are plotted against the square root of the frequency.

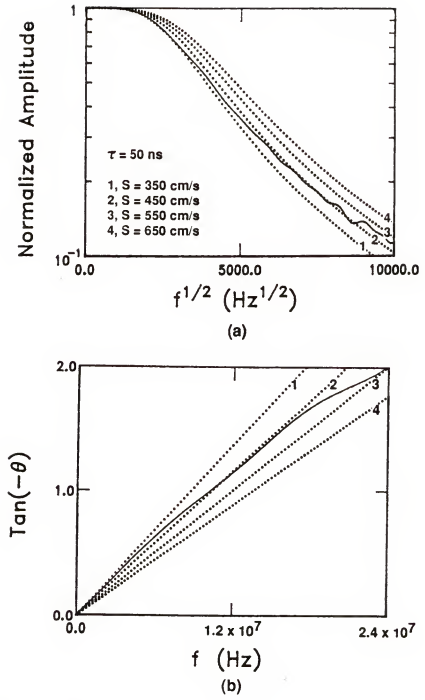

Fig. 6.6. Amplitude (a) and phase (b) of the frequency response for the n-GaAs layer with d = 0.3 μm. The solid line is from the experiment. The dotted lines are the theoretical plots obtained with fixing τ and changing S. Both figures are plotted against the square root of the frequency.

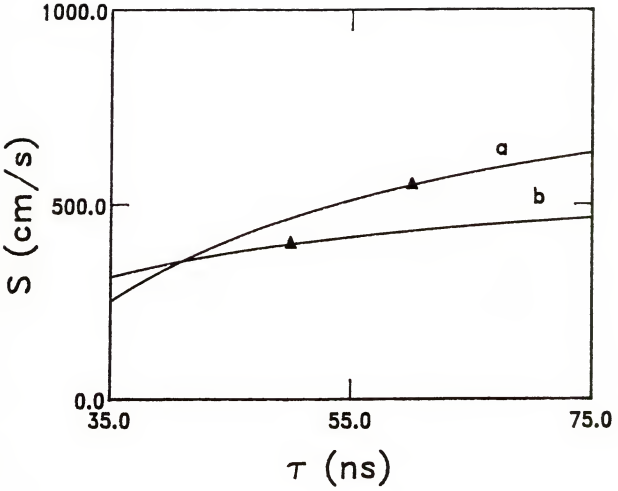

Fig. 6.7. Figure shows the sets of values of (τ, S) for n-GaAs layers with d = 0.5 μm (a) and d = 0.3 μm (b). Curves (a) and (b) are generated based on the first sets of values (▲) for (τ, S) obtained from the best fits in Figs. 6.5 and 6.6.

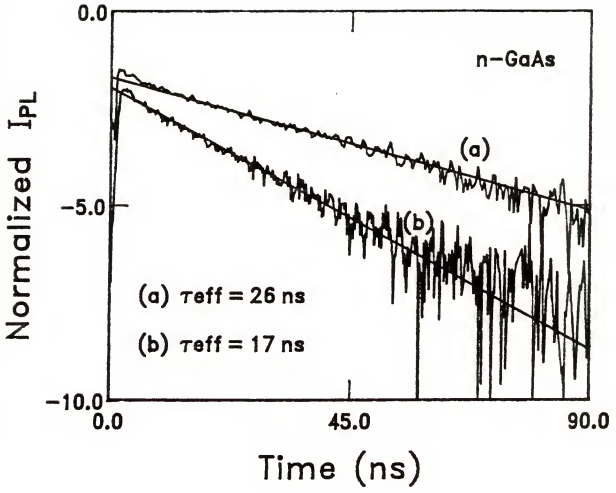

Fig. 6.8. Illustration of the feature of the best fits for the time-domain analysis.

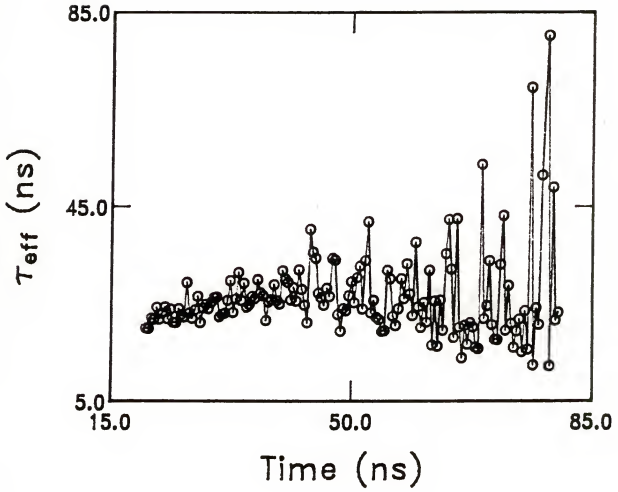

Fig. 6.9. Fluctuation of τ_{eff} at different decay times for d = 0.5 μm. The open circles denote the value for τ_{eff} obtained from the measured signals within the discrete interval of 16 ns. The solid line connects all the data points to show the fluctuations in τ_{eff}. The overall best fit is 26 ns from Fig. 6.8.

CHAPTER 7
CONCLUSIONS

This chapter lists the major results of this thesis. The primary objective was to extract transport parameters in heavily doped semiconductors for modeling of advanced BJTs and solar cells. New data for the minority carrier transport parameters in heavily doped silicon are reported. In addition, new measurement techniques have been developed. As a result, the main objectives have been met. However, there are still many subjects that need to be investigated further, and are listed in Section 7.2 as suggestions for a future work.

7.1 Contributions

The main contributions of the present thesis are

- Photodiode arrays with finely defined metal pattern were fabricated on heavily phosphorous-doped n-type silicon with doping density up to 7.2×10^{19} cm^{-3}.

- Minority hole lifetime was measured in heavily phosphorous-doped n-type silicon. The minority hole lifetime depends quadratically on the doping density, and shows a strong Auger-recombination dependence. Doping ranges from 10^{18} cm^{-3} to 10^{20} cm^{-3} are covered. Empirical fits useful for device modeling were given.

- Minority hole diffusivity and mobility were measured for heavily phosphorous-doped n-type silicon in the doping range of 10^{18} cm^{-3} to 10^{20} cm^{-3}. The mobility data for the minority holes are greater than that for majority holes by a factor of about 2, and shows an increase with donor density N_{DD} in the doping range of $N_{DD} > 4 \times 10^{19}$ cm^{-3}. This behavior is not predicted by the present transport theory, and is believed to be important for understanding the carrier transport physics.

- Temperature dependence of the minority hole mobility and diffusivity in the temperature range of 30 K to 300 K was measured. The preliminary results show a distinctly different transport behavior for the minority carriers from that of the majority carriers. Empirical fits useful for device modeling were given.

- Minority hole diffusion length was measured for heavily phosphorous-doped n-type silicon in the doping range of 10^{18} cm^{-3} to 10^{20} cm^{-3}. The results are consistent with an Auger-limited minority-carrier lifetime and a diffusivity that is doping insensitive in the 10^{18} - 10^{20} cm^{-3} range. The results were used to perform the self-consistent checking for the lifetime and the diffusivity obtained from independent measurements.

- New nondestructive measurement technique for extracting the bulk lifetime τ and the surface recombination velocity S in semiconductor wafers has been developed. The technique allows the separate

determination of S and τ from the same signal, and has been demonstrated on GaAs, Si, and InP wafers.

- New nondestructive measurement technique for extracting the bulk lifetime τ and the surface/interface recombination velocity S in semiconductor thin-film has been developed. The technique allows the characterization of S and τ for samples grown by modern growth techniques, and is useful for studying the radiative lifetime and the Auger lifetime for III-V and other compound semiconductors.

- New nondestructive measurement technique for extracting the bulk lifetime τ and the surface recombination velocity S from semiconductor wafers has been developed. The technique analyzes the luminescence signals in the time domain to extract S and τ from signals at different emission wavelength, and has been demonstrated on chemically passivated GaAs wafers.

7.2 Suggestions for Future Work

7.2.1 Suggestion for Work on Silicon

- Due to its high accuracy, the extension of the lateral photo-current measurement technique for the characterization of the transport parameters in p-type Si is suggested.

- No temperature-dependent data for the energy-gap narrowing effects in the n-type silicon have been reported. This data is essential for modeling the performance of advanced p/n/p BJT at low temperatures. It is also important for investigating the physics of these effects.

- The data for the energy-gap narrowing ΔE_g have been established for p-type Si at different temperatures. However, in extracting ΔE_g the diffusivity data were not measured from the same device. Therefore, the non-uniformity of the doping density, which exists in the heavily doped Si, could result in some uncertainty in the reported data. Therefore, measurements that allows the extraction of diffusivity and ΔE_g from same device, need to be done to establish a more complete data base for heavily doped Si.

- The doping dependence of the surface recombination velocity in heavily doped Si is important for advanced BJT. In literatures, the reported data for both the n- and p-type Si are measured using transistors with vertically gated base. No data for doping density greater than 10^{19} cm^{-3} have been reported for both n- and p-type Si. The application of the non-destructive measurement technique developed in this work to the characterization of the surface properties of heavily doped Si is straightforward, and needs to be done for both conductivity types of Si.

- The measured temperature-dependent mobility data for the minority carriers suggests that the mobility is not controlled by the ionized-impurity scattering but, rather, by the lattice scattering. A carrier transport theory that models this behavior is still not available, and needs to be developed.

7.2.2 Suggestion for Work on GaAs

7.2.2.1 Minority Carriers Mobility

- For p-type GaAs, no results for dopings greater than 2×10^{19} cm^{-3} have been reported yet. For high performance HBT (N/p/N), the acceptor concentration N_{AA} in the base is typically about 1×10^{20} cm^{-3}. Therefore, there is a pressing need for more measurement data within the doping range $2 \times 10^{19} < N_{AA} < 1 \times 10^{20}$ cm^{-3}.
- For n-type GaAs, no data for the minority hole mobility have been reported yet. The minority hole mobility data are essential for design and modeling of the P/n/p (or P/n/P) HBTs, a symmetrical device component to build a fast low power complimentary bipolar logic.
- No temperature dependence for the minority-carrier mobility for both n- and p-type GaAs has been reported. As has been found in silicon, the temperature-dependent mobility data for the minority carriers behave drastically different from that of the majority carriers. It is likely that this difference can be accentuated at low

temperature, and hence the temperature dependence of the minority carrier mobility in both n- and p-type GaAs needs to be characterized. Temperature-dependent characterization of the minority electron and hole mobilities is also essential for the understanding of the minority carriers transport mechanisms.

7.2.2.2 Lifetime

- No directly measured data for lifetime in n-type GaAs are available. The only available data are deduced by using the majority hole mobility and the diffusion length data (from Hwang [58]). More work on the hole lifetime measurement for low- and moderately-doped samples grown by modern growth techniques is essential for the understanding of the radiative lifetime. Similar work for heavily doped samples is essential for understanding the Auger recombination.
- The minority electron lifetime for p-type GaAs with doping density N_{AA} up to 10^{19} cm^{-3} has been established. However, the lifetime for N_{AA} in the higher doping range ($10^{19} < N_{AA} < 10^{20}$ cm^{-3}) hasn't been reported yet. This could be due to the fact that the lifetime is in the sub-nanosecond range, and is difficult to measure. An accurate determination of the lifetime in this very heavily doped range is thus necessary for the understanding of the physics of the recombination mechanisms.
- To investigate the recombination mechanisms in depth, the temperature-dependent measurements of the carrier lifetime in the n-type as well as in the p-type GaAs need to be performed.

7.2.2.3 Surface Recombination Velocity

- Because of the strong effective energy-gap shrinkage in the p^+ GaAs confining layer of a p/p^+ reflection barrier, heterojunction barriers are essential for confining minority electrons in the base region of n-on-p as well as p-on-n GaAs solar cells. The measurement results for the dependence of S on the doping density in the high-low heterojunction have not been well established. The theoretical model for S in the isotype heterojunction that includes the recombinations in both the accumulation and the space charge regions as well as the heavy doping effects in the confining layer needs to be developed for modeling advanced solar cells.
- The effects due to the aluminum mole fraction x on the surface recombination velocity for $Al_xGa_{1-x}As/GaAs$ isotype heterostructure interface needs to be investigated. Physical model accounting for these effects needs to be developed.

7.2.2.4 Energy Gap Narrowing

The effects of energy-gap narrowing ΔE_g on a solar cell are

- The effective energy-gap shrinkage enhances the carrier injection from the base injection into the emitter layer by about a factor of 7, so that the cell's dark current includes a sizeable, sometimes dominant, contribution from the recombination in the emitter layer.
- It could reduce the barrier height of the homojunction barriers, and

hence increase the value of S for the back surface barrier. Moreover, it makes the barrier ineffective for high efficiency applications.

The effects of ΔE_g on an HBT are

- It effectively shrinks the energy-gap in the base, and hence enhances the emitter injection efficiency. This is in contrast to the ΔE_g effect on the silicon BJT, where the common emitter current gain is reduced.

- Only data for p-type GaAs have been reported. This is because most GaAs-based bipolar devices are designed to exploit the high mobility of electrons, and hence work has focused on p-GaAs. The data for ΔE_g for p-GaAs in the doping range of 10^{16} to 10^{20} cm^{-3} have been established. No data for n-type GaAs are available. To estimate the common-emitter current gain for P/n/p (or P/n/P) HBTs, data for ΔE_g in the n-type GaAs need to be characterized.
- No data for the temperature dependence of the energy-gap narrowing in n- and p-type GaAs have been reported. To clarify the physics that governs the energy-gap narrowing, temperature-dependent measurements need to be done.

7.2.2.5 Photorecycling Effects

- These effects lead to difficulties in extracting parameters from high quality thick GaAs layers. They become significant when the layer thickness is greater than the photon escaping distance. More theoretical work modeling this effect is needed.

APPENDIX
DESIGN AND FABRICATION OF THE TRANSMISSION LINE

Because of the parasitic effects, the conventional device-packaging (e.g. TO-5 header) limits the device responses to a frequency f below about 100 MHz. For response with f > 100 Hz, the measured signals are distorted and attenuated because of the impedance mismatch between the header and the 50Ω input impedance of the digitizer. Microwave circuits are designed to avoid these effects such that the responses can be transmitted without any significant distortions. The microwave circuit used in this work are built in a hybrid form. The advantage for the hybrid design is that the active device can be made of an entirely different material than the substrate of the circuit. Microstrip transmission line structures, among all kinds of microwave circuits, are used because of the simplicity of the structure, the low cost of fabrication, and the small dispersion in the signal response.

The geometry of the microstrip is shown in Figure A.1. The parameters that determine the characteristic impedance Z_o of the microstrip line are the strip width W, the height h, the thickness t, and the relative permitivity of the substrate ε_r. The formulas for W/h < 1 that equate all those parameters are given as follows [59].

$$Z_o = 60 \ln[(8h/W_e) + (W_e/4h)]/\sqrt{\varepsilon_r'} \ , \qquad (A.1)$$

where the effective relative permitivity ε_r' is

$$\varepsilon_r' = 0.5\ (\varepsilon_r + 1) + 0.5\ (\varepsilon_r - 1)\ [(1 + 12h/W_e)^{-1/2} + 0.04\ (1 - W_e/h)^2], \qquad (A.2)$$

and the effective strip width W_e is

$$W_e = W + (t/\pi)\ [1 + \ln(4\pi W/t)]. \qquad (A.3)$$

A computer program was developed to solve Eqs. (A.1)-(A.3) numerically for the value of W corresponding to $Z_o = 50\ \Omega$. The calculated result for the strip width is $W \simeq 615\ \mu m$. In the procedure for calculating W, the values of $t = 12.3\ \mu m$, $h = 660\ \mu m$, and $\varepsilon_r = 9.8$ (for alumina) were used.

A mask with $W = 615\ \mu m$ was designed for fabricating the microstrip line. The fabrication procedure of the strip line follows the conventional photolithography process. A photoresist pattern with $W = 615\ \mu m$ on the metal plate was defined by the mask after the photolithography process. The strip line was formed on a ceramic plate coated with Cr/Au thin metal layers after the chemical etching of the uncovered metal. The Au-etching was performed using the etching solution composed of KI (4g), I_2 (1g), and H_2O (40 ml) for ~ 3 min. After the DI-water rinse, the Cr-etching was subsequently performed using the commercial Cr-etchant. The etching time is about 1 min. Finally, the sample was dipped in 2% H_2SO_4 and then rinsed in deionized water. All the chemical etchings were done at room temperature.

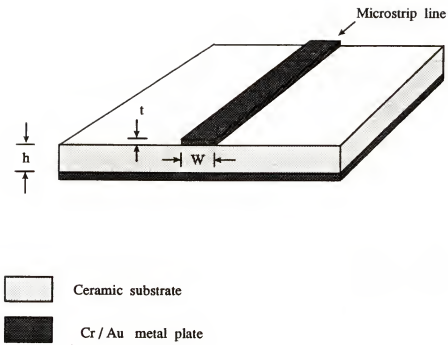

Fig. A.1 Schematic illustration of the microstrip line.

REFERENCES

[1] J. Del Alamo, S. E. Swirhun, and R. M. Swanson, "Measurement and modeling of minority carrier transport in heavily-doped silicon," Solid-State Electron., vol. 28, pp. 47-52, 1985.

[2] R. P. Mertens, J. L. Van Meerbergen, J. F. Nijs, and R. J. Van Overstraeten, "Measurement of the minority-carrier transport parameters in heavily-doped silicon," IEEE Tran. Electron Devices, vol. ED-27, pp. 949-955, May 1980.

[3] J. Dziewior and D. Silber, "Minority-carrier diffusion coefficients in highly-doped silicon," Appl. Phys. Lett., vol.35, pp. 170-172, July 1979.

[4] S. E. Swirhun, J. Del Alamo, and R. M. Swanson, "Measurement of hole mobility in heavily doped n-type silicon," IEEE Electron Device Lett., vol. EDL-7, pp. 168-171, March 1986.

[5] K. Misiakos, C. H. Wang, and A. Neugroschel, "Method for simultaneous measurement of diffusivity, lifetime, and diffusion length, with application to heavily doped silicon," IEEE Electron Device Lett., vol. EDL-10, pp. 111-113, Mar. 1989.

[6] C. H. Wang, K. Misiakos, and A. Neugroschel, "Minority-carrier transport parameters in n-type silicon," IEEE Tran. Electron Devices, vol. ED-37, pp. 1314-1322, May, 1990.

[7] C. H. Wang, K. Misiakos, and A. Neugroschel, "Minority hole diffusion length in heavily doped silicon," Appl. Phys. Lett., vol. 54, pp. 2233-2234, May 1989.

[8] K. Misiakos and F. A. Lindholm, "Generalized reciprocity theorem for semiconductor devices," J. Appl. Phys., vol. 58, pp. 4743-4744, Dec. 1985.

[9] B. Noble, Method Based on the Weiner-Hopf Technique. New York: Pergamon, 1958.

[10] K. Misiakos, C. H. Wang, A. Neugroschel, and F. A. Lindholm, "Simultaneous extraction of minority-carrier transport parameters in crystalline semiconductors by lateral photocurrent," J. Appl. Phys., vol. 67, pp. 321-333, Jan. 1990.

[11] C. H. Wang, "Measurement of minority carrier transport in heavily doped silicon," Master's thesis, University of Florida, May, 1989.

[12] J. Dziewior and W. Schmid, "Auger coefficients for highly-doped and highly-excited silicon," Appl. Phys. Lett., vol. 31, pp. 346-348, Sep. 1977.

[13] A. Haug, "Recombination mechanism in heavily doped silicon," Solid-State Electron., vol. 25, pp. 665-667, 1982.

[14] W. Lochmann and A. Haug, "Phonon-assisted Auger recombination in Si with direct calculation of the overlap integrals," Solid State Commun., vol. 35, pp. 553-556, 1980.

[15] P. T. Landsberg, "Trap-Auger recombination in silicon of low carrier densities," Appl. Phys. Lett., vol. 50, pp. 745-747, March, 1987.

[16] J. A. del Alamo, "Minority carrier transport in heavily doped n-type silicon," Ph.D. Dissertation, Stanford University, Nov., 1985.

[17] M. S. Tyagi and R. Van Overstraeten, "Minority carrier recombination in heavily-doped silicon," Solid-State Electron., vol. 26, pp. 577-597, 1983.

[18] W. R. Thurber, R. L. Mattis, Y. M. Liu, and J. J. Filliben, "Resistivity-dopant density relationship for boron-doped silicon," J. Electrochem. Soc., vol. 127, pp. 2291-2295, Oct. 1980.

[19] C. H. Wang, K. Misiakos, and A. Neugroschel, "Temperature dependence of minority hole mobility in heavily doped silicon," Appl. Phys. Lett., vol. 57, pp. 159-161, July, 1990.

[20] H. S. Bennett, "Hole and electron mobilities in heavily doped silicon: comparison of theory and experiment," Solid-State Electron., vol. 26, pp. 1157-1166, 1983.

[21] J. R. Lowney and H. Bennett, "Majority and minority electron and hole mobilities in heavily doped GaAs," to be published in J. Appl. Phys.

[22] T. H. Ning and C. T. Sah, "Theory of scattering of electrons in a nondegenerate-semiconductor-surface inversion layer by surface-oxide charges," Phys. Review B, vol. 6, pp. 4605-4608, 1972.

[23] J. D. Cressler, D. D. Tang, K. A. Jenkins. G. P. Li, and E. S. Yang, "On the low temperature static and dynamic properties of high-performance silicon bipolar transistors," IEEE Trans. Electron Devices, 36, 1489 (1989).

[24] S. E. Swirhun, D. E. Kane and R. M. Swanson, "Temperature dependence of minority electron mobility and bandgap narrowing in p^+ Si," IEDM Dig., pp. 298-301, 1988.

[25] J. Bardeen and W. Shockley, Phys. Rev., 80, 72 (1950).

[26] N. D. Arora, J. R. Hauser and D. J. Roulston, "Electron and hole mobilities in silicon as a function of concentration and temperature," IEEE Trans. Electron Devices, vol. ED-29, pp. 292-295, 1982.

[27] P. W. Chapman, O. N. Tufte, J. D. Zook, and D. Long, "Electrical properties of heavily doped silicon," J. of Appl. Phys., vol. 34, pp. 3291-3295, 1963.

[28] J. R. Lowney, "Impurity bands and band tailing in moderately doped silicon," J. Appl. Phys., 59, 2048 (1986).

[29] J. D. Beck and R. Conradt, Solid-St. Commun., vol. 13, pp. 93-95, 1973.

[30] S. E. Swirhun, Y, -H. Kwark, and R. M. Swanson, "Measurement of electron lifetime and band-gap narrowing in heavily doped p-type silicon," in IEDM Tech. Dig., 1986, pp.24-27.

[31] M. S. Tyagi, J. F. Nijs, and R. J. Van Overstraeten, "Effect of surface recombination on the transient decay of excess carriers produced by short wavelength pulses," Solid-State Electron., vol. 25, pp.411-415, 1982.

[32] D. E. Ioannou and R. J. Gledhill, "Effect of surface recombination on the decay of excess minority carriers in semiconductors induced by finely focused picosecond pulsed laser beams," J. Appl. Phys., vol. 56, pp. 1797-1800, 1984.

[33] K. Misiakos, F. A. Lindholm, and A. Neugroschel, "Solution of the continuity equation in planar symmetry cases and assessment of photoluminescence decay," J. Appl. Phys., vol. 58, pp. 1647-1650, 1985.

[34] G. W. 't Hooft and van Opdorp, "Determination of bulk minority-carrier lifetime and surface/interface recombination velocity from photoluminescence decay of a semi-infinite semiconductor slab," J. Appl. Phys., vol. 60, pp. 1065-1070, 1986.

[35] R. J. Nelson and R. G. Sobers, "Interfacial recombination velocity in GaAlAs/GaAs heterostructures," Appl. Phys. Lett., vol. 32, pp. 761-763, 1978.

[36] R. J. Nelson, J. S. Williams, H. J. Leamy, B. Miller, H. C. Casey, Jr., B. A. Parkinson, and A. Heller, "Reduction of GaAs surface recombination velocity by chemical treatment," Appl. Phys. Lett., vol. 36, pp. 76-79, 1980.

[37] R. J. Nelson and R. G. Sobers, "Minority-carrier lifetime and internal quantum efficiency of surface-free GaAs," J. Appl. Phys., vol. 49, pp. 6103-6108, 1978.

[38] Yablonovitch, C. J. Sandroff, R. Bhat, and T. Gmitter, "Nearly ideal electronic properties of sulfide coated GaAs surfaces," Appl. Phys. Lett., vol. 51, pp. 439-441, 1987.

[39] R. K. Ahrenkiel, D. J. Dunlavy, R. Y. Loo, and G. S. Kamath, "Minority-carrier lifetime in n-$Al_{0.38}Ga_{0.62}As$," J. Appl. Phys., vol. 63, pp. 5174-5176, 1988.

[40] R. K. Ahrenkiel, M. M. Al-Jassim, D. J. Dunlavy, K. M. Jones, S. M. Vernon, S. P. Tobin, and V. E. Haven, "Minority carrier lifetime of GaAs on silicon," Twentieth IEEE Photovoltaic Specialist Conference , 1988, pp. 684-687.

[41] R. K. Ahrenkiel, D. J. Dunlavy, and M. L. Timmons, "III-V compound process development using photoluminescence lifetime," Twentieth IEEE Photovoltaic Specialist Conference, 1988, pp. 611-615.

[42] J. M. Borrego, R. J. Gutmann, and N. Jensen, "Non-destructive lifetime measurement in silicon wafers by microvave reflection," Solid-State Electron., vol. 30, pp. 195-203, 1987.

[43] K. Nauka, H. C. Gatos, and J. Lagowski, "Oxygen-induced recombination centers in as-grown Czochralski silicon crystals, "Appl. Phys. Lett., vol. 43, pp. 241-243, 1983.

[44] G. L. Miller, D. A. Robinson, and S. D. Ferris, "Non-destructive electrical test methods for semiconductor materials," Proc. Electrochem. Soc., vol. 78-3, pp. 1-31, 1978.

[45] W. van Roosbroeck and W. Shockley, "Photon-radiative recombination of electrons and holes in germanium," Physical Review, vol. 94, pp. 1558-1560, 1954.

[46] K. Misiakos and A. Neugroschel, "Lifetime and diffusivity determination from frequency-domain transient analysis," IEEE Electron Device Lett., vol. EDL-8, pp. 358-360, 1987.

[47] H. C. Casey, D. D. Sell, and K. W. Wecht, "Concentration dependence of the absorption coefficient for n- and p-type GaAs between 1.3 and 1.6 eV," J. Appl. Phys., vol. 46, pp. 250-257, 1975.

[48] R. S. Besser, and C. R. Helms, "Comparison of surface properties of sodium sulfide and ammonium sulfide passivation of GaAs," J. Appl. Phys., vol. 65, pp. 4306-4310, 1989.

[49] S. E. Swirhun, "Characterization of majority and minority carrier transport in heavily doped silicon," Ph.D. Dissertation, Stanford University, 1987.

[50] R. K. Ahrenkiel, D. J. Dunlavy, and T. Hanak, "Minority-carrier lifetime in ITO/InP heterojunctions," J. Appl. Phys., vol. 64, pp. 1916-1921, 1988.

[51] G. Lubberts, and B. C. Burkey, "Optical and electrical properties of heavily phosphorus-doped epitaxial silicon layers," J. Appl. Phys., vol. 55, pp. 760-763, 1984.

[52] S. M. Sze, Physics of Semiconductor Devices, 2nd Edition. New York: Wiley, 1981.

[53] R. S. Besser and C. R. Helms, "Effect of sodium sulfide treatment on band bending in GaAs," Appl. Phys. Lett., vol. 52, pp. 1707-1709, 1988.

[54] C. H. Wang and A. Neugroschel, "Minority-carrier lifetime and surface recombination velocity measurement by frequency domain photoluminescence," accepted for publishing in IEEE Trans. Electron Devices, see also Chapter 4 of this thesis.

[55] G. W. 'tHooft, C. van Opdorp, H. Veenvliet, and A. T. Vink, "Minority carrier lifetime and luminescence in MOVPE-grown (Al,Ga)As epilayers and DH lasers," J. of Crystal Growth, vol. 55, pp. 173-182, 1981.

[56] J. M. Borrego and S. K. Ghandhi, "Interface recombination velocity and lifetime in GaAs and AlGaAs/GaAs structure," Solid-State Electronics, vol. 33, pp. 733-736, 1990.

[57] J. M. Olson, R. K. Ahrenkiel, D. J. Dunlavy, B. M. Keyes, and A. E. Kibbler, "Ultralow recombination velocity at $Ga_{0.5}In_{0.5}P$/GaAs heterointerfaces," Appl. Phys. Lett., vol. 55, pp.1208-1210, 1989.

[58] C. J. Hwang, "Doping dependence of hole lifetime in n-type GaAs," J. of Appl. Phys., vol. 42, pp. 4408-4409, 1971.

[59] Tri T. Ha, Solid State Microwave Amplifier Design, Wiley, New York, 1981.

BIOGRAPHICAL SKETCH

Chih Hsin Wang was born in Taipei, Taiwan, R.O.C., in 1959. He received the BS degree in physics from the National Tsing Hua University in 1983 and the M.S. and Ph.D. degrees in electrical engineering from the University of Florida in 1989 and 1991, respectively. His Master's thesis was given the best master's thesis award in the department.

From 1985 to 1986, he was a research assistant in the Department of Electrical Engineering of the National Tsing Hua University, worked on the characterization of polysilicon MOSC diode. His research interests include semiconductor device physics and technology.

I certify that I have read this study and that in my opinion it conforms to acceptable standards of scholarly presentation and is fully adequate, in scope and quality, as a dissertation for the degree of Doctor of Philosophy.

Arnost Neugroschel

Arnost Neugroschel, Chair
Professor of Electrical
Engineering

I certify that I have read this study and that in my opinion it conforms to acceptable standards of scholarly presentation and is fully adequate, in scope and quality, as a dissertation for the degree of Doctor of Philosophy.

Fred Lindholm

Fredrik A. Lindholm, Cochair
Professor of Electrical
Engineering

I certify that I have read this study and that in my opinion it conforms to acceptable standards of scholarly presentation and is fully adequate, in scope and quality, as a dissertation for the degree of Doctor of Philosophy.

Sheng Sam Li

Sheng S. Li
Professor of Electrical
Engineering

I certify that I have read this study and that in my opinion it conforms to acceptable standards of scholarly presentation and is fully adequate, in scope and quality, as a dissertation for the degree of Doctor of Philosophy.

Gijs Bosman

Gijs Bosman
Professor of Electrical
Engineering

I certify that I have read this study and that in my opinion it conforms to acceptable standards of scholarly presentation and is fully adequate, in scope and quality, as a dissertation for the degree of Doctor of Philosophy.

Ulrich H. Kurzweg

Ulrich H. Kurzweg
Professor of Aerospace
Engineering, Mechanics, and
Engineering Sciences

This dissertation was submitted to the Graduate Faculty of the College of Engineering and to the Graduate School and was accepted as partial fulfillment of the requirements for the degree of Doctor of Philosophy.

May 1991

for Herbert A. Bruns
Winfred M. Phillips
Dean, College of Engineering

Madelyn M. Lockhart
Dean, Graduate School